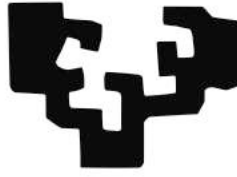eman ta zabal zazu

UPV   EHU

University of the Basque Country

Department of Material Physics

PhD Thesis

Polythiophene-based nanoscale lateral devices

Thales V. A. G. de OLIVEIRA

from São Paulo

May 2014

Sypervised by Dr. Alexander M. Bittner
& Dr. Luis E. Hueso

Abstract

The integration of functional organic materials in electronic devices holds great promise for current and future applications. Organic materials offer many advantages over their inorganic counterparts, such as high chemical tunability, low-temperature processing, and the prospect for low-cost, large-area manufacturing. In this thesis, solution-processable polythiophene-based materials are investigated towards integration in spintronic, and low-voltage field-effect transistor (FET) devices.

In the first part of this thesis, the electrical transport of the highly conductive poly-(3,4-ethylene-dioxythiophene):poly(styrenesulfonic acid) (PEDOT:PSS) is studied with ohmic and spin-polarized tunnel electrodes of nanoscale lateral dimensions. Temperature-dependent charge transport measurements revealed that electrical conductivity scales non-linearly as a function of electrode spacing, which is attributed to the localization of carriers induced by the disorder, induced by the PSS polyelectrolyte. In addition, the integration of this conducting polymer in nanoscale lateral spin valve devices is demonstrated by controlling the pH of the PEDOT:PSS solution, and by protecting the ferromagnetic contacts with a metal oxide barrier (AlO_x). Charge and magneto-transport measurement results of $NiFe/AlO_x/PEDOT:PSS/AlO_x/NiFe$ lateral structures are presented for various thicknesses of the alumina tunnel barriers. The absence of magnetoresistance in these spin valves is interpreted within the framework of Valet-Fert theory, and the results prove valuable for the estimation of an upper limit of the carriers' spin lifetime in PEDOT:PSS.

In the second part, ultrathin hybrid gate dielectrics based on aluminum oxide (AlOx) and mixed-type phosphonic-acid self-assembled monolayers (SAM) were studied with a high performance liquid-crystalline semiconducting polymer, viz. poly(2,5-bis(3-alkylthiophen-2-yl)thieno[3,2-b]thiophene (pBTTT). By co-assembling of carboxylate- and methyl-terminated SAMs one can obtain high surface energy, while recovering the leakage current levels obtained with pure methyl-terminated monolayers. Atomic force microscopy analysis shows that the surface chemistry of the underlying mixed SAM has a strong impact on the morphology of pBTTT films, and consequently their electrical response. A strong improvement of the field-effect transistor characteristics is observed at low concentration of carboxylate groups, accompanied by the appearance of the well-known terrace-like microstructure of pBTTT for the monolayers with lower surface energies. Although terraced morphology is known for this polymer, it never been observed on patterned metal electrodes, which make up the basic structure of integrated circuits.

In the last part of this thesis, the mixed SAM approach is further exploited to manufacture field-effect transistors based on pBTTT with nanoscale lateral dimensions, and patterned metal gate electrodes. Owing to the high capacitance of this ultrathin AlO_x/SAM hybrid dielectric, pBTTT nanotransistors operate at very low input voltages ($<3V$), low leakage currents ($<5pA$) and relatively high on/off ratios ($\sim10^3$). Furthermore, optimization of the atomic force microscopy imaging process of pBTTT films directly reveals the morphology and size distribution of nanoscale crystallites within pBTTT terraces. The observed crystallite diameter is twice as high as previous literature values.

Resumen

La electrónica orgánica o la electrónica plástica, es una rama de la ciencia de los materiales dedicada a la comprensión de los procesos electrónicos en la materia orgánica, como la transferencia de carga (de corto alcance) o el transporte de carga (de largo alcance). Los dispositivos electrónicos orgánicos se fabrican con semiconductores basados en carbono, tales como pequeñas moléculas y polímeros de sistema conjugado. Ésto contrasta con la electrónica tradicional, que se basa en semiconductores o conductores inorgánicos, tales como el Silicio o el Cobre. Los semiconductores orgánicos (OSC) ofrecen muchas ventajas sobre los materiales electrónicos tradicionales . Su procesamiento por lo general requiere métodos de fabricación de bajo coste, como recubrimiento por inmersión, impresión por chorro de tinta, estampado, sublimación a la temperatura ambiente, auto-ensamblaje, etc. El procesamiento de semiconductores orgánicos se realiza generalmente a bajas temperaturas (<180°C), lo que permite la integración con sustratos flexibles (p.e. hojas de plástico), y como consecuencia la ampliación de la gama de aplicaciones que requieren dispositivos electrónicos. Por otra parte, los OSC se pueden modificar químicamente y sus propiedades se pueden fácilmente ajustar para cumplir con los requisitos de la aplicación. Los avances en la electrónica orgánica han sido notables en las últimas décadas, tanto desde el punto de vista fundamental como técnico. Actualmente, los diodos orgánicos emisores de luz (OLED) son la principal tendencia tecnológica en el mercado de las pantallas. De hecho, incluso la curvatura de los aparatos de televisión flexibles basados en OLED ya pueden ser controlados. Otra potente tecnología basado en OSCs son los dispositivos fotovoltaicos orgánicos (OPV). Sin embargo, aunque las células solares orgánicas con un récord de eficiencia del 12 % se han logrado a escala experimental en el laboratorio, el mantenimiento de la alta eficiencia en la producción en cadena (por ejemplo, procesamiento rollo-a-rollo) ha demostrado ser muy complicado. Otra tecnología interesante son los transistores de efecto de campo orgánico (OFET), que hasta ahora han tenido menos éxito comercial, pero siguen siendo un tema de gran actividad de investigación académica y de desarrollo industrial a pequeña escala.

Las aplicaciones mencionadas hasta ahora se basan exclusivamente en electrones de transporte de carga en materiales funcionales, sean orgánicos o inorgánicos. Los electrones, sin embargo, son partículas subatómicas elementales que poseen tanto carga como un momento angular intrínseco de espín $\frac{1}{2}\hbar$. En consecuencia, la información almacenada en el espín se ignora en gran medida en la mayoría de las aplicaciones electrónicas. Con el objetivo de explotar las propiedades del espín en la electrónica de

estado sólido, ha surgido un área de investigación relativamente nuevo - electrónica basada en el espín, o espintrónica. Tal vez la primera observación de que el espín de un electrón puede afectar transporte de carga fue en el año de 1856, cuando William Thomson (también conocido como Lord Kelvin) demostró que dependiendo de la orientación y la fuerza de un campo magnético externo aplicado a un metal ferromagnético, se puede alterar la resistividad eléctrica. Este fenómeno se conoce como la magnetorresistencia anisótropa (AMR), y se introdujo en aplicaciones comerciales por primera vez en 1991 por IBM. Los dispositivos de espintrónica más prometedores de hoy en dia son las memorias de acceso aleatorio magnetorresistivas (MRAM) basadas en los fenómenos de transferencia de momento magnético del espín (STT), que están siendo desarrollados por la industria de almacenamiento de información. Este dispositivo, llamado STT-MRAM, se basa directamente en conmutación del estado de resistencia de una célula de memoria por la transferencia del momento de espín, sin la necesidad de un campo magnético externo. Esto es muy ventajoso ya que permite la completa operación eléctrica (respuesta rápida), operación lógica en conjunción con una función de memoria, y puede ser fácilmente miniaturizado debido al circuito integrado simplificado (IC).

La comercialización de dispositivos que muestran magnetorresistencia (MR) ha sido muy estimulado por el descubrimiento del efecto de magnetorresistencia gigante (GMR) a principios de 1988 por Baibish *et al.* El efecto GMR se observó en estructuras de películas delgadas de múltiples capas compuestas de metales ferromagnéticos (FM) separadas por capas metálicas no magnéticas (NM). Debido a la separación impartida por las capas de metal NM, la magnetización de las capas de FM puede revertir de forma independiente. Se ha observado un fuerte efecto de MR al cambiar la orientación relativa
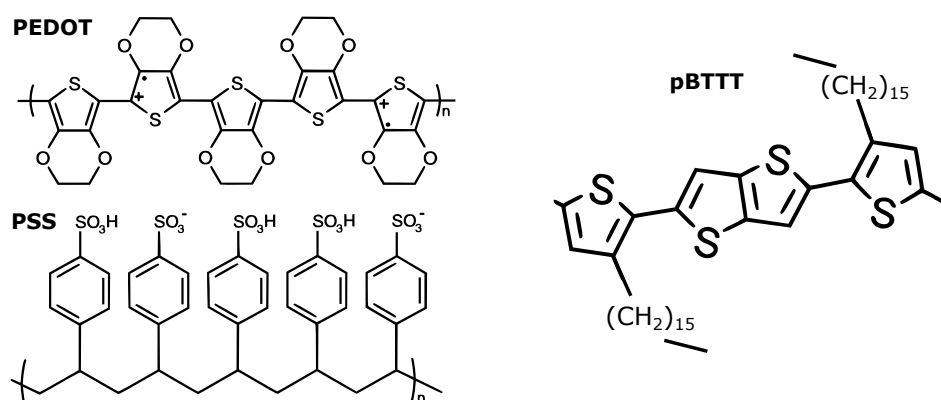
Semiconductores orgánicos estudiados en esta tesis. En la *izquierda*, la estructura química del polímero conductor poli-(3,4-etileno-dioxitiofeno):poli(ácido estirenosulfónico) (PEDOT:PSS). En la *derecha*, la estructura química del polímero semiconductor poli[2,5-bis(3-alquiltiofeno-2-il)tieno[3,2-b]tiofeno (pBTTT).

de los momentos magnéticos de las película FM, que fué un orden de magnitud superior a efectos de MR vistos en dispositivos basados en AMR. El mecanismo fundamental detrás de las grandes señales de MR obtenidas fue la conservación de la orientación del espín al cruzar la interfaz FM/NM. Un efecto MR gigante surgió cuando la capa de material NM tenía un espesor comparable a la longitud de difusión del espín (L_{sf}) en este metal. Desde este descubrimiento, la investigación de los fenómenos relacionados con el espín de los electrones se ha convertido en un área de investigación muy activa debido a su potencial hacia la física fundamental y las aplicaciones, y ha sido testigo de numerosas ramificaciones a lo largo de la última década.

Entre ellos, la búsqueda de espaciadores NM que ofrecen más funcionalidades es notable. Por ejemplo, considerables esfuerzos se han puesto en el uso de los semiconductores inorgánicos (por ejemplo Si, GaAs), debido a la posibilidad de su integración en tecnologías existentes, y la posibilidad de realizar lógicas de computación cuántica. Motivado por la demanda de las nuevas tecnologías, ha surgido otra área de investigación interesante que tiene como objetivo la integración de los materiales orgánicos con los dispositivos de espintrónica. Más allá de las características fascinantes que ofrecen los OSC, como la flexibilidad y el bajo coste de fabricación, la característica que realmente atrajo a la comunidad espintrónica fue el bajo peso atómico (Z) de los elementos que componen la mayor parte de los OSC (por ejemplo, C, H, N, O). La interacción hiperfina (HI) y la interacción del espín-órbita (SOI) se ha sabido durante mucho tiempo que son las principales causas de dispersión del espín de los electrones. Como la interacción espín-órbita es proporcional a Z^4, se espera que el tiempo de vida de espín en OSCs debe ser mucho más larga que sus homólogos inorgánicos (por ejemplo de Si, Cu). La interacción hiperfina, que resulta de la interacción del espín del electrón con momentos magnéticos nucleares, todavía existe en los OSC debido a la presencia de átomos de H (espín nuclear 1/2). Sin embargo, esta interacción es considerada muy débil en comparación con la componente del SOI. Otros aspectos importantes de los OSCs son sus bajas movilidades (10^{-5}-10^1 cm^2/Vs) y las bajas densidades de portadores de carga. El transporte de carga en estos materiales se caracteriza por saltos incoherentes entre estados localizados. Estos estados electrónicos son tan estrechos que la conducción no puede ser tratada por las teorías de la banda clásicas. El transporte de carga a través de un ancho de banda estrecho (típicamente 0.1eV) alrededor de los orbitales moleculares localizados es seguido generalmente por una distorsión en la estructura molecular locales (polarones). Curiosamente, a pesar de las bajas movilidades en los OSC, se obtienen relativamente largas longitudes de difusión de giro debido a los largos tiempos de relajación del espín, que pueden alcanzar valores superiores a 10μs. Por ejemplo, para pequeñas moléculas semiconductoras como cristales de rubreno con estructura optimi-

zada, existen estimaciones teóricas de que la longitud de difusión del espín podría ser incluso más grande que un milímetro.

En esta tesis, nanoestructuras híbridas orgánico-inorgánico a nanoescala son investigads como componentes de dispositivos electrónicos funcionales. Se han estudiado dos temas en este trabajo. En la primera parte, válvulas de espín orgánicas, un concepto novedoso que permite el almacenamiento de información en los dispositivos electrónicos orgánicos. El trabajo presentado sirve como base para la comprensión de la integración de polímeros conductores con materiales ferromagnéticos, y los fenómenos de transporte de espín en dispositivos laterales a nanoescala. El segundo tema aborda transistores orgánicos de película delgada, que permiten la fabricación de circuitos integrados a través de los métodos de fabricación de bajo coste (por ejemplo, procesamiento de la solución). Se presenta una investigación experimental sobre dieléctricos de puerta basados en capas auto-ensambladas y su interacción con los polímeros semiconductores de alta cristalinidad. Otro aspecto importante estudiado en esta tesis, es la miniaturización de dispositivos. La reducción de los dispositivos de dimensiones nanoscópicas no sólo puede mejorar las propiedades conocidas, sino que puede dar lugar a nuevas funcionalidades. Por ejemplo, la reducción de longitudes de canal OFET (L) puede mejorar la frecuencia de funcionamiento máxima (f) de estos dispositivos desde que $f \propto 1/L$. En el caso de los dispositivos de espintrónica orgánicos, la fabricación a escala nanométrica es imprescindible para su funcionamiento, pues las longitudes de difusión del espín en estos materiales son relativamente cortas.

Esta tesis está organizada de la siguiente forma. En la primera parte, se ha estudiado el transporte eléctrico del polímero de alta conductividad poli-(3,4-etileno-dioxitiofeno):poli(ácido estirenosulfónico) (PEDOT:PSS) con electrodos óhmicos y electrodos de túnel de espín
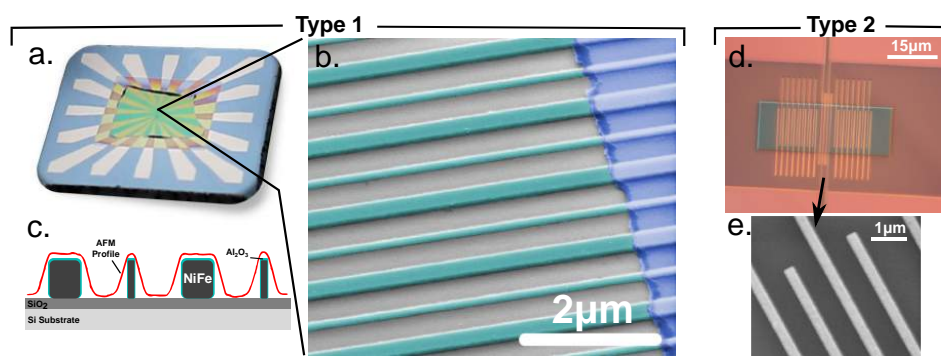

Válvulas de espín laterales (*Tipo 1*) y las sondas de cuatro puntos (*Tipo 2*). Las válvulas de espín interdigitados de dos terminales típicas están basadas en nanoelectrodos con polarización de espín de $NiFe/AlO_x$. Las sondas de cuatro puntos han sido utilizadas para medidas eléctricas a baja escala. Ambos dispositivos se utilizan para estudiar el transporte de carga y de espín en PEDOT:PSS.

polarizados de dimensiones laterales a nanoescala. Las mediciones del transporte de carga en función de la temperatura revelaron que la conductividad eléctrica varia no linealmente en función de la distancia entre electrodos, lo que se atribuye a la localización de portadores de carga inducidos por el desorden causado por el polielectrolito PSS. Además, la integración de este polímero conductor en dispositivos de válvula de espín laterales nanométricos se ha demostrado mediante el control del pH de la solución PEDOT:PSS, y protegiendo los contactos ferromagnéticos con una barrera de un óxido de metal (AlOx). Se presentan los resultados de medidas de transporte y magnetoresistencia de las estructuras laterales de NiFe/AlOx/PEDOT:PSS/AlOx/NiFe para diferentes espesores de las barreras del túnel de alúmina. La ausencia de la magnetorresistencia en estas válvulas de espín se interpreta en el marco de la teoría de Valet-Fert, y los resultados muestran ser válidos para la estimación de un límite máximo de tiempo de vida del espín de los portadores de carga en PEDOT:PSS.
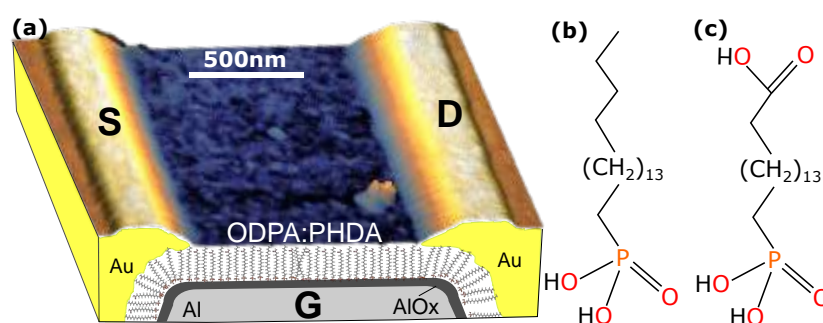
Transistores orgánicos de baja tensión con electrodos de puerta híbridos y estampados. Se investigan dieléctricos de compuerta ultrafinos basados en monocapas auto-ensambladas de tipo mixto (*derecha*) y su interacción con pBTTT.

En la segunda parte, se han estudiado dieléctricos de compuertas híbridas ultrafinas basados en óxido de aluminio (AlOx) y monocapas (SAM) autoensambladas de ácido fosfórico de tipo mixto con un polímero semiconductor líquido cristalino de alto rendimiento, el poli[2,5-bis(3-alquiltiofeno-2-il)tieno[3,2-b]tiofeno (pBTTT). Mediante el co-ensamblaje de los grupos terminales carboxilo y metilo del SAM se puede obtener una alta energía superficial, y recuperar los niveles de fuga de corriente obtenidos con monocapas con terminaciones de metilo puras. El análisis de microscopía de fuerza atómica muestra que la química superficial de la SAM mixta subyacente tiene un fuerte impacto en la morfología de las películas de pBTTT, y en consecuencia en su respuesta eléctrica. Se ha observado una fuerte mejora en las características del transistor de efecto de campo a baja concentración del grupo carboxilo, acompañado por la aparición de la conocida microestructura del pBTTT de tipo terraza para las monocapas con energías superficiales más bajas. Aunque la morfología de terrazas ya es conocida
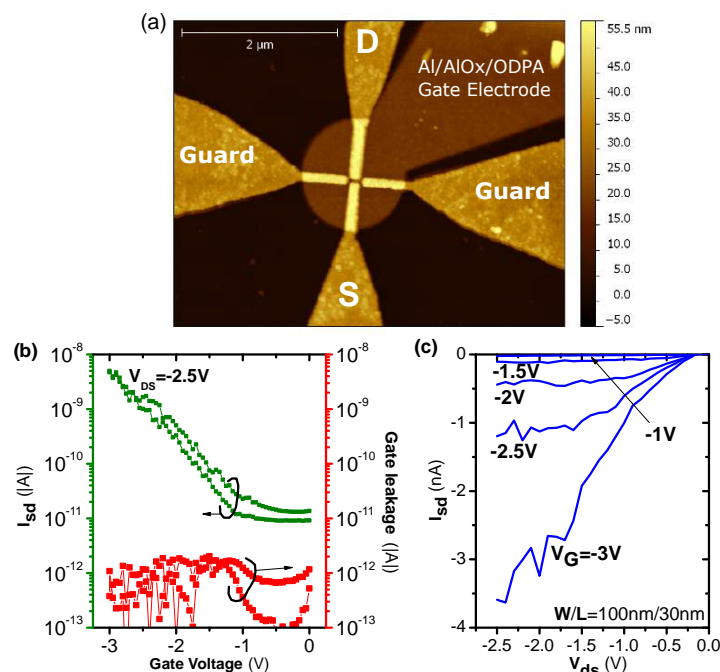
Nanotransistores de pBTTT con electrodos de compuerta híbridos estampados. Los dispositivos con canales de hasta 20nm, en las dimensiones de un cristal de pBTTT, han sido fabricados y estudiados.

para este polímero, nunca se ha observado en los electrodos metálicos estampados, que constituyen la estructura básica de los circuitos integrados.

En la última parte de esta tesis, se estudia aún más la estrategia de los SAM mixtos para la fabricación de transistores de efecto de campo basados en pBTTT con dimensiones laterales nanométricas, y electrodos de puerta de metal estampado. Debido a la alta capacitancia de estos dieléctricos híbridos ultrafinos AlOx/SAM, los nanotransistores de pBTTT operan a tensiones de entrada muy bajos (<3V), a bajas corrientes de fuga (<5pA), y a relativamente altos ratios de ON/OFF (10^3). Por otra parte, la optimización del proceso de las imágenes de microscopía de fuerza atómica de las películas de pBTTT revela directamente la morfología y la distribución del tamaño de los cristales nanométricos dentro de las terrazas de pBTTT . El diámetro de los cristales observados es el doble de los valores encontrados en la bibliografía.

Palabras clave: *espintrónica orgánica, transistores de película delgada, autoensamblaje, electrónica orgánica, válvulas de espín, semiconductores orgánicos, poli[2,5-bis(3-alquiltiofeno-2-il)tieno[3,2-b]tiofeno, pBTTT, poli-(3,4-etileno-dioxitiofeno):poli(ácido estirenosulfónico), PEDOT:PSS*

Contents

Contents

1 Introduction

Nanotechnology is the manipulation of matter on supramolecular, molecular, or even atomic length scales.[1] Since this field of research and technology is simply defined in terms of sizes, it encompasses a broad range of sciences, including biology, materials science, physics, chemistry, etc.[2]; and applications ranging from microelectronics to medicine. In fact, most of the electronic devices in current society (e.g. smartphones, laptops, etc) benefits from nanotechnologies. At the heart of these technologies lies what is maybe the most important invention of the twentieth century – the *transistor*. This is the key component of modern technologies, and is used to switch and/or amplify electronic signals. Current state-of-the-art, high-end microprocessors are being shipped with the so-called "22 nanometer technology node" (e.g. Intel's Haswell Microprocessors), which means that the half-pitch of the lateral features in these devices have only 22nm. Highly scaled devices also means that more transistors can fit in a chip – today's microprocessors are manufactured with a staggering number of transistors (>1.8 billion with current technology).

Reduction of transistor dimensions to improve performance – as dictated by the well-known "Moore's Law" – is nearing its end, and the Semiconductor Industry is facing ever increasing challenges. This is easily understood since for this technology node layers of dielectric materials must be on the order of 0.5-1nm thick (a few atoms), and even advanced thin-film deposition techniques such as atomic layer deposition (ALD) fail in producing devices with no faults. In fact, Intel's release of the next semiconductor technology node (14nm) that was expected for the year 2014[1] may be potentially postponed to the upcoming year due to defects in their microprocessors. The end of Moore's Law signs the emergence of an era where microelectronics technology is not solely dominated by silicon-based materials & devices, and *top-down* fabrication (i.e. photolithograpy, reactive ion etching, etc) is not the unique manufacturing approach at the nanoscale. The industry is now faced with a new trend, the so called "More-than-Moore", where value is added in the devices not by following the size scaling rules of Moore's Law, but by incorporating new materials and functionalities.[3] This paradigm

---

[1]As predicted by the International Technology Roadmap for Semiconductors (ITRS).

shift has been anticipated a couple of decades ago, and several research areas have emerged to meet the demand for new technologies.

1.1 Organic Materials for Electronic and Spintronic Applications

Although silicon-based devices will continue being the major player in solid-state electronics in the foreseeable future, other exciting technologies exist. Among them lies organic electronics (or plastic electronics), a branch of materials science devoted to the understanding of electronic processes in organic matter, such as short range charge transfer or long-range charge transport. Organic electronic devices are manufactured with carbon-based semiconductors, such as π-conjugated small molecules and polymers. This contrasts with traditional electronics, which relies on inorganic semiconductors or conductors such as silicon or copper.

Organic semiconductors (OSC) offers many advantages over traditional electronic materials. Their processing usually requires low-cost fabrication methods, such as spin-coating, ink-jet printing, stamping, sublimation at or near-room temperature, self-assembly, etc. Organic semiconductor processing is usually performed at low temperatures ($<180°$C) allowing integration with flexible substrates (e.g. plastic sheets), widening the range of applications requiring electronic devices. Moreover, OSCs can be chemically tuned and a vast range of properties can be tailored to fulfil application requirements. Progress in organic electronics has been remarkable in the past decades, both from the fundamental and technological standpoint. Organic light emitting diodes (OLED) [4] are currently the main technological trend in the display market. In fact, even the curvature of OLED-based bendable television sets can be controlled. Another potential technology based on OSCs are organic photovoltaics (OPV). However, although organic solar cells with record efficiency of 12% have been achieved in laboratory scale experiments, keeping high efficiency in up-scaled manufacture (e.g. roll-to-roll processing) has proven difficult. Another exciting technology is the organic field-effect transistor (OFET) [5–7], which so far has had less commercial success, but remains a highly active topic of academic research and small-scale industrial developments (e.g. Plastic Logic).

The applications mentioned so far rely exclusively on electron (or hole) charge transport in functional materials, be it organic or inorganic. Electrons, however, are subatomic elementary particles that possess both charge e and an intrinsic angular moment of $\frac{1}{2}\hbar$

(spin). Consequently, the spin information stored in electrons is largely neglected in the majority of electronic applications. Aiming at exploiting the electron spin dregree of freedom in solid state electronics, a relative new research has emerged – spin-based electronics, or *spintronics* for short. Perhaps the first observation that the spin of an electron can affect charge transport dates back to 1856, when William Thomson (also known as Lord Kelvin) demonstrated that depending on the orientation and strength of an external magnetic field applied to a ferromagnetic metal, the electrical resistivity changes. This phenomenon is known as anisotropic magnetoresistance (AMR), and was introduced in commercial applications for the first time in 1991 by IBM [8]. Today's most promising spintronic devices are the magnetoresistive random-access-memories (MRAM) based on spin torque transfer phenomena (STT), which is under development by the information storage industry. This so-called STT-MRAM directly relies on spin-polarized electrons switching the resistance state of a memory cell, without an external magnetic field. This is very advantageous since it allows an all-electrical operation (fast response), all-spin logic operation with built-in memory[9], and can be easily miniaturized due to the simplified integrated circuit (IC).

The commercialization of devices showing magnetoresistance (MR) has been much stimulated by the discovery of the giant magnetoresistive effect (GMR) a few years earlier in 1988 by Baibish *et al.*[10]. The GMR effect was observed in multi-layered thin-film structures comprised of ferromagnetic (FM) metal spaced by non-magnetic (NM) metal layers. Due to the decoupling imparted by the NM metal layers, magnetization of the FM layers can reverse independently. A strong MR effect was found upon switching the relative orientation of the FM film magnetic moments (parallel or anti-parallel alignment), which was an order of magnitude higher than MR effects seen in AMR-based devices [10, 11]. The fundamental mechanism behind the large MR signals obtained was the conservation of the spin orientation upon crossing the FM/NM interface. A giant MR effect arose when the NM spacer had its thickness comparable to the spin diffusion length, L_{sf}, of the electrons into the NM metal (usually copper).

Since this discovery, investigation of phenomena involving the spin of electrons has become a very active research area due to its rich physics and potential towards applications[12, 13], and has seen numerous ramifications along the last decade. Among them, the search for NM spacers offering more functionalities is noticeable. For instance, considerable efforts have been put in the use of inorganic semiconductors (e.g. Si, $GaAs$) due to their tuning capabilities and the possibility of realizing quantum computation logics [14–19]. Triggered by the demand of new technologies, another exciting research area has emerged that aims at integrating OSC materials with spintronics devices. Beyond the fascinating features offered by OSC, such as flexibility and low-cost

manufacturing, the characteristic that really attracted the spintronic community was the low atomic weight of the elements composing most OSC (e.g. C, H, N, O) [20]. Hyperfine (HI) and spin-orbit interaction (SOI) have been long known to be the main causes of spin scattering of electrons. Since spin-orbit interaction is proportional to Z^4, the spin life time in OSC is expected to be much longer than its inorganic counterparts (e.g. Si, Cu). Hyperfine interaction, which results from the interaction of electron spin with nuclear magnetic moments, still exists in OSC due to the presence of H atoms (nuclear spin $\frac{1}{2}$).[21] However, this interaction is considered to be very weak in comparison to the SOI component.

Another important aspect of OSCs are their intrinsically low carrier mobility ($10^{-5} - 10^1$ cm^2/Vs) and low carrier density. Charge transport in these materials is characterized by incoherent hopping between localized states. These states are so narrow that conduction cannot be treated by classical band theories. Charge transport through a narrow bandwidth (typically 0.1 eV [22]) around the localized molecular orbitals (HOMO – the highest occupied molecular orbital, or LUMO – lowest unoccupied molecular orbital) is generally followed by a distortion in the local molecular structure (polarons). Furthermore, disorder that is characteristic of polymer OSC complicates even more the charge transport due the creation of a larger density of trap states. Interestingly, despite of the low mobilities in OSC, relatively long spin diffusion lengths are obtained due to the long spin relaxation times, which can reach values in excess of 10 µs [20]. For small-molecule OSCs like rubrene crystals with optimized structure, for example, there are estimates that the spin diffusion length could be even larger than a millimeter [23].

1.2 Organic Semiconductors

It is intuitive for the understanding of organic semiconductors (OSC) to start a discussion from the basic constituents of this class of materials. Organic semiconductors, as any other organic material, are mostly constituted of carbon and hydrogen, but, to a lower extent, may also contain nitrogen, sulphur, oxygen, phosphorous, and fluorine atoms. OSCs are electrically insulating in their pristine state, but can be made conductive under the influence of external stimuli (e.g. electric field, temperature, doping).

An isolated carbon atoms has six electrons in its ground state. Four of them are located in the valence shell – two 2s, and two 2p orbitals. However, in order to achieve a more stable configuration when covalently bonded to other atoms, the wavefunctions of the s and p orbitals hybridize. In simple terms, the valence electrons try to be as far apart from each other in order to easily accommodate (less repulsion) adjacent

atoms. The hybridization type depends on the type and number of atoms carbon is bonded to, which ultimately defines the shape and properties of the molecules. Of particular interest for for today's OSCs is the sp^2 hybridization, which results from the hybridization of three carbon orbitals (2s, 2p$_x$, 2p$_y$) to form three identical trigonal-planar aligned sp^2-hybridized orbitals, with a 2p$_z$ orbital pointing out perpendicular to the plane. In a molecule, when sp^2-hybridized carbon atoms are adjacent to each other, the electron density of the neighboring localized 2p$_z$-atomic orbitals overlap to form a π-bond. Therefore, the electron wavefunction of these valence electrons can spread over the length of the molecule (*delocalization*), creating a way in which charge carriers can propagate in organic solids.
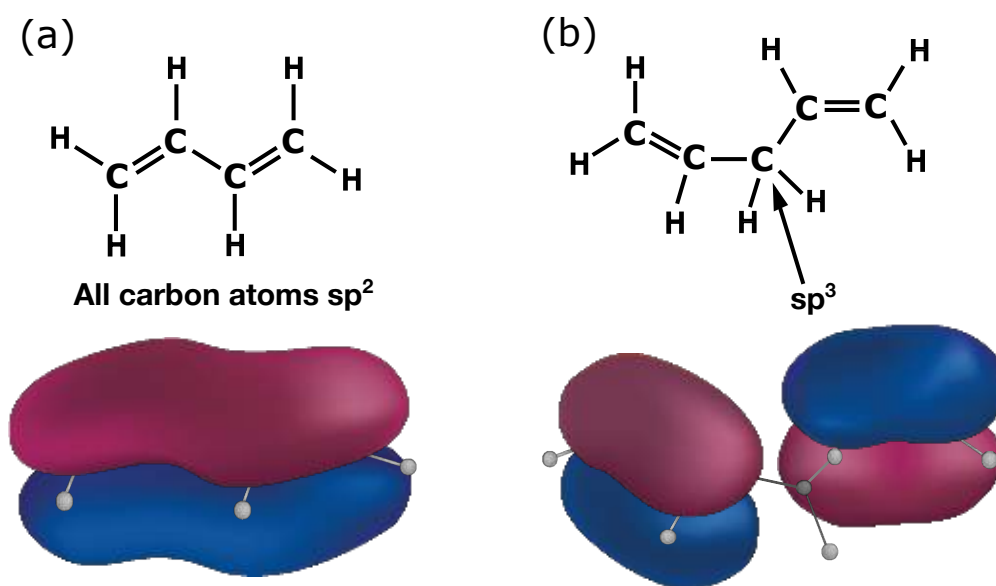
Figure 1.1: The molecular structure and π-orbitals of (a) 1,3-butadiene and (b) 1,4-pentadiene. For the latter, the presence of a sp^3 hybridized atom disrupts the electron delocalization.

As indicated in Figure 1.1(a), when a sequence of sp^2-hybridized carbon atoms are arranged in a chain, the delocalization of the wavefunction can extend over all the atomic units of the molecule. This is also known as π-conjugation, and is characterized by an alternation of single (σ) and double bonds (π and σ) in a molecule. The sp^2 hybridization is fundamental charge transport in organics. For instance, if an sp^3 carbon atom is present on the molecule the π orbital system is disrupted, compromising long-range charge transport, as illustrated in Figure 1.1(b).

The π-electrons in molecules can be viewed as a "particle-in-a-box" system from quantum mechanics. The electrons (particles) occupy discrete energy levels in the molecule (box). Of particular interest are the frontier quantum states, namely the highest occupied molecular orbital (HOMO), and the lowest unoccupied molecular orbital (LUMO).
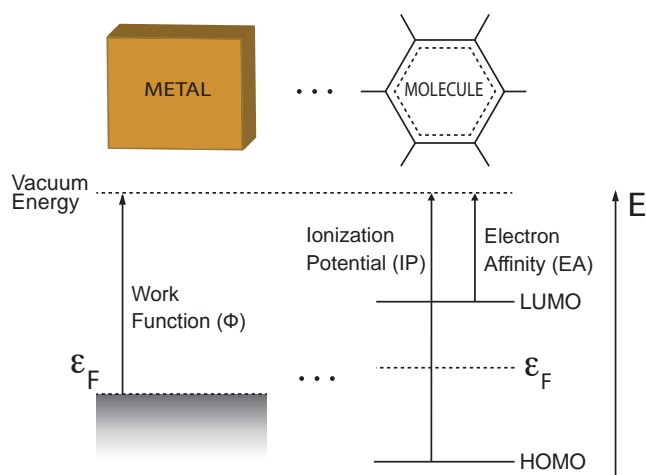
Figure 1.2: Band diagram for metals (left) and molecules (right).

The size of the π-conjugation determines the extent of confinement of the possible quantum states, which also in turn defines the HOMO-LUMO energy gap. The smaller the π-conjugation length, the higher will be the energy gap. For instance, benzene molecule with six sp^2 carbon atoms has an energy-gap of 6eV, while for molecules with larger π-conjugation such as Pentacene this value goes down to 2.1eV.[24] Simplified electronic band-diagrams of metal and molecules are illustrated in Figure 1.2.

Organic semiconductors can be further classified in two groups, which are normally refereed to as *small molecules* and *polymer semiconductors*. This distinction is important since the morphology, physical properties, and processing methods of OSCs can vary drastically depending on the molecular weight of the molecule. For instance, small molecules can be processed from the gas-phase (sublimation) and form very large crystals (e.g. rubrene), whereas polymer processing is largely done from solution and generally results in low crystallinity.

1.2.1 Polythiophene-based materials for Organic Electronics

In the previous section, it has been learnt that OSCs are mostly composed of a π-conjugated chain of hydrocarbons. Although these simple acyclic alkene structures have been fundamental for the understanding of charge transport in organic materials[2], it has found little use in real applications. For instance, doped polyacetylene was found to be highly unstable to oxygen exposure.[28] The appearance of carbonyl groups (or others)

---

[2]The discovery of electrical conductivity in polymers by H. Shirakawa, A. J. Hegger, and A. G. MacDiarmid[25] came from the study of a simple hydrocarbon polymer, the polyacetylene $(C_sH_s)_n$. A nice review of earlier achievements in the area of conducting polymers can be found in Refs. [26, 27]

upon air exposure highly degrades the electrical conductivity due to the formation of sp^3 units, therefore hindering its widespread use.

Figure 1.3: The chemical structure of polythiophene, with the reminiscent molecular structure of polyacetylene highlighted (*in violet*).

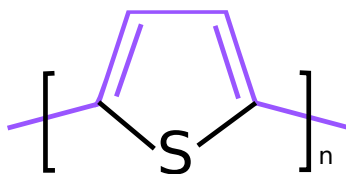The problem of these simple conjugated polymers is that their ionization potential (IP) is relatively low (4.7eV for polyacetylene), which renders the OSC prone to attack from oxidative species such as oxygen. Several metals have IPs of similar magnitude of that of polyacetylene. However, oxygen is able to diffuse easily into the bulk of polymeric materials, whereas in most metals a protecting passivating oxide layer is formed at its surface. To solve this issue, several alternative polymers have been put forward, such as polyphenylenes, polyanilines, and polythiophenes. The aromaticity of these compounds confers very good chemical and thermal stability, as compared to the chain in extended polyacetylenes. Among them, polymers based on thiophene heterocycles enjoy high IP (>5eV), together with remarkable flexibility for synthetic manipulation. The basic chemical structure of polythiophenes is shown in Figure 1.3. The sulphur atom in the thiophene monomer has two lone electrons pairs, one *sp^2*-hybridized and another non-hybridized *p* orbital, which participates in the cyclic six electron π-system. It interesting to note that the molecular structure of this polymer is similar to polyacetylenes (highlighted in the figure), but with raised energy levels due to the heterocycle and aromacity.

Polythiophenes are insoluble and infusible, so in the early days it was synthesized exclusively by electropolymerization.[29] The resulting material was amorphous and had poor electrical performance.[5] It was later discovered that adding an alkyl side chain to the thiophene heterocycle allowed the synthesis of this polymer with standard synthetic chemical methods.[30] In 1995, this method was perfected in order to synthesize soluble regioregular alkyl polythiophenes – e.g., the Poly(3-hexylthiophene-2,5-diyl) (rr-P3HT).[31] The regular ordering of alkyl sidechains promoted dramatic improvement in the polymer packing organization, which led to over three orders of magnitude improvement in its carrier mobility.

The following sections describes the two polythiophene-based materials studied in this thesis, namely the poly(2,5-bis(3-hexadecylthiophen-2-yl)thieno[3,2-b]thiophene (pBTTT),

and the poly(3,4-ethylenedioxythiophene):poly(styrenesulfonate) (PEDOT:PSS). Although their chemical structure and properties are remarkably different, both polymers share a thiophene-based backbone.

Poly(2,5-bis(3-hexadecylthiophen-2-yl)thieno[3,2-b]thiophene) - pBTTT

Further development of polythiophene-based materials has been achieved recently by McCulloch *et al.* [32]. In order to improve the mobility of carriers in this polymer they successfully performed a few changes in the monomer structure. On the one hand, they introduced regiospecifically the linear conjugated thieno[3,2-b]thiophene structure in the monomer. On the other hand, rather few alkyl chains are present in this polymer, as seen in Figure 1.4, but the presence of the rigid and planar thieno[3,2-b]thiophene co-monomer confers superior π-stacking ability with adjacent chains. Besides promoting enhanced intermolecular charge transport, this fused thiophene heterocycle also increases the IP (5.1eV) due to resonant stabilization, giving the polymer better chemical stability. Furthermore, the reduced density of alkyl side groups critically reduces steric hinderance caused by excessive volume of side chains.

This molecular architecture gives the polymer a liquid-crystalline behaviour, allowing it to form highly crystalline thin-films. As seen in the atomic force microscopy image of Figure 1.4, the pBTTT tends to form large two-dimensional (2D) terrace-like sheets after appropriate annealing. Thin-films of pBTTT are composed of several stacks of molecular crystals aligned edge-on with the surface. This molecular arrangement is highly interesting for situations in which 2D charge transport is required. This is the case for field-effect transistor devices, in which charge carriers takes place almost exclusively at the first semiconducting layer interfacing the gate dielectric. In fact, pBTTT has one of the highest reported field-effect mobilities to date for polymer transistors, amounting to $1cm^2V^{-1}s^{-1}$ in optimized devices. Moreover, the HOMO-LUMO gap of pBTTT is 2eV, conferring its semiconducting behavior and very good current on-off ratios (10^7-10^{-9}).

Poly(3,4-ethylenedioxythiophene):poly(styrenesulfonate) - PEDOT:PSS

Now we turn our attention to another polythiophene-based OSC investigated in this thesis, namely the poly(3,4-ethylenedioxythiophene) (PEDOT). In contrast to the pBTTT discussions of the previous section, this material is designed to show ohmic instead of semiconducting behavior. However, as it has been already discussed, polythiophenes are natively semiconducting and have a large bandgap at the Fermi energy level. Therefore,
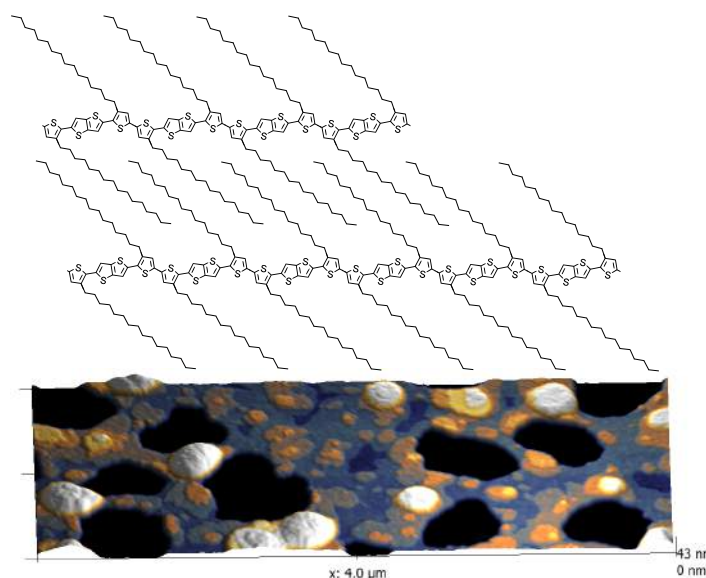
Figure 1.4: The chemical structure of pBTTT and a representation of its terrace-like molecular stacking (*top*). In the (*bottom*), an atomic force microscopy image of an dewetted pBTTT thin-film. The dark areas in the image represent the sample substrate. The large pBTTT terrace stacks are clearly visible in the image, together with white bumps resulted from the dewetting process. The substrate consists of an ultra-smooth (R_q=0.2) atomic-layer deposited AlOx treated with highly hydrophobic octadecylphosphonic acid self-assembled monolayer.

in order to render this material electrically conductive, oxidative doping is normally carried out.

An alternative, but elusive route to obtain metallic-like conductivity in OSC is to design conjugated molecules with very low, or ideally zero energy bandgap.[33] The problem with this strategy is that in order to suppress the bandgap, the HOMO level must be increased concurrently with a LUMO level decrease. Although materials with very low bandgaps can be synthesized, they are highly unstable in air due to the very low IP. PEDOT, however, has been designed in order to have decent environmental stability, and therefore possesses an intermediate energy bandgap of 1.6eV (2eV for pristine polythiophene), which also implies that it must be doped to become conductive.

The widespread success of PEDOT as conducting material is the result of an ingenious molecular engineering of its monomer, the 3,4-ethylenedioxythiophene (EDOT).[34, 35] As seen in Figure 1.5, the EDOT consists of a simple thiophene ring fused to an oxygen-containing ethylenedioxy heterocycle. The substitutions at β positions completely eliminates non-α polymerization reactions, allowing the synthesis of high-quality stereoregular polymer chains. The insertion of strong electron-donating groups (ether) at the 3,4 β-positions decreases the oxidation potential of the molecule, together with a relative

increase of the reactivity at the alpha α sites for polymerization.[36] The reduced oxidation potential of the monomers translates in improved stability of its radical cations. Note that radical cations (polarons or bipolarons) form the basis for electrical conduction, which for PEDOT is engineered for stability. Another aspect is that the ether groups at the β positions are covalently bonded forming a rigid, planar heterocycle. This rigid architecture avoid steric distortions of the π-system, of an otherwise singly or non-cyclic doubly substituted thiophene. This, together with the cationic mesomeric stabilization of the π-conjugation promoted by the oxygen and sulphur atoms, leads to reduced bandgaps. Therefore, the synergy between planarization, extension of π-conjugation, and electron-donating substitution allows hole-conducting polymers with high stability and relatively low energy bandgap.
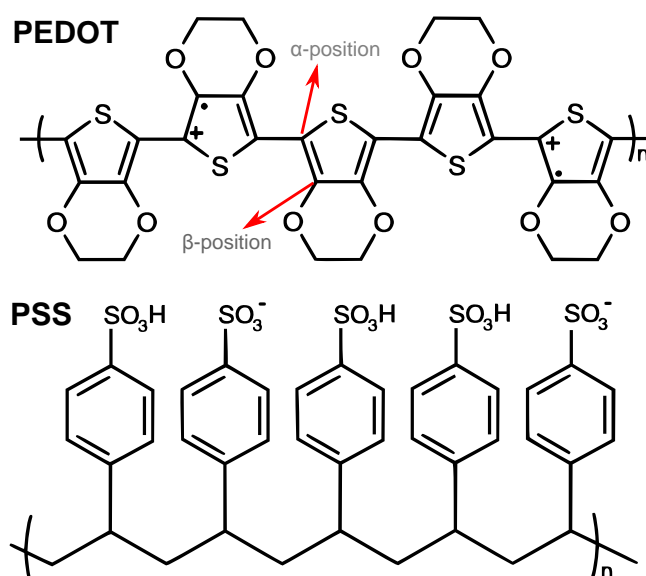
Figure 1.5: The chemical structure of PEDOT:PSS. In the fully doped state, this conducting polymer has one positive charge (*e* hole) for each three EDOT rings.

Although the EDOT monomer is soluble in water, the PEDOT resulting from electrochemical or oxidative polymerization is not. Therefore, PEDOT is normally synthesized in its doped form, wherein the dopant counterion simultaneously confers conductivity and solubility. Several acids qualify as dopants for conducting polymers, being the most used the polystyrenesulfonic acid (PSS). The strong acidity of its sulfonic acid groups, its solubility in water, its excellent film-forming properties, its transparency to light in the visible spectral range, make PSS an industrial standard for PEDOT:PSS manufacture.

1.3 Outline of this Thesis

In this thesis, nanoscale hybrid organic-inorganic nanostructures are investigated as components of functional electronic devices. Two topics are covered in this work. The first topic deals with organic spin-valves, a novel concept that allow information storage in organic electronic devices. The work serves as basis for the understanding of integration of conductive polymers with with ferromagnetic materials and spin-transport phenomena in nanoscale lateral devices. The second topic addresses organic thin-film transistors, which allow the manufacture of logic integrated circuits via low-cost fabrication methods (e.g. solution processing). A thorough experimental investigation on self-assembled monolayer based gate dielectrics and its interaction with highly-crystalline polymer semiconductors is presented. Another important aspect covered in this thesis is device miniaturization. Reducing devices to nanoscopic dimensions not only can improve known properties, but can give rise to novel functionalities. For instance, reducing OFET channel lengths (L) can improve the maximal operation frequency (f) of these devices since $f \propto 1/L$. In the case of organic spintronic devices, nanometric scale manufacturing is imperative for its functionality since spin diffusion lengths in these materials are relatively short.

This thesis is organized as follows. In Chapter 2, a general overview of the concepts and theory behind electron transport processes in organic semiconductors is presented. Emphasis is given to charge transport models and equations utilized throughout this work, for both pristine and highly doped organic semiconductors. The fundamentals of spin injection, transport and detection in semiconductors are thoroughly described. This additionally includes relevant information regarding spin injection with finite interface resistances, device architecture, and its implications to organic spintronics. Chapter 3 is devoted to the experimental methods developed for the fabrication of high-quality organic electronic devices, which included laterally patterned spin-valves and OFETs. The characterization techniques and details of organic semiconductor processing are also presented. In Chapter 4 a comprehensive study on the spin and charge transport processes in lateral spin-valves based on PEDOT:PSS is presented. Charge transport of PEDOT:PSS is studied with both ohmic and spin-polarized tunneling electrodes at nanometric dimensions, wherein it is demonstrated that conductivity in these confined dimensions scales non-linearly with nanoelectrode spacing. Magnetotransport measurements along with device modelling allowed the estimation of an upper limit for the spin lifetime in this conducting polymer. In Chapter 5, a novel ultra-thin hybrid gate dielectric based on mixed-type phosphonic-acid SAM is introduced. SAMs containing carboxylate and/or methyl-terminated molecules are studied with respect to

their surface energy and leakage current levels. It is found that by simple improvement in the assembly process, one can obtain high surface energy, while retaining the low-leakage levels that was previously observed only in pure alkyl-terminated SAMs. The electrical characteristics of TFTs based on pBTTT, and the impact of the underlying mixed-SAM dielectrics on the polymer morphology are presented. Chapter 6 extends the mixed-SAM approach for TFTs with highly scaled channel lengths (L∼30nm). As it is demonstrated, the average diameter of pBTTT nanocrystallites compares to the lateral dimensions of the device, allowing TFT operation with a few crystallites. Moreover, given the high capacitive coupling obtained with ultra-thin AlOx/mixed-SAM dielectrics, the pBTTT nanotransistors are operated at very low-voltages (<3V) with good on/off ratios. Finally, a summary of the findings of this work and an outlook of possible research directions are given in Chapter 7.

2 Fundamental Background

In this chapter, the concepts necessary for the understanding of charge and spin transport in organic semiconductors are briefly described. The basic theory of hopping transport, field-effect transistors, and spin-polarized transport are also reviewed, providing the reader the necessary knowledge for the following chapters.

2.1 Charge Carrier Transport in Organic Semiconductors

Organic semiconductors have been introduced in Chapter 1, with special focus on the relationship between chemical structure of individual molecules and their electronic properties. Although electronics with single molecules is an active research topic[37], this thesis concerns exclusively with condensed matter in the solid state. For electron transport at larger scales, which may be determined by the device dimensions, intermolecular electronic transport becomes as important as intramolecular transport. For example, the electronic coupling between two π-stacked tetracene molecules has been shown to dramatically vary with small relative lateral displacement, and in some cases completely halting the intermolecular charge transfer.[38] Due to the sensitivity to molecular packing, the OSC that showed the best charge carrier mobility to date was ultra-pure single-crystalline aligoacenes, reaching mobilities in excess of $30\text{cm}^2\text{V}^{-1}\text{s}^{-1}$ at room-temperature and even exhibiting band-like[1] transport characteristics.[39]

Unfortunately, obtaining ultra-purified materials and fabricating devices based on organic single-crystals are challenging. In fact, the vast majority of OSCs exhibit some degree of disorder, braking the crystalline packing symmetry. This is specially true for organic molecules since in its great majority display complex and asymmetric shapes. Spatial and energetic disorder induces localization of the electron wave-function, thereby

---

[1]This represents the availability of a continuous band of allowed energy states for electrical transport, which contrasts with the discrete set of energy levels normally found in isolated molecules and atoms.

reducing the intermolecular electronic coupling and consequently the carrier mobility. In the framework of the Anderson localization, one may consider OSCs invariably insulators since their electronic states are localized. However, as it is observed, carrier transport in highly disordered electronic systems can occur. Indeed, increasing the level of disorder deteriorates the charge mobility since the Fermi energy level shifts deeper into the band-gap. But, even in this situation, thermally-assisted or direct tunneling between localized states can generate sizeable electrical currents. Therefore, the charge transport in disordered OSC is dominated by hopping of charge carriers between localized states, which is also known as *hopping transport.*
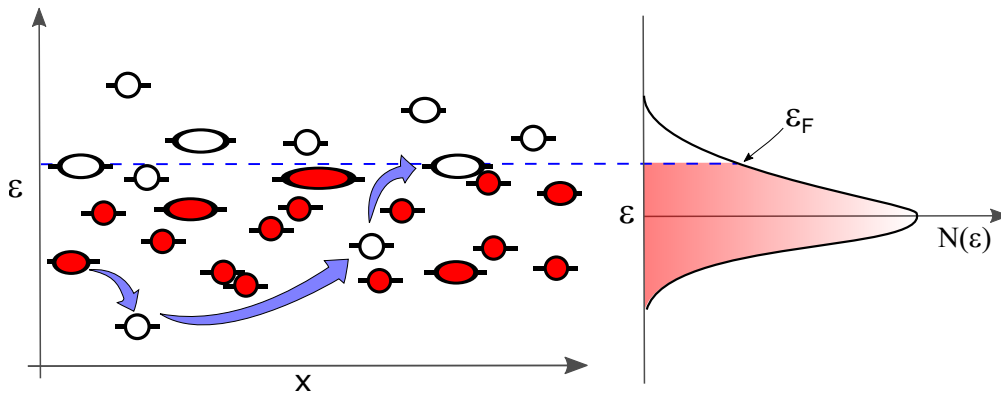
Figure 2.1: Simplified one-dimensional representation of the hopping conduction. (*left*) An array of empty (white) and occupied (red) electronics states near the Fermi energy level, ε_F. Charge carriers may hop upwards or downwards in energy, in a variable range of distances. On the (*right*), the distribution of the density of states with respect to the energy level.

A simplified one-dimensional view of the hopping carrier transport is shown in Figure 2.1. Filled (*red*) and empty electronic states (*white*) are scattered both spatially and energetically near the Fermi energy level ε_F. The *density of states* $N(\varepsilon)$ of this hypothetical electronic structure is also shown, which represents the population of carriers at a given energy level. As represented in the figure, in some regions the wave-function delocalization can extend over large lengths, while in other places the state is localized. A charge carrier may jump from an occupied to an empty state with a given external perturbation. If the available thermal energy is sufficient, carriers can diffuse between states by simple thermal activation. Alternatively, an external bias can be applied in order to drive carrier hopping between localized states. The rate at which charge hops is related to the concept of charge carrier mobility (with unit $cm^2V^{-1}s^{-1}$). Carrier mobility is a material parameter that correlates the mean drift velocity v_D of carriers and the applied electric field $\vec{E}$. Moreover, the hopping rate and/or mobility determines the conductivity σ of the material,

$$\sigma = e \cdot (n_{holes} \cdot \mu_{holes} + n_{electrons} \cdot \mu_{electrons}) \tag{2.1}$$

where e is the fundamental electric charge, and n is the carrier concentration (electron/hole charge carrier). If, for example, the charge transport is exclusively via holes, the Eq. 2.1 would reduce to $\sigma = e \cdot n_{holes} \cdot \mu_{holes}$. Since the materials studied in this thesis are exclusively hole conductors, the subscript index *holes* will not be used hereafter.

2.1.1 Variable-Range Hopping Transport

Modelling the problem of charge transport in disordered materials can be done by computing all the available electronic states, and the probability evolution of charge carrier hopping from a state i to a remote state j. This approach is clearly prohibitively complicated, since one should input the unknown distribution of all electronic states in real space, and also information about the wavefunction decay lengths. Another fundamental parameter is the overlap between the decaying wavefunctions of adjacent sites. Overlapping wavefunctions is necessary since it allows charge tunneling, and consequently compute the transitions rates W_{ij} from site to site[40, 41],

$$W_{ij} = \upsilon_o \exp\left(\frac{-2|R_{ij}|}{\xi}\right) \begin{cases} \exp\left(-\frac{\varepsilon_j - \varepsilon_i}{k_B T}\right) & \forall \varepsilon_j > \varepsilon_i \\ 1 & \text{else,} \end{cases} \tag{2.2}$$

where R_{ij} is the distance between site R_i and the R_j, υ_o the phonon vibration frequency, ξ the localization radius, and k_B the Boltzmann constant. The ξ is the result of the overlap of the wavefunction of states i and j. The pre-expontial factor υ_o can be interpreted as an "attempt-to-jump" factor, as it relates to the phonon-assisted tunneling between states. As can be understood from Eq. 2.2, the hopping rate is exponentially dependent both on the distance between the two sites, and on the energy penalty of the $i{\rightarrow}j$ transition. This energetic penalty is absent for charges hopping downward in energy. Since the hopping conduction is directly related to phonon-assisted tunneling processes, it is worth pointing out that when the charge must surpass an energetic barrier, it does so by absorbing a phonon from the acoustic bath. Conversely, if the final state has lower energy, the charge transit results in phonon emission.

The breakthrough on hopping conduction came when Sir Nevill F. Mott realized that the energy penalty (activation energy) for charge transfer is not necessarily a material constant, but varies for systems with localization radii ξ near the metal-insulator tran-

sition or at sufficiently low temperatures.[42] This implies that charge carriers do not hop exclusively to nearest neighboring states, as previously assumed, but can jump to locations that are farther than the average distance between states. In other words, it can happen that when the charge carrier attempts a jump, it could be more energetically favorable to look for remote states, rather than jumping upwards in energy in the nearest states. This phenomena is specially true at low temperatures, since acoustic phonon are drastically suppressed. For this reason, the highly acclaimed Mott's model takes its name – variable-range hopping (VRH) conduction.

As previously discussed, charge carriers hop at or near the Fermi level, where both empty and occupied states are present. The hopping system can then be described by a band-width $\Delta\varepsilon$ where the states for conduction are available. In order to simplify the calculations, Mott assumed an uniform density of states near the Fermi energy. Following this approach, the carrier concentration available for transport $N(\varepsilon_F)\Delta\varepsilon$ can be directly derived. Therefore, setting an arbitrary distance R, at any given energy spread would result in $\frac{4}{3}\pi R^3 N(\varepsilon_F)\Delta\varepsilon$ potential target sites available for charge hopping. If hopping conduction is possible, at least one unoccupied site exists within range, which is enforced by the equation[43],

$$\frac{4}{3}\pi R^3 N(\varepsilon_F)\Delta\varepsilon \cong 1. \tag{2.3}$$

Equation 2.3 is at the heart of Motts theory, since it connects both the spatial (R) and energetic ($\Delta\varepsilon$) terms of the variable-range-hopping conduction with the DOS of the material. With this in mind, the transition rates for charges hopping upward in energy (from Eq. 2.2) can be rewritten as

$$W(R) = v_o \exp\left(\frac{-2R}{\xi} - \frac{1}{k_B T \frac{4}{3}\pi R^3 N(\varepsilon_F)}\right), \tag{2.4}$$

where the equation is function of R only. Note that Eq. 2.4 can be also rewritten as function of energy, W($\Delta\varepsilon$). In order to find the best possible path the charge carrier would take in this percolating electronic system, one must find the situation in which the transition rates from site-to-site are maximized. Or, in other words, what is the optimal hopping lengths and energy band-widths the charge carriers will have in order to minimize the transport energy. This is straightforwardly done by taking the derivative of Eq. 2.4 with respect to R, $\frac{dW(R)}{dR} = 0$, or similarly repeating this for the transition rates as function of energy band-width. From these calculations, the optimal hopping length and energy band-width functions can be derived,

$$R_{optimal} = \left(\frac{\xi}{8k_B\pi N(\varepsilon_F)} \frac{1}{T} \right)^{\frac{1}{4}} \text{and}$$

$$\Delta\varepsilon_{optimal} = \frac{3}{4} \left(\frac{\left(8k_BT/\xi \right)^3}{\pi N(\varepsilon_F)} \right)^{\frac{1}{4}}. \tag{2.5}$$

When Equations 2.5 are substituted in Eq. 2.4, the fastest and energy-efficient route for the transport process is found, W_{max}. From this optimization, Mott arrived in his famous generalized VRH conductivity equation[44],

$$\sigma\left(T\right) \propto W_{max} \propto \exp\left[-\left(\frac{T_0}{T} \right)^{\frac{1}{1+D}} \right], \tag{2.6}$$

wherein T_0, generally refereed to as the characteristic temperature, envelopes most of the variables of Eqs. 2.5 and 2.4, and D is the dimensionality factor (D=3 in the previous discussions for three-dimensional electronic system). Also note that in order to obtain the total current crossing the sample, one simply needs to multiply the hopping rates by the electron charge e. Knowing the charge electrical current value, one can directly compute the equation in terms of conductivity (or resistivity). The characteristic temperature can be obtained with,

$$T_0 = \frac{\beta_D}{k_B N(\varepsilon_F)\xi^D}, \tag{2.7}$$

wherein β_D is a numerical coefficient used as correction[45] for Mott's assumption in Eq. 2.3, which also depend on the dimensionality of the hopping process. The VRH theory will be further discussed in Chapter 4, where it will be applied to interpret the charge carrier transport of an highly conductive polymer, the PEDOT:PSS.

2.2 Organic Field-Effect Transistors

A field-effect transistor is a three terminal electronic device used to control electrical currents (*output*) with a voltage (*input*). It is comprised of a gate, source and drain electrodes. Source and drain electrodes are contacted to a semiconducting material, whereas the gate is capacitively coupled to the semiconductor across a dielectric, refereed to as gate dielectric. The device configuration used in this thesis is shown in Figure 2.2. When an electric potential is applied to the gate electrode, the resistance of

the semiconductor can be modulated, allowing charge carriers to flow (or not) between source and drain terminals, I_{sd}. The source electrode has fixed reference potential, and in this thesis is kept grounded (0V). By applying a gate-source potential, V_{gs}, the valence (*or* HOMO) or conduction band (*or* LUMO) is bent towards the Fermi energy level, and the density of states for transport is generated at the gate dielectric/semiconductor interface, which can be filled with mobile charge carriers.
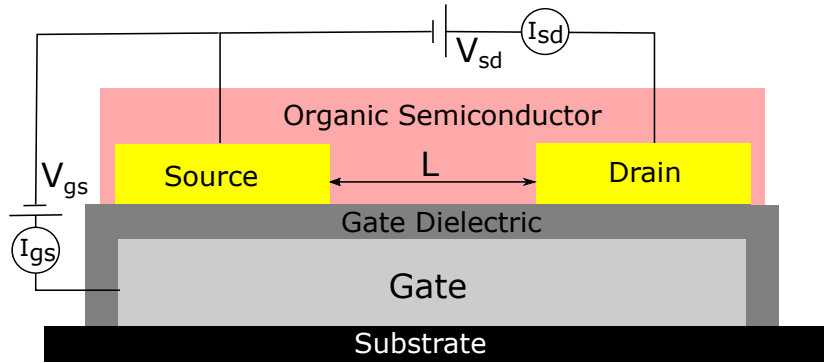
Figure 2.2: **Schematic of a field-effect transistor** and typical electrical interconnections. The device shown has a bottom-contact, bottom-gate electrode configuration, which is used throughout this thesis.

The current-voltage characteristics of a FET can be described by,

$$I_{sd} = \frac{\mu C_i W}{L} \left((V_{gs} - V_{th}) V_{sd} - \frac{V_{sd}^2}{2} \right) \text{ for } |V_{gs} - V_{th}| > |V_{sd}|$$

$$(linear\ regime)$$

$$I_{sd} = \frac{\mu C_i W}{2L} (V_{gs} - V_{th})^2 \text{ for } |V_{sd}| > |V_{gs} - V_{th}| > 0$$

$$(saturation\ regime)$$

(2.8)

for the linear and saturation regimes, wherein the currents and voltages of the expressions are labeled in Figure 2.2, C_i is the capacitance per unit area of the gate dielectric, and μ the carrier mobility, L the channel length, and W the channel width (not indicated in the schematics). The *threshold voltage*, V_{th}, in an ideal FET is zero. However, given the mismatch between the work-functions of contacts and the semiconductor conduction states, and the presence of traps at the gate dielectric/semiconductor interface, this value is finite. In other words, an energy barrier must be surpassed to allow long-range charge transport. The threshold voltage is an important parameter, since it marks the transition between off-state operation regime to the *subthreshold* region. In this region, the charge density, or density of states (if no charge reservoir is present), depends exponentially on V_{gs}. The slope of the drain current in this operation regime

is denoted as the *subthreshold swing*, and is described by,

$$S_{s-th} = \frac{k_b T}{e} \ln 10 \left(1 + \frac{e N_{trap}}{C_i}\right) \tag{2.9}$$

wherein N$_{trap}$ represents the density of trap states at the dielectric/semiconductor interface. It is evident from Eq. 2.9 that in order to improve the switching of the FET, the dielectric capacitance should be increased, and the trap states should be reduced. The theoretical minimum for the subthreshhold swing at room-temperature is 60mV/decade.[46] The carrier field-effect mobility is given by,

$$\mu_{lin} = \frac{L}{C_i W V_{ds}} \frac{dI_{ds}}{dV_{gs}} \; (linear \; regime) \tag{2.10}$$

and

$$\mu_{sat} = \frac{2L}{C_i W} \left(\frac{d\sqrt{I_{ds}}}{dV_{gs}}\right)^2 \; (saturation \; regime) \tag{2.11}$$

can be straightforwardly computed by evaluating the drain-source current versus the gate-source voltage behavior of the device (*transfer characteristics*).

The equations above are derived for an ideal metal-insulator-semiconductor (MIS) structure, in which the dielectric is considered to be a perfect insulator. However, the dielectrics are in reality leaky – a significant current density exists, the I$_{gs}$. This so called *leakage current* is an important device parameter since the standby power consumption of integrated circuits are derived from it. The power requirements of a device also strongly depend on the capacitance C$_i$ of the dielectric layer (see also Eqs. 2.8), which is given by

$$C_i = \frac{\varepsilon_0 \varepsilon_r}{t} = \frac{Q}{V_{gs} - V_{th}}, \tag{2.12}$$

wherein Q is the surface charge density at the dielectric/semiconductor interface, ε_0 is the vacuum permittivity, ε_r the relative permittivity of the dielectric, and t is its thickness. To lower power consumption while keeping the same device properties, input voltages should be decreased – therefore, the capacitance per unit area must be increased. This is obtained by using dielectrics with high permittivities and/or thinner dielectric layer. This theme will be further discussed in Chapter 5, where an ultrathin hybrid gate dielectric based on mixed self-assembled monolayers is presented.

2.3 Basics of Spin Transport

Spin Electronics dates back to the mid-thirties, when Mott [47] postulated that that electron transport in ferromagnetic (FM) transition metals should be treated as being carried in two independent channels, with different transport properties. The basic assumption was that electron spin mean free path, λ_{sf} (*sf* stands for spin-flip), in metals is much larger than the mean free path, λ, of the electron itself. The illustration in Figure 2.3 represents Mott's ideas: a spin-up electron travelling through a metal suffers several scattering events in the crystal lattice before flipping its spin down. This spin-flip event is, however, rare in most elementary FM metals such as Ni, Co, Fe, and its alloys. Therefore in the $\lambda_{sf} \gg \lambda$ limit, spin currents can be treated independently of each other. However, having two independent spin channels alone does not suffice to explain the anomalies in the transport characteristics observed in FM metals (e.g. anisotropic magnetoresistance). From its electronic structure it becomes clear that these two spin channels have very different electronic transport properties.
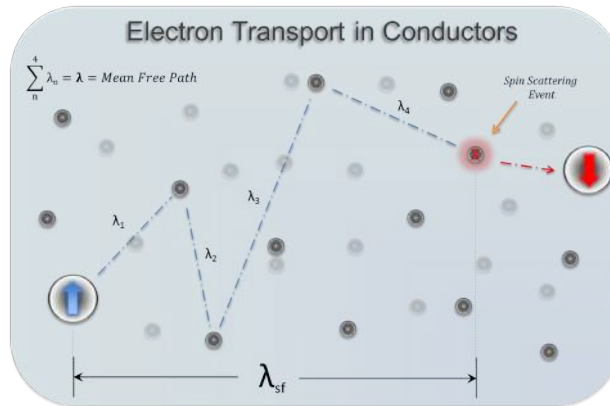
Figure 2.3: Illustration of electron diffusion in metals. Electron undergoes several momentum scattering events before loosing its spin information. The average of momentum scattering events gives the electron mean free path λ, which is much smaller than the electron-spin mean free path λ_{sf}. As a result, in ferromagnetic metals spin-up and spin-down electrons can be treated independently.

According to the Pauli exclusion principle, the wave function of two or more electrons has to be antisymmetric with respect to the spatial exchange of any two electrons. Therefore, the symmetry (or asymmetry) of the spin part of the wave function influences the total energy of the system. This energy is known as exchange energy, E_{ex}. The consequence of this exchange interaction in transition metals is the splitting of the d orbital in two spin sub-bands. This spin asymmetry imparts a very different topology of the Fermi surface for spin-up and spin-down carriers. Figure 2.4(a) depicts a simplified

illustration of the electronic density of states (DOS) in ferromagnetic transition metals (e.g. Co, Ni, Fe, and its alloys). In this materials the valence states are constituted of *s* and *d* electrons. Spin-split electrons of the 3d orbitals have localized wave functions and do not contribute to the charge transport. While the spin imbalance imparts a net ferromagnetic moment, the conduction is dominated by the un-split 4s delocalized and hybridized bands [48].

(a)   (b)
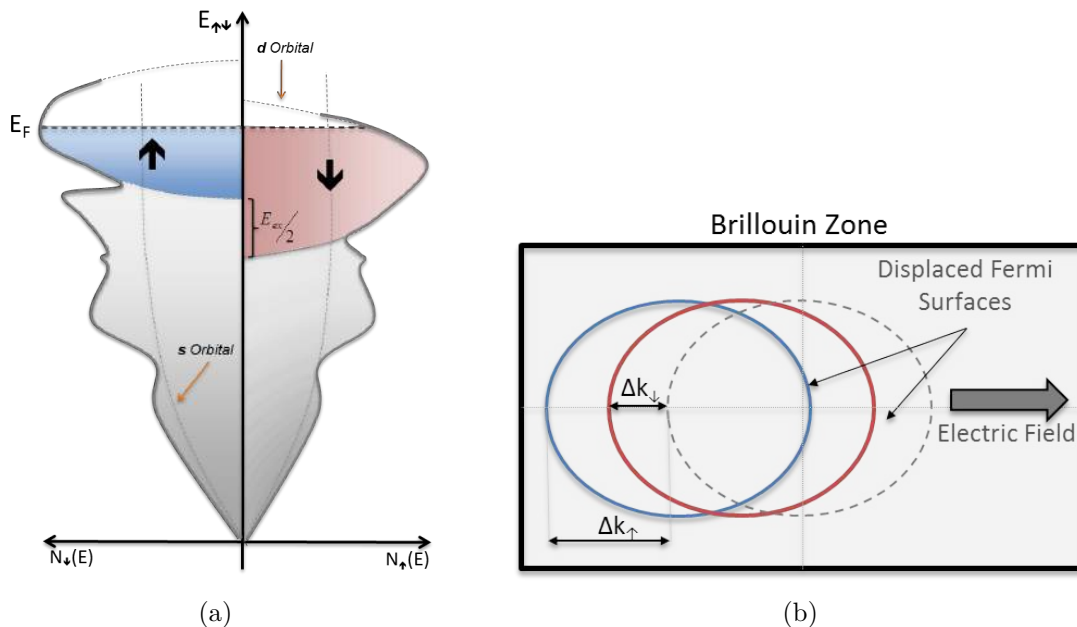
Figure 2.4: Schematic illustration of transition metal ferromagnetic materials electronic density of states (DOS) (a) and its Fermi surface under applied electric field, (b).

The origin of spin-polarized currents in ferromagnetic metals is, however, different. It results from the *s*-*d* interband exchange interaction, that gives rise to different spin-flip scattering probabilities, and different Fermi velocities for each spin entity [49, 50]. Consequently, upon application of a perturbation to ferromagnetic transition metals (e.g. termoelectric, electric, magnetic potential), one has spin-dependent shifts in momentum space due to the different electron conductivities, which corroborates to the validity of the two spin current model. This is depicted in Figure 2.4(b). In this model – valid for diffusive transport –, the spin-dependent bulk conductivities are associated to the DOS via the Einstein relation:

$$\sigma_{\uparrow,\downarrow} = e^2 N_{\uparrow,\downarrow} D_{\uparrow,\downarrow} \quad \text{with} \quad D_{\uparrow,\downarrow} = \frac{1}{3} v_{F\uparrow,\downarrow} l_{e\uparrow,\downarrow} \tag{2.13}$$

where e is the absolute value of the electronic charge, $N_{\uparrow,\downarrow}$ is the spin-dependent DOS at the Fermi energy, $D_{\uparrow,\downarrow}$ the spin-dependent diffusion constants, $v_{F\uparrow,\downarrow}$ the spin-dependent

Fermi velocity, $l_{e\uparrow,\downarrow}$ the spin-dependent electron mean free path. The current spin polarization in ferromagnetic metals can thus be defined as:

$$\alpha_{\mathrm{F}} = \frac{\sigma_\uparrow - \sigma_\downarrow}{\sigma_\uparrow + \sigma_\downarrow} \tag{2.14}$$

The sign and magnitude of spin polarization can be measured by Andreev reflection experiments [51], yielding a spin polarization in the range 0.3–0.7 in conventional ferromagnets [52, 53]. Half-metallic materials, such as $La_{1-x}Sr_xMnO_3$ and CrO_2, can reach polarization values in excess of 0.96 [54], however, at very low temperatures [55]. The reason for this giant spin polarization is that in half-metallic materials charge density drops to zero in one of the spin sub-bands. In spite of its attractive properties, difficult fabrication processes and degrading properties near room temperature prevent wider use of half-metallics in spintronic applications. In this thesis, only metallic ferromagnets are considered due to their high Curie temperatures.

2.3.1 Spin injection and Spin accumulation at FM/NM interfaces

We now move to the case where ferromagnetic (FM) metal interfaces non-magnetic materials of comparable conductivity (NM). This is schematically illustrated in Fig. 2.5. Current flows perpendicular to the plane, crossing the FM/NM interface, under the influence of an electric field $\vec{E}$. The current in the FM metal is spin-polarized ($J_\uparrow^{FM} \neq J_\downarrow^{FM}$), as a result of the its spin-dependent conductivities ($\sigma_\uparrow^{FM} \neq \sigma_\downarrow^{FM}$). In contrast, electron-spin conductivities at the NM side is identical ($\sigma_\uparrow^{NM} = \sigma_\downarrow^{NM}$) given the absence of spin-imbalance in its electronic structure. As a result, the conservation of spin-polarized current density across the interface $\vec{\nabla} \cdot \vec{J}_{tot} = 0$ is compromised, and the system goes out of thermodynamical equilibrium near the interface. A spin accumulation zone is formed due to the pile-up of imbalanced electron spins, which extends by L_{sf}^{FM} into FM, and L_{sf}^{NM} into the NM side. In this spin accumulation zone the Fermi level of spin-up and spin-down carriers is split in order to induce spin-flips near the interface and balance the spin charge density:

$$\vec{\nabla}\vec{J}_{\uparrow,\downarrow} = -\vec{\nabla}\vec{J}_{\downarrow,\uparrow}. \tag{2.15}$$

Fermi level splitting and spin flipping adjustment takes place in both, FM metal and NM material. Consequently, a net spin-polarized current is induced in the NM side, with a characteristic diffusion length L_{sf}^{NM}. While the diffusion length is generally

short in the FM side (e.g. $L_{sf}^{Co} = 59$ nm [56]), it can be very long in the NM side due to a much lower concentration of spin scattering centers (e.g. $L_{sf}^{Cu} = 1$ μm [57], $L_{sf}^{CNT} = 50$ μm [58], $L_{sf}^{Si} = 100$ μm [19]).

To understand the spin accumulation near the interface, one has to describe the current in terms of electrochemical potentials of the spin polarized electrons [59, 60]. Electron transport is driven by a gradient of electrochemical potential for both spin species,

$$\boldsymbol{\nabla}\mu_{\uparrow,\downarrow} = -e\vec{J}_{\uparrow,\downarrow}/\sigma_{\uparrow,\downarrow}, \tag{2.16}$$

where $\boldsymbol{\nabla}\mu_{\uparrow\downarrow}$ represents the local variation of the spin-dependent electrochemical potential $\mu_{\uparrow\downarrow}$, $\sigma_{\uparrow\downarrow}$ is the spin-dependent conductivity, and e is the electron charge. The spin accumulation, which is described by $\Delta\mu=\mu_{\uparrow}-\mu_{\downarrow}$, is maximal at the FM/NM interface due to the Fermi level splitting, and falls to zero at $\pm\infty$, as shown in Fig. 2.5(a). As shown in Refs. [60–62], the spin polarization of the current density across the FM/NM interface can be described by

$$\left(\frac{\vec{J}_{\uparrow} - \vec{J}_{\downarrow}}{\vec{J}_{\uparrow} + \vec{J}_{\downarrow}}\right)^{FM/NM} = \frac{\beta}{1 + {r_{NM}}/{r_{FM}}}, \tag{2.17}$$

where β is the spin-polarization of the FM metal, and r_{FM} and r_{NM} are given by the products of the resistivity with the spin diffusion length the FM and NM materials, respectively,

$$\begin{aligned} r_{FM} &= \rho_{FM} \cdot L_{sf}^{FM}, \\ r_{NM} &= \rho_{NM} \cdot L_{sf}^{NM}. \end{aligned} \tag{2.18}$$

Evaluating Eq. 2.17 one directly observes that if $r_{NM} \gg r_{FM}$, the spin injected through the interface becomes vanishingly low. This happens because the spin accumulation generated at the interface is equal $\Delta\mu$ on both sides of the interface. Since the spin-flip (spin relaxation) rate is proportional to $\Delta\mu_{FM,NM}/r_{FM,NM}$, and $\Delta\mu_{FM}=\Delta\mu_{NM}$ at the interface, the current at the FM side is already largely depolarized before crossing the interface. By contrast, if $r_{NM} \approx r_{FM}$, the current spin polarization is retained in the NM material. This is the case, for example, when the FM/NM interface is formed by metals (e.g. Co/Cu, $NiFe/Al$, etc). Spin polarized current for the two cases mentioned above is illustrated in Fig. 2.5(b).
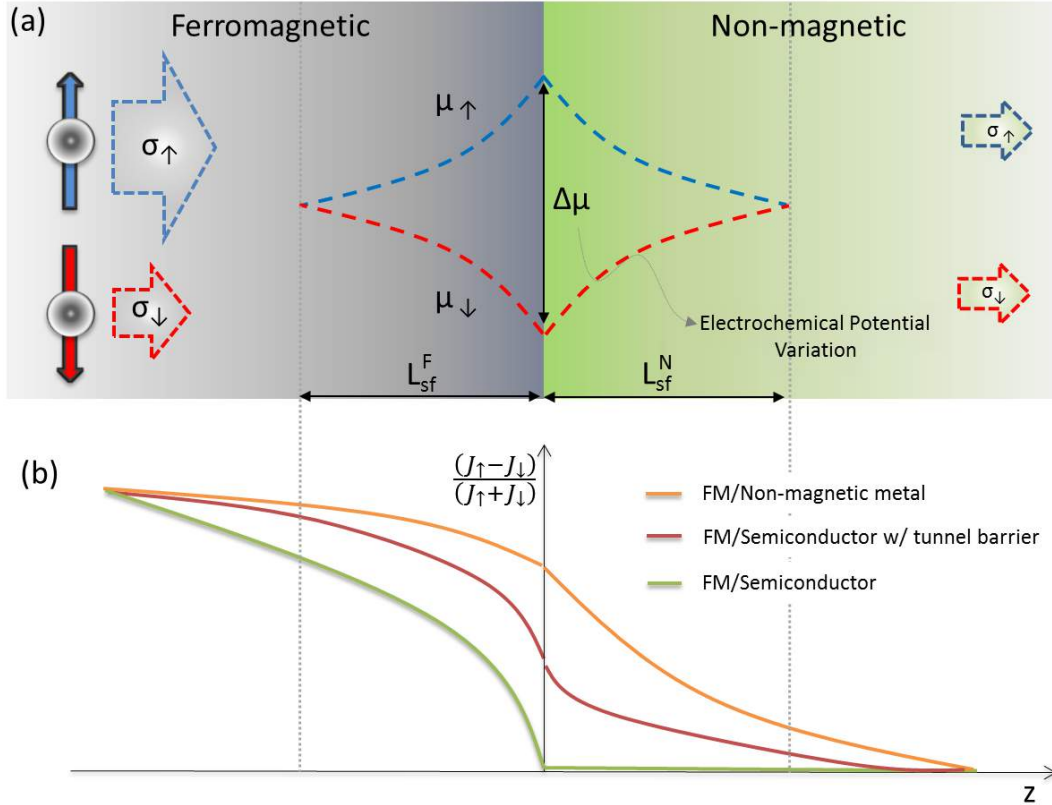
Figure 2.5: Illustration of the spin accumulation and injection from a ferromagnetic metal to a non-magnetic material. (a) Spin-polarized electrons from a ferromagnetic metal (grey) into a non-magnetic material (green) accumulates near the interface of the heterostructure. This accumulation extends by L_{sf}^F into the ferromagnetic metal, and L_{sf}^N into the non-magnetic side. The splitting of the Fermi level at the interface is represented by the variation of the electrochemical potential of both spin species, $\mu_\uparrow$ and $\mu_\downarrow$. The electrochemical potentials in the illustration are continuous through the interface (transparent contacts), but they can be highly discontinuous (e.g. with tunnel barriers).(b) Spin current polarization for three different situations: FM/metal (orange), FM/Semiconductor with tunnel barrier (red), FM/semiconductor (green). The conductivity mismatch between FM metal and semiconductor induces an increase of spin-flip recombination at the FM side, and negligible spin polarized current is injected into the semiconductor. With a tunnel barrier, $\Delta\mu$ is considerable increased at the non-magnetic side, compensating the spin depolarization at the FM side. *Illustration adapted from [49].*

The effect of interface resistances on spin accumulation

Another interesting scenario is when a finite interface resistance r_b is included in the system. Interface resistance can be present both intentionally (e.g. tunnel barriers), or unintentionally (e.g. air oxidation). When r_b is considered in the calculations, the spin polarization of the current density at the interface is described by,[62]

$$\left(\frac{\vec{J}_\uparrow - \vec{J}_\downarrow}{\vec{J}_\uparrow + \vec{J}_\downarrow}\right)^{FM/r_b/NM} = \frac{\beta r_{FM} + \gamma r_b}{r_{FM} + r_{NM} + r_b}, \tag{2.19}$$

where γ is defined as the spin asymmetry coefficient (if any) of the interface layer. As evidenced by Eq. 2.19, even if $r_{NM} \gg r_{FM}$, the spin accumulation at the NM can be recovered when r_b is of the same magnitude of r_{NM} and γ is finite. In fact, insulating tunnel barriers grown from metal oxides provide simultaneously enough interface resistance and spin assymetry. This phenomena, referred to as spin-polarized tunneling effect, is very relevant when one attempts to inject spin polarized carriers into a material of dissimilar conductivity, such as in metal/semiconductors systems (see red curve in Fig. 2.5(b)).

The physical mechanism behind the recovery of spin accumulation lies in the spin-dependent transmittances of electrons through the barrier. The tunneling conductance is proportional to the DOS of each spin-subband at the Fermi level [53]. Hence, a large suppression of the minority spin-carriers can be obtained since the penetration of the wave-function through the barrier is limited (as compared to the majority spin carriers). The presence of a spin-filtering tunneling barrier induces a discontinuity of $\Delta\mu$ at the interface. The spin accumulation at the NM side increases proportionally to γr_b, which balances the spin-flip rate at FM/NM interface, and restores the spin-polarization [61, 62]. In the limit where $r_b \gg r_{NM}$, spin-polarization can be fully recovered and reach values as high as γ. When $r_b \approx r_{NM}$, the recovered spin-polarization amounts to $\gamma/2$.

Successful injection of spin-polarized current density into a NM material does not entail that the spin imbalance can be detected by a second FM electrode. For instance, an energy barrier (normally referred to as Schottky barrier) is normally formed at metal-inorganic semicondutor interfaces. For specific barrier heights and reverse bias, the carrier injection is dominated by field-emission tunneling [63]. Schottky barriers are thus good candidates to assist the injection of spin-polarized currents into semiconductors, since it provides a controllable interface resistance. However, upon forward bias the carrier injection is no longer dominated by tunneling since the barrier is reduced due to FM Fermi level shift. Therefore, in spite of the successful use of Schottky bar-

riers as spin filters [64], the method is not suitable since spin accumulation can not be sensed in the second FM electrode due to the conductivity mismatch [65].

2.3.2 Injection and Detection with spin-polarized tunneling electrodes

Detection of spin-polarized currents in organic systems is generally limited to electrical detection in a spin valve configuration. Direct optical methods can not be applied to detect spins, since organic materials have a very low spin-orbit coupling. Consequently, the most accessible method for the detection of spin accumulation in OSCs is by positioning a second FM electrode in the vicinity of the spin injecting electrode. One can understand the spin accumulation detection (or extraction) process as follows. Consider a second FM electrode contacting the NM material near the spin-injecting FM electrode at distances $d \leq L_{sf}^{NM}$. In this region a spin imbalance is present, i.e. spin-up and spin-down electrochemical potential are not equal. The difference of the spin-dependent electrochemical potentials on both sides of the NM/FM interface generates an effective built-in voltage δV. Since the magnetization of the FM detection probe can be reversed (inversion of minority and majority spins), the excess voltage δV can be switched according to the probe magnetization. Note that if the metal electrode is non-magnetic the voltage built-up is zero, and the spin accumulation can not be detected.

We now focus our attention in the case of FM/r_b/NM/r_b/FM structures, which is decribed by the theory developed by Valet & Fert [59, 62]. The total series resistance of this two-terminal spin-valve structure is given by,

$$R^{P,AP} = 2(1 - \beta^2)\rho_F t_F + \rho_N t_N + 2(1 - \gamma^2)r_b + 2r^{P,AP},$$ (2.20)

wherein labels P and AP indicates the total resistance for each magnetic configuration of the FM electrodes – parallel and anti-parallel, respectively. Values t_F and t_N represents the thickness of the FM and NM electrodes, respectively. The spin-dependent interface resistance contributions $r^{P,AP}$ are respectively defined as

$$r^P = \frac{\frac{(\beta - \gamma)^2}{r^N} \coth\left(\frac{t_N}{2l_{sf}^N}\right) + \frac{\gamma^2}{r^F} \coth\left(\frac{t_F}{2l_{sf}^F}\right) + \frac{\beta^2}{r_b}}{\frac{1}{r^N} \coth\left(\frac{t_N}{2l_{sf}^N}\right) \frac{1}{r^F} \coth\left(\frac{t_F}{2l_{sf}^F}\right) + \frac{1}{r_b}\left[\frac{1}{r^N} \coth\left(\frac{t_N}{2l_{sf}^N}\right) + \frac{1}{r^F} \coth\left(\frac{t_F}{2l_{sf}^F}\right)\right]},$$ (2.21)

and,

$$r^{AP} = \cfrac{\frac{(\beta-\gamma)^2}{r^N}\tanh\left(\frac{t_N}{2l_{sf}^N}\right) + \frac{\gamma^2}{r^F}\coth\left(\frac{t_F}{2l_{sf}^F}\right) + \frac{\beta^2}{r_b}}{\frac{1}{r^N}\tanh\left(\frac{t_N}{2l_{sf}^N}\right)\frac{1}{r^F}\coth\left(\frac{t_F}{2l_{sf}^F}\right) + \frac{1}{r_b}\left[\frac{1}{r^N}\tanh\left(\frac{t_N}{2l_{sf}^N}\right) + \frac{1}{r^F}\coth\left(\frac{t_F}{2l_{sf}^F}\right)\right]}. \qquad (2.22)$$

The magnetoresistance ΔR can then be obtained from Eqs. 2.21 and 2.22, with $2(r^{AP} - r^P)$. To simplify the expression, t_F is taken equals ∞ for the spin-dependent components of the magnetoresistance. This is a plausible assumption since ΔR saturates for values when $t_F > l_{sf}^F$. For instance, in this thesis the ferromagnetic electrodes were generally based on 25nm thick NiFe thin-films, which is considerably higher than $l_{sf}^{NiFe} \approx 5.5$nm. In view of this simplification, the magnetoresistive response for two-terminal spin-valves with spin-polarized tunneling electrodes becomes

$$\Delta R = \cfrac{2(\beta r_F + \gamma r_b)^2}{(r_b + r_F)\cosh\left(\frac{t_N}{l_{sf}^N}\right) + \frac{r_N}{2}\left[1 + \left(\frac{r_b}{r_N}\right)^2\right]\sinh\left(\frac{t_N}{l_{sf}^N}\right)}. \qquad (2.23)$$

This expression is valid for vertically stacked, or laterally patterned spin-valves with FM electrode width equals the NM spacer thin-film thickness. In Figure 2.6 the magnetoresistance $\Delta R/R^P$ is plotted as function of interface resistance normalized with the FM electrodes area – generally referred to as the resistance–area product (RA) in the literature. This example is based on Fig. 03 of Ref. [62] for GaAs as NM spacer, but with input parameters of NiFe/AlOx spin-polarized tunneling electrodes. It becomes evident that injection and detection of spin-polarized transport is possible in systems with large mismatch of conductivity ($r_{NM}/r_{FM} > 10^6$ in this example). However, measurable MR signals are only achieved in a very narrow range of interface resistances. The maximal magnetoresistance for these systems reads,

$$\frac{\Delta R}{R^P} = \frac{\gamma^2}{1 - \gamma^2}, \qquad (2.24)$$

which is only obtained for $t_N \ll L_{sf}^{NM}$. This condition is satisfied in Figure 2.6 only when the NM thickness is <20nm – that is to say, $t_N/L_{sf}^{NM} < 10^{-2}$. It becomes therefore clear from Eq. 2.24 that in order to successfully fabricate a spin-valves based on materials with mismatched conductivities, tunneling barriers with substantial spin asymmetry coefficient and precisely engineered interface resistance must be employed.
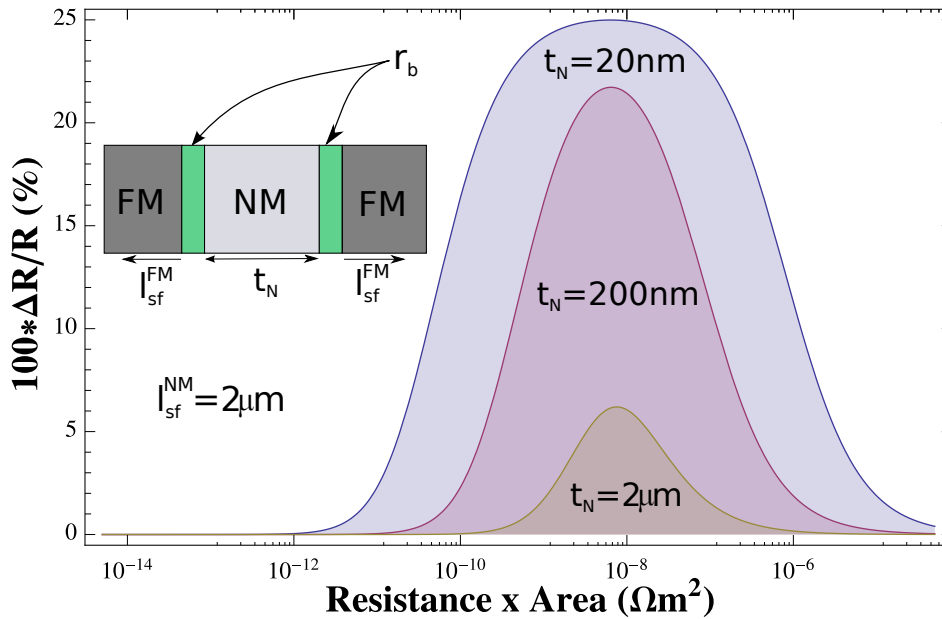
Figure 2.6: The magnetoresistance of an FM/I/NM/I/FM structure with high conductivity mismatch plotted versus interface resistance-area (r_b), wherein FM = NiFe (r_{FM}=0.8x10^{-14} Ωm^2, β=0.7, L_{sf}^{FM}=5.5nm), NM = GaAs (r_{NM}=4x10^{-9} Ωm^2), and the I = AlOx (γ=0.45). The MR is plotted for several electrode spacings t_N, and for a fixed spin diffusion length l_{sf}^{NM}=2μm. Based on Ref. [62], but calculated for NiFe/AlOx electrodes.

2.3.3 Local and Non-local Spin Accumulation

The discussions of the previous sections have focused exclusively on a two-terminal measurement geometry. This is generally referred to as *local measurement*, and is the simplest way to measure spin accumulation. As illustrated in Fig. 2.7, current is sourced and spin accumulation voltage built-up is measured with the same electrodes, $FM2$ and $FM3$. Although this strategy is technically simple and straightforward to measure, a few spurious effects can take place at the junction that can potentially mimic MR effects. For instance, the magnetization reversal of the FM contacts generate stray fields in the NM region, which can induce local Hall voltages across the junction. This can be easily mistaken as a MR effect, but it is not related to the NM's spin accumulation. Another effect that play a role is the intrinsic AMR effect (introduced in Chapter 1) of the interconnects, that is always included in the signal.

An alternative way of detecting pure spin accumulation is to take advantage of the diffusive nature of the electron spin. As illustrated in Fig. 2.7, when charge current is applied through $FM1$ and $FM2$, a voltage build-up can be measured as δV between $FM3$ and $FM4$. Spin accumulation generated at $FM2$ diffuses isotropically through the NM, while the charge is only driven between $FM1$ and $FM2$ when an electrical
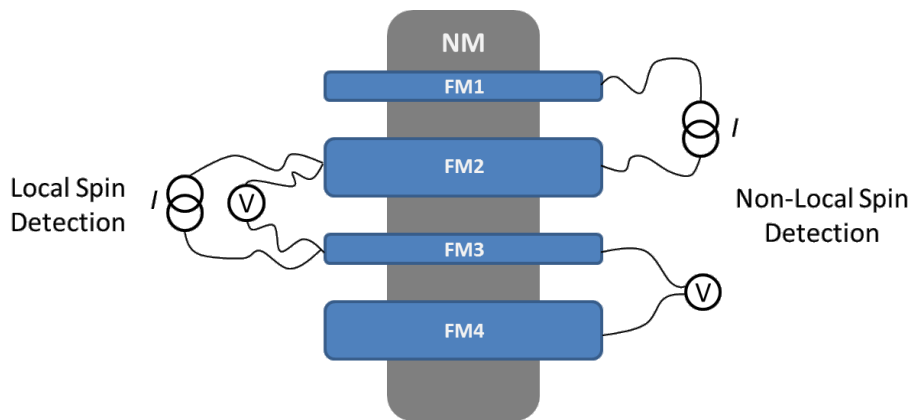
Figure 2.7: Local (*left*) and non-local (*right*) measurement geometries for spin accumulation detection. Local measurements of MR suffers the influence of spurious effects arising from local $\vec{E}$ fields and carrier motion. To avoid spurious effects, a non-local measurement can be employed due to the diffusive nature of the spins. In this case, current flows trough a set of electrodes ($FM1$ and $FM2$), and spin polarization is measured non-locally with neighboring electrodes of different width ($FM3$ and $FM4$). Magnetization direction of the electrodes can be controlled independently by an external magnetic-field due to the magnetic shape anisotropy.

potential is applied. The difference $\delta V_{FM3} - \delta V_{FM4}$ can then be measured by a voltmeter. This measurement method is generally referred to as *non-local measurement*, and is largely used in the metal spintronics community. The method allows to remove unwanted spurious contributions from the MR signal [57, 66]. Non-local measurement is considered to be a definite and unambiguous proof of spin transport in NM materials, and it is still lacking in organic spintronics.

2.3.4 Magnetic Tunnel Junctions

If $t_N{=}0$ we fall in the special case of magnetic tunnel junctions (MTJ), wherein an insulating layer decouples two spin-polarized FM electrodes. Magnetoresistance effects in MTJs were sought after since 1975 [67], but only in 1995[68, 69] sizable MR effects were consistently and reproducibly obtained. Spin-polarized tunneling in FM-I-NM (I - insulator, and NM - non-magnetic) structures were long known to be possible, but several technical difficulties had to be overcome in order to fabricate devices showing significant tunnel magnetoresistance (TMR) effects. Most of the difficulties had originated in the thin-film stack growth and their characterization. However, with the technological advances in the mid nineties, the successful manufacture of MTJs has become routine.
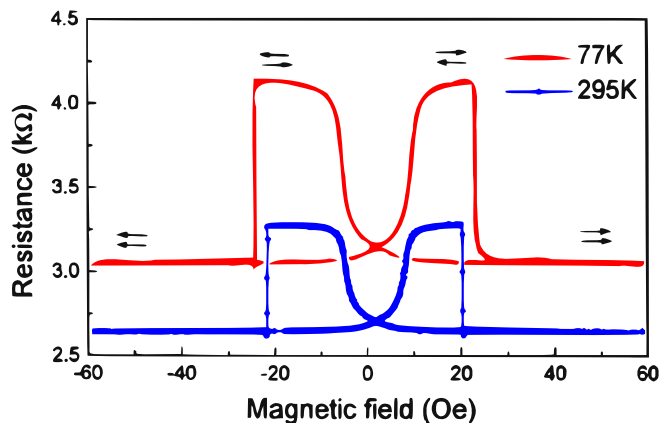
Figure 2.8: Magnetoresistance of an highly optimized Co/AlOx/NiFe tunnel magnetic junction, showing TMR of 27.1% and 20.2%, at 77K and 295K, respectively. Taken from Moodera *et al.*[70]

MTJs are based on the stacking of a FM-I-FM thin-film structure, wherein the insulating layer should be only 1-3nm thick. The response of the device is extremely sensitive to the quality of this tunneling barrier. Interface roughness, purity, homogeneity, and interface contamination has been shown to have drastic deleterious effects to TMR values. The difficulties in finding ideal materials & processes become evident in retrospect. Even 18 years after the seminal works of Moodera et al. (1995, Ref. [68]) and Miyazaki et al. (1995, Ref. [69]), only two materials for tunneling barriers have found widespread application in MTJs – namely, AlOx and MgO. This thesis deals exclusively with AlOx, given its superior mechanical and chemical robustness in comparison to MgO.

The ferromagnetic layers must be also carefully engineered, so that the magnetic reversal of each layer switches independently with well separated coercive fields. In Figure 2.8 a highly optimized Co/AlOx/NiFe MTJ[70] is shown. Well separated switching is clearly observed in these MTJs, which is characterized by a plateau of the resistance with the FM electrodes in anti-parallel configuration ($\rightleftharpoons$). TMR as high as 20% was observed at room-temperature, while these values considerably increase at low-temperatures. Record room-temperature TMR values with AlOx tunnel barriers amount to 70-80%[71, 72] using CoFeB electrodes. This FM alloy shows the highest surface spin polarization from known FM metals at room-temperature (γ=0.51~0.58), justifying the high TMR values.

Since MTJs are strongly dependent on the tunnel barrier quality, the bottom electrode thin-film, which supports the top layers, ultimately defines the device response. Roughness of the bottom electrode may induce dipolar coupling with the top electrode inhibiting independent reversal of their magnetization. In the worst case, ultrathin insulating layers grown over rough surfaces may contain a very high density of hot spots

due to non-homogeneous thickness. This leads to localized high current densities and premature failure of the junction. This issues will be further discussed in Chapter 3, Section 3.4.

2.4 Spin transport in Organic Semiconductors

Direct measurement of electron spin polarization in organic (semi)conductors has been accomplished by very few groups through two-photon photoemission [73], and low-energy muon rotation experiments [74]. Optical methods such as those used in early studies of spin-polarized injection in inorganic semiconductors [75], fail to detect electron spins in organic semiconductors due to their weak spin-orbit interaction. As a result, spin injection, transport and detection investigations in organic spintronics is generally accomplished in actual device platforms.

The length scales in which an electron spin diffuses through non-magnetic materials defines the scales in which devices should be produced, in order to detect measurable magnetoresistace signals. In organic semiconductors (OSC), the record spin diffusion length reported was on the order of $100 - 135$ nm [76, 77]. For that reason, the minimal requirement for a successful spin signal measurement is that the gap t_N separating the ferromagnetic electrodes in a spin-valve should be within in the $t_N \leq l_s$ limit. A common practice to obtaining such small gap sizes is the vertical stacking of FM electrodes sandwiching the charge-transporting layer (hereafter referred to as *vertical devices or vertical geometry*). While this technique has been remarkably successful in metallic spintronics and MTJ fabrication, it leads to critical reliability issues with OSC NM spacers.

Figure 2.9 illustrates a common source of uncertainties in an FM-OSC-FM junction produced in vertical geometry. In the top electrode deposition step, highly energetic atoms landing on an OSC surface diffuse through the OSC matrix, forming unwanted pin-holes and magnetic inclusions. Moreover, OSC solids tend to have rough surfaces due to the high-molecular weight of its molecules. Thus, the interface between the OSC and top electrode has inherently high roughness, which leads to stochastic magnetic behavior of the FM electrodes [78]. Rough interfaces along with metal diffusion is translated into misleading interpretation of results, such as whether charge transport is in tunneling or injection regimes [79], or if the MR signal in these vertical stacks in fact originates from spin tunneling or injection through/into an OSC spacer layer, or from magnetic inclusions prevenient from electrode deposition [80, 81]. The first organic spin-valve reported [82] can be taken as an example of a misled interpretation, in which the

(quasi) temperature-independent I-V characteristics of the LSMO/$Alq_3(> 100$ nm)/Co junction resembles one of a TMR, and not a GMR spin-valve. The space-charge-limited behavior expected for these OLED-like structures is totally absent. Bias-voltage applied in MR measurements were generally much lower than the built-in potential formed in these Schottky-like FM/OSC interfaces, which indicates that virtually no current was actually passing through the OSC. These evidences strongly suggest that pin-holes and/or charge tunneling from FM filaments largely dominates the device response.

FM/OSC interfaces fall in the case where the conductivity mismatch should induce a large current density spin depolarization. Spin relaxation due to the high resistance of OSCs should lead to a significant reduction of the spin accumulation at the interface, which is an essential feature of a spin valve. As for now, no reports have tackled this matter. Controversially, there have been many successful reports on organic spin valves with and without tunnel barriers [80, 83–85]. It should be noted, however, that these reports were predominantly obtained in experiments with vertically stacked trilayer devices, which are generally prone to defects.
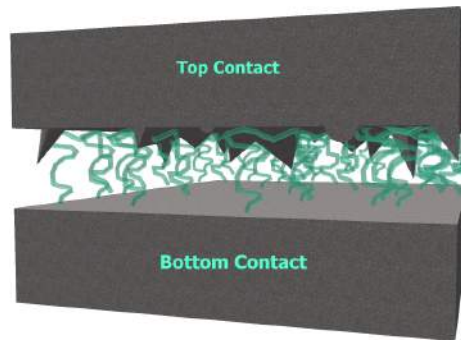
Figure 2.9: Schematic illustration of a conventional organic spin-valve. The device is composed of a vertical stack, in which the OSC is sandwiched between two different FM materials. Metallic FM electrodes deposited on top of organic materials are expected to have rough surfaces, accompanied by stochastic surface magnetic properties. Diffusion of metal also leads to the formation of pinholes and uncontrolled junction gap size.

Low junction resistances, strong conductance dips at zero-bias, and inversion of the MR signal at low-voltages have been reported by various groups [76, 81, 86]. The presence of FM inclusions in Alq_3 as deep as 80 nm has been confirmed by electron energy loss spectroscopy (EELS) in Co/Alq_3 junctions, along with uncorrelated changes of the MR signal with bias [87]. In short, spin transport measurements in vertical devices brought up a multitude of controversial results, and it is evident that different strategies must be devised.

2.4.1 Lateral Spin Valves for Organic Semiconductors

An alternative to the vertical device configuration described in the previous chapter, is the use of laterally patterned spin-valve devices. Pinholes and magnetic inclusions are completely eliminated in this device geometry. It also allows a better definition of the gap size, which is an important parameter largely used to calculate the spin relaxation life-time τ_{sf}, or conversely, the spin diffusion length L_{sf}^{NM}. Moreover, it opens the possibility of having more than two terminals, and exploit the diffusive nature of spin signals[66], as described in Section 2.3.3. Non-local spin and Hanle spin precession measurements are experimental proofs still lacking in organic spintronics. Even a more definite demonstration of GMR effects in two-terminal devices is desired.[86] Another potential of lateral spin valves is the possibility of gating the OSC, which may create a $2D$ electron-gas with high mobility, and potentially result in high MR signals [88].

There have been few reports describing the fabrication of lateral spin valves for OSCs, and so far no unambiguous proof of MR has been given. Dediu *et al.* have provided evidences of spin-polarized electron transfer in α-sexithiophene ($T6$) within a lateral spin valve with LSMO electrodes [89]. However, the LSMO contacts had the same geometry (hence similar switching fields), and all the interconnects were produced with the same material. Therefore, no spin valve-like signal was measured, and the signal could be likely due to AMR of the LSMO interconnects. Huisman *et al.* have also reported on an unsuccessful non-local measurement of spin currents on *Pentacene* with *Co* electrodes. Likewise, no MR signal was recorded in their sole MR measurement [90]. Michelfeit *et al.* presented a concept of a lateral spin valve with $CoFeB$ electrodes and Dihexylquaterthiophene ($DH4T$) as spin/charge transporter layer. However, they also have not reported any MR measurement [91]. Naber *et al.* reported on their attempts to inject spin-currents into rubrune crystals through tunnel barriers [92], which were also not successful.

In this thesis, lateral spin valves based on highly conducting polymer are introduced (Chapter 4). Devices based on conducting polymers drastically differs from previous attempts to manufacture lateral spin valves. Conducting polymers possess intrinsic availability of charge carrier density, without the need to apply an external electric field. Therefore, this class of devices are, to some extent, comparable to all-metallic spintronic devices. It is important to emphasize, however, that conductivities of the best conducting polymers are still over three orders of magnitude lower than metals such as Ag, Cu, etc. Consequently, conducting polymer spin valves may still suffer from the conductivity mismatch problem when spins are injected with FM metallic electrodes.

3 Experimental Methods

This chapter presents the fabrication techniques that were developed for the manufacture of high-quality nanoscale devices. After a brief introduction to the electron-beam lithography technique used, the resist combination used for the fabrication of high aspect-ratio sub-10nm gaps between nanostructures virtually absent of defects, while maintaining excellent edge quality. The protocol is specially useful for designs that suffer from strong proximity effect, allowing fabrication of dense array of nanostructures with spacing down to 60nm. The method developed to obtain very smooth aluminum thin films via simple room-temperature thermal evaporation is also shown. For the smoothest films (root mean square roughness Rq<0.3nm), even the standard grainy Al nanostructure is not appreciable by atomic force microscopy.

3.1 Electron-beam lithography process

In this thesis we were specially interested in probing organic semiconductors at very confined spatial regions. To this end, we employ electron-beam lithography (EBL), since it allows routine creation of nanoscale patterns on a surface[93]. The idea behind this technique is the fabrication of suitable masks on a sample surface, which is used for the transfer of desired patterns. These masks are in general made of electron beam-sensitive polymers (resists), which are *spin-coated* on a substrate and *baked-out* with a hot-plate or an oven. The bake-out step is done in order to remove residual solvent and to densify the material. The bake-out temperature/time drastically influence the properties of resists, and must be optimized for each process. Resists change their properties upon *exposure* to high energy electron radiation. Subsequently, the sample is immersed in an appropriate solvent to dissolve the exposed regions (positive tone resists), or the unexposed regions (negative tone resists). This critical process is referred to as *development* step. Deposition of suitable materials onto the mask, followed by dissolution of the resist in specific solvents (*lift-off*), routinely yields patterns in the sub-50nm scale. A general lithography process work-flow is displayed in Figure 3.1 for a positive-tone resist.

The quality of the substrates on which the structures are fabricated is of paramount importance. The surface roughness, in particular, plays a major role in defining the electrical properties of the devices. For instance, manufacture of tunnel magnetic junctions on rough surfaces leads to the formation of hot-spots in the non-uniform tunnel barrier. This can cause coupling between top and bottom ferromagnetic electrode (FM), not allowing the independent reversal of the electrodes. Moreover, high roughness can preclude the formation of the tunnel barrier, since it can induce shorts between the two FM layers. In the fabrication of organic field effect transistors (OFET), surface roughness is equally important. High performance OFETs are only obtained with very smooth channels. The gate dielectric/OSC interface quality dictates the overall performance of the OFET, and should be kept as smooth as possible in order to obtain transistors with high-mobility.
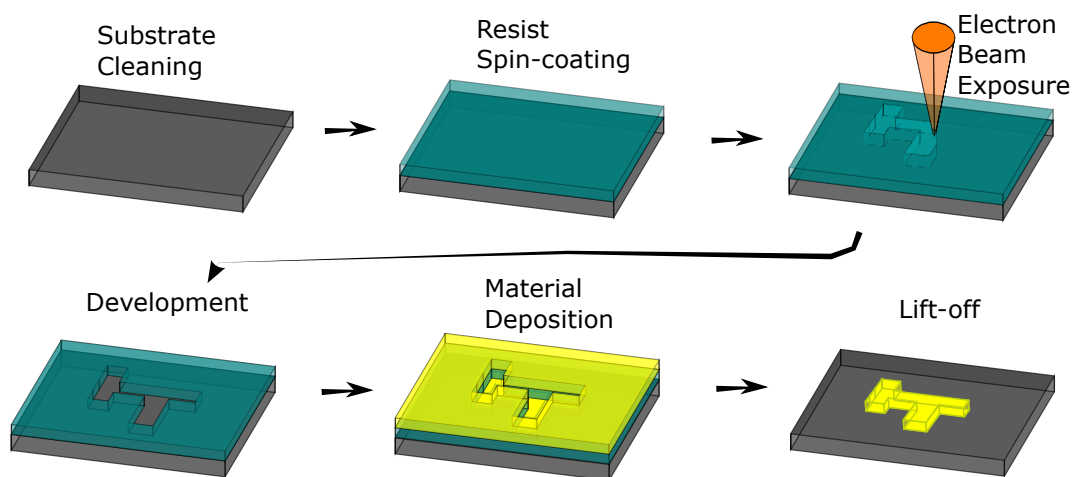

Figure 3.1: **General work-flow of the additive patterning process.** Resist (sacrificial layer) is coated on a clean substrate and is exposed by an electron-beam. The exposed areas are dissolved with an appropriate developer, and material is deposited onto it. The resist is stripped off leaving behind the desired nanostructures.

Heavily As-doped silicon wafers (500μm thick) with thermally grown SiO_2 were used as substrates for all devices presented in this thesis. They were purchased from Silicon Valley Microelectronics, and were inspected by atomic force microscopy (AFM) on a wafer-to-wafer basis. Only wafers with surface root mean square roughness Rq<0.17nm were used for device fabrication. The doped silicon had a low resistivity (ρ=$1 - 5$ mΩcm, and had 150nm coating of highly insulating SiO_2. The underlying conducting Si can be used as an extra electrode for globally gating the chip, or can be left unused in floating potential.

3.2 PMMA-PMGI resist combination: a highly reliable approach for nanostructural patterning

Perhaps the most used resist in EBL is the poly(methyl methacrylate) (PMMA), a high-resolution positive-tone resist with excellent film-forming properties and thermo-mechanical stability.[94, 95] PMMA can be synthesized with very high purity, which allows the fabrication of defect-free masks for pattern transfer with lateral dimensions in the scale of the molecular length of PMMA chains <10nm.[96] Pattern transfer can be done in multiple ways – including wet etching (e.g. SiO_2 etching with hydrofluoric acid), dry etching (mostly reactive ion etching processes), and material deposition. In this thesis, focus is given exclusively to the latter. In particular, material deposition took place via high-vacuum (HV) and ultra-high-vacuum (UHV) physical vapor deposition (PVD).

When electron-exposed structures are in close proximity to each other, the thickness of the resist becomes a very important parameter since high aspect-ratio resist structures can collapse in the development step. Therefore, one generally relies on thin layers (30-50nm) to obtain small nanogaps with PMMA resist. Figure 3.2 displays a false-colored scanning electron microscopy (SEM) image of a typical EBL fabricated nanostructure with PMMA in a two-step lithographic process. For the small rectangle-shaped NiFe nanostructures, 50nm of PMMA ($950K$ $A2$ MicroChem Corp.) was used, whereas the well-spaced Au nanoelectrodes were fabricated with a thicker double-layer PMMA combination. For the latter, a bottom layer of lower molecular weight ($495K$ $A2$ MicroChem Corp.) is used in order to produce a small undercut after development, which is the result of a faster dissolution of the low molecular-weight species. The presence of an undercut is of great importance when materials are deposited onto the resist mask. This allows the penetration of solvent in the lift-off step, therefore facilitating the removal of the material and resulting in structures with good edge quality. On the
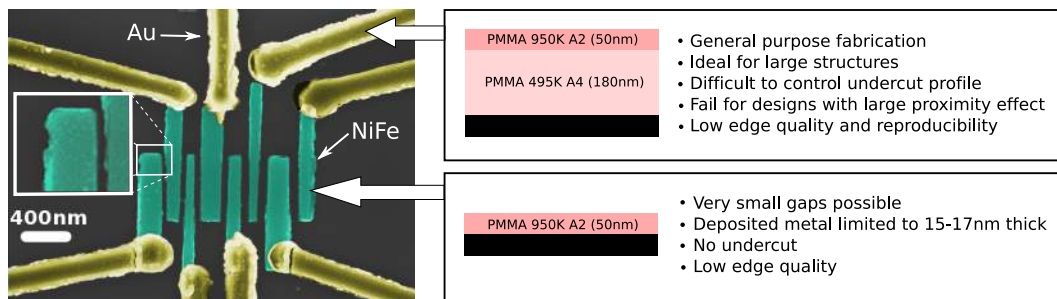

Figure 3.2: Typical nanostructures fabricated with single and double-layer PMMA resist.

other hand, structures produced with a single-layer resists generally have poor edge quality as a result of the material deposition at the resist step edge. This commonly observed issue is highlighted in the inset of the SEM image in Figure 3.2. Moreover, the thickness of material deposited onto thin single layer resists is limited to <1/3 of the resist thickness. As a consequence, the smaller the nanogap targeted in the design, the thinner the material that can be deposited. This is a very critical restriction for electronic devices, since metallic thin film resistance rapid increases with the thickness of the electrodes that can extend several millimeters on the chip.
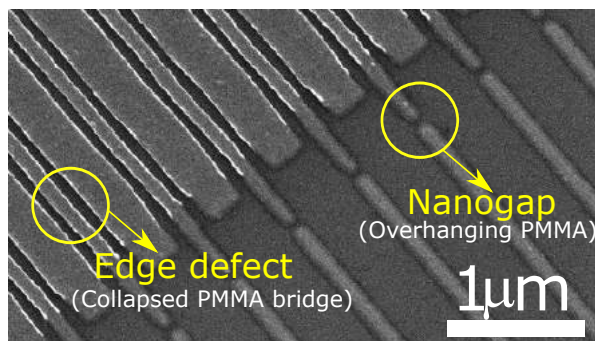

Figure 3.3: **The proximity effect of nanostructures fabricated with PMGI/PMMA bridges.** An SEM image showing NiFe structures patterned with collapsed, and overhanging PMMA resist. The bright stripes indicate the tall NiFe edges, which is normally as tall as the resist used.

Here, a process to fabricate nanostructures that are absent of edge defects, and maintain its quality even for interstructure spacing down to <10nm is presented. Moreover, it allows deposition of thicker film (25-60nm), which drastically reduces the device series resistance. Thicker layers additionally allow the fabrication of the nanoscale junctions and interconnects in one single lithographic step, improving the throughput of devices manufactured. A defect-free nanostructure edge is of particular importance in our devices, since defective edges hinder the formation of continuous multi-layered structures and also adds a great amount of uncertainty in the devices response. The method relies on a double-layer resist technique, in which polymers of different chemistry are used – namely, PMMA as *imaging* top-layer resist, and Polymethylglutarimide (PMGI) as the bottom-layer, *lift-off* and support resist. The combination of these two resists has been previously reported in the literature [97, 98], whereas here we extend the method for structures with high proximity effect.

The advantage of using PMGI-based resist is that its development can be made independently of the imaging resist PMMA, therefore allowing a better control of the undercut profile. Since the PMGI developer is based on an aqueous solution of tetramethylam-
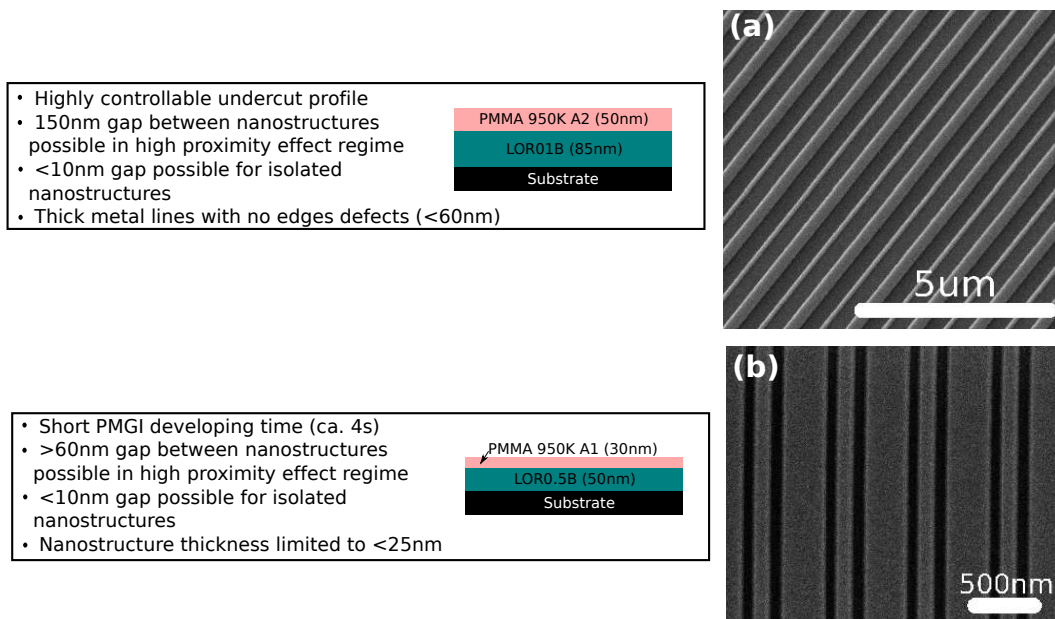
- Highly controllable undercut profile
- 150nm gap between nanostructures possible in high proximity effect regime
- <10nm gap possible for isolated nanostructures
- Thick metal lines with no edges defects (<60nm)

PMMA 950K A2 (50nm)
LOR01B (85nm)
Substrate

(a)

5um

- Short PMGI developing time (ca. 4s)
- >60nm gap between nanostructures possible in high proximity effect regime
- <10nm gap possible for isolated nanostructures
- Nanostructure thickness limited to <25nm

PMMA 950K A1 (30nm)
LOR0.5B (50nm)
Substrate

(b)

500nm

Figure 3.4: The two approaches to obtain extended nanostructures with high-proximity, and minimal spacing >150nm (top), and >60nm (bottom).

monium hydroxide (TMAH), the PMMA is not affected by the second development step. In this scenario, overdeveloped lift-off resist results in clean PMMA bridges overhanging from PMMA/PMGI support. Therefore the formed integrated shadow-mask can be used to form very small nanogaps between the structures. Indeed, metallic junctions with 3nm gaps (tunneling regime) has been recently demonstrated with a PMMA/PMGI-based process.[99] This idea works well for short PMMA bridges, since the long ones can collapse onto the substrate. This is shown in Figure 3.3, for NiFe structures fabricated with overdeveloped PMGI resist. For extended structures in close proximity, PMMA collapses and therefore the rough edges are visible (bright areas). For more isolated structures, the PMMA bridge remains overhanging and a nanogap is formed after metal lift-off.

We have devised two resist preparation protocols, which are shown in Figure 3.4. The first (Figure 3.4(a)), is suitable for long nanostructures with high-proximity effect and spacing >160nm. And the second (Figure 3.4(b)), in which resist thicknesses were reduced, is suitable for manufacture of structures with spacing >60nm. The PMGI dissolution rate is reduced for thinner layers, since the flux of material removed from the undercut region is reduced. For both resist types the same preparation parameters were used – namely, 15min on a hot-plate at 493K for PMGI, and 15min at 453K for the PMMA.

Another important aspect of the process developed is that we can control the edge slope profile by simple sample rotation in the deposition process. This characteristic applies
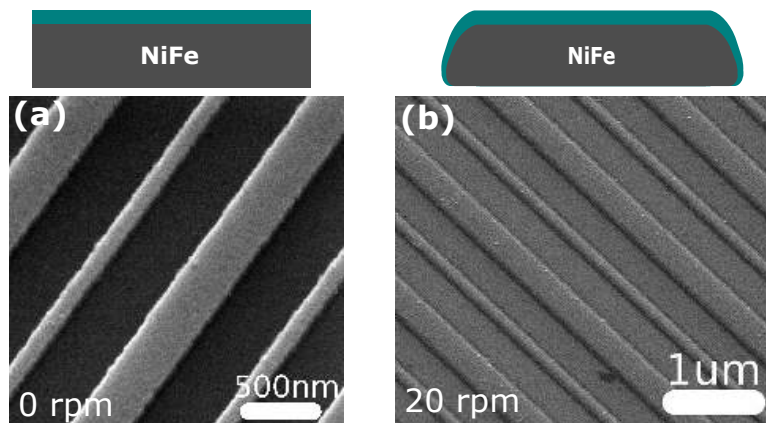
Figure 3.5: **The effect of sample rotation on the edge profile.** Due to the high undercut quality of PMGI/PMMA resists, controlling edge slope is possible by sample rotation in the evaporation process. SEM images for samples processed with no rotation (a), and with 20rpm (b).

for directional evaporation processes, such as thermal and electron-beam evaporation. The SEM images in Figure 3.5 display this effect – when sample rotation (20rpm) is used for the electron-beam (EB) evaporation of NiFe, a sloped edge is clearly observed. In contrast, if no rotation is employed, sharp squared edges are formed. Having this degree of control is of paramount importance for the fabrication of multilayered nanostructures. This is specially important when thin layers must be deposited over the nanostructure. As illustrated in Figure 3.5, sloped edges obtained upon rotation allow complete coverage of the bottom structure, whereas sharp edges hinder the top-layer from covering the whole surface. In our application in specific, we are interested in producing ultra-thin (0.5-2nm) tunneling barriers on top of transition metal electrodes. Any discontinuity of this barrier may lead to catastrophic device failure, for example, when a conducting material is deposited on top of this structure. The bottom and top electrodes become electrically shorted, rendering the device nonfunctional.

3.3 Facile evaporation of smooth Aluminum thin-films

Structured and extended aluminum (Al) thin-film films are an integral part of complementary metal-oxide-semiconductor (CMOS) technology, and also holds promise for applications ranging from plasmonics[100] to spintronics[101]. In this thesis ultrathin and/or ultrasmooth aluminum films were used in the fabrication of thin tunneling barriers (see Section 3.4) and patterned gate electrodes, respectively. In this section we describe the latter, namely, on how to obtain smooth aluminum thin films on a surface.

Aluminum thin films can be obtained from different physical vapor deposition (PVD)

routes – thermal evaporation with heating filaments, electron-beam evaporation, or sputtering. A common feature of all processes is that the resulting thin film has a very rough surface. In Figure 3.6(a), a topographical atomic force microscopy (AFM) image of a thermally evaporated Al thin film is shown. The texture is characterized by sharp protrusions and depressions on the surface, which is the result of its strong tendency to crystallize upon film growth. This has serious implications when the dimensions of the structures of interest are reduced to the scale of the Al grain sizes (50~250nm). As seen in Figure 3.6(b,c), when the width of the structures are reduced to ~80nm, the long stripe is basically compose of a chain of grains. Electrical conductivity through these scaled nanostructures are expected to be strongly dependent on the scattering at these grain boundaries.
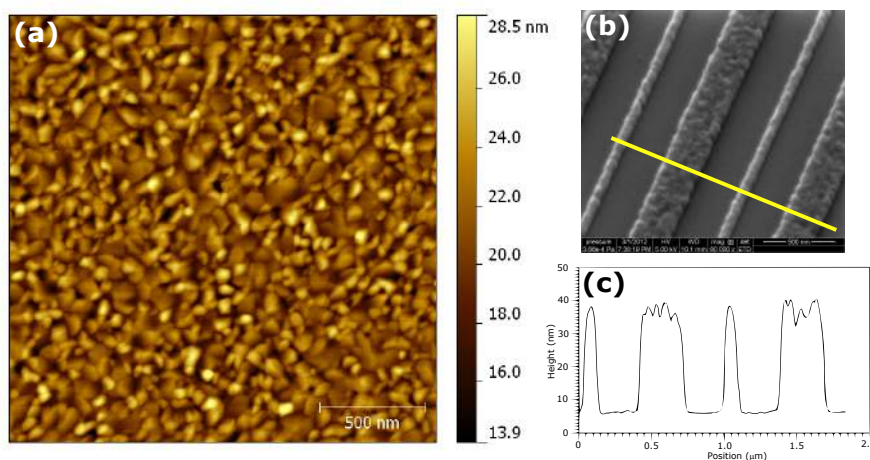

Figure 3.6: **The topography of thermally evaporated aluminum.** An atomic force microscopy (a), and a SEM image (b) of extended and structure Al thin-film, respectively. In (c), the height profile of the Al nanostructure in (b).

One important feature of the Al films exploited here is the fact that when Al films are expose to air, a thin passivating AlOx layer (1~2nm depending on the exposure time) is formed at the surface. Moreover, AlOx is a highly insulating material (band-gap ~8.8eV), whereas Al is a metal with one of the highest conductivities ($3.5 \times 10^7 Sm^{-1}$). Therefore, given the abundance of this material (the third on earth's crust) and its straightforward processing, Al becomes a potential candidate for the fabrication of structured gate electrodes with embedded dielectric gate oxide. In fact, AlOx possesses over two times higher permittivity then standard SiO_2 providing a stronger capacitive coupling and lower leakage currents in MOSFET devices. However, the surface roughness (protrusions and depressions) hinder effective use of Al/AlOx as gate electrodes. In fact, high performing transistors should have ultrasmooth gate dielectric surfaces.

The two most common routes to decrease the surface roughness of Al films are: deposition with the sample kept at cryogenic temperatures, and evaporating Al with high deposition rates. Both approaches rely on the idea of inhibiting Al grain growth. At low temperatures, surface diffusivity of Al on SiO_2 surface is much reduced. Therefore, Al atoms arriving at the substrate have lower chance of diffusing to existing grain nucleation sites. This induces the formation of a much higher concentration of nucleation sites, leading to a film with finer grains and consequent smoother surface. This is an elegant solution, but it is also time consuming and requires specialized equipment.
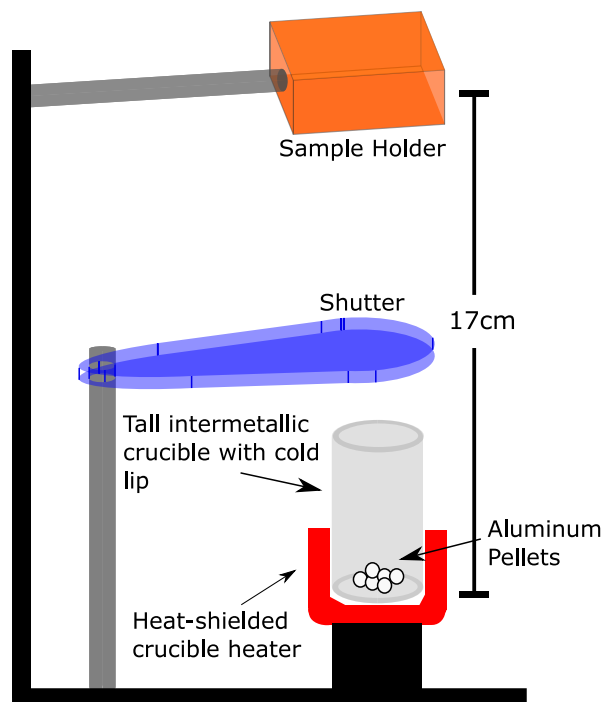

Figure 3.7: **Scheme of the thermal evaporation set-up.** The samples are held in relative close proximity to the Al source in order to achieve high evaporation rates without excessive power settings.

An alternative technique is to grow the thin-films with fast deposition rates, keeping the sample near room-temperature. At fast rates one can keep the substrate temperature low given the short exposure time to blackbody radiation from the hot crucible. Moreover, surface atomic diffusivity, which is higher than bulk self-diffusion, is strongly suppressed by the rate at which new atomic layers are deposited. Quenching Al atomic species (from gas phase) on a relatively cool substrate therefore leads to smoother surfaces by suppressing Al grain growth. In order to obtain high evaporation rates we have modified our evaporation system (Kurt J. Lesker PVD 75) sample holder configuration. This was done in order to align the samples co-linearly with the crucible (K. J. Lesker, EVC5INTSPL02) and crucible heater (K. J. Lesker, EVCH12), and also to reduce the

substrate-source distance. As illustrated in Figure 3.7, small quantities of aluminum and a tall crucible (32mm) were used. This was important since the crucible heater is operated with high power settings (set point 47∼48%, 400-420A) and the molten Al tended to drip off the crucible, catastrophically damaging the heating plates. With these settings and the sample in close proximity (16∼17cm), evaporation rates in the range of 9∼22nms^{-1} have been obtained.
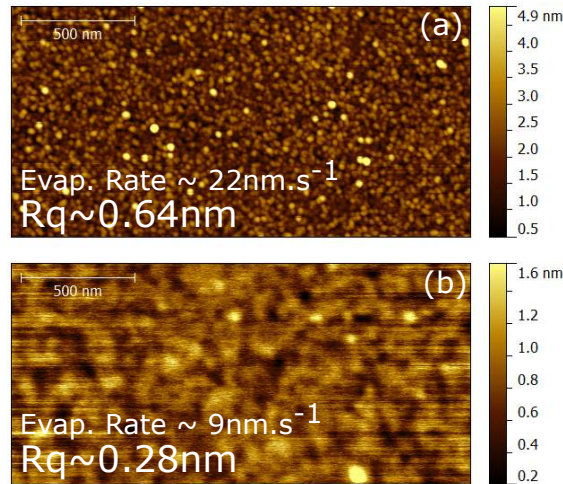

Figure 3.8: **The topography of Al thin-films deposited with high evaporation rates.** As indicated, the r.m.s. roughness R$_q$ of films evaporated at excessively high rates (*top*), where considerably higher than for the optimized evaporation rates (*bottom*) due to substrate overheating.

In Figure 3.8 AFM topographical images for the two evaporation rates are shown. For very fast evaporation rates (∼22nms^{-1}) we have obtained a fine-grained surface texture with Rq=0.64±0.06nm (for ∼1s deposition time, 23nm thick), whereas for relatively slower evaporation rates (∼9nms^{-1}, for ∼2s, 21nm thick) the grainy texture disappears (Rq=0.28±0.02nm). Root mean square roughness measurements were averaged from three randomly chosen 2x2μm^2 areas on the sample. For thick films deposited at faster rates (∼20nms^{-1}, ca. 200nm), the surface roughness drastically increases to Rq=8±1nm (not shown). These results suggest the existence of a narrow processing window, which is defined by an interplay between deposition rate and sample temperature. We observed a very rapid increase of substrate temperature when the evaporation rate was too high, or when the exposure time was too long. High substrate temperatures may promote higher surface diffusivity and grain recrystallization processes, which lead to higher roughnesses. Therefore, by optimizing evaporation power settings and evaporation time, very smooth Al thin-films (Rq<0.3nm) were obtained. The importance of smooth surfaces will become clear in Chapter 5, in which Al gate electrodes are used in the manufacture of low-operating voltage organic field-effect transistors.

3.4 Spin-polarized Electrodes with AlOx Tunneling Barriers

Now we move our attention to the growth of ultra-thin Al films, which are useful for the fabrication of spin-polarized tunneling electrodes. In order to manufacture spin injection and detection nanoelectrodes it is important to understand what are the critical parameters influencing its quality. To do so, it is imperative and instructive to review a few aspects of magnetic tunnel junction (MTJs) fabrication. As already discussed in Section 2.3.4, the most crucial step of MTJ fabrication is the insulating layer growth, the layer decoupling the top and bottom FM electrodes. This barrier should allow the conservation of the spin in the carrier tunneling process (i.e. spin-polarized tunneling). This requirement alone indicates that the easily obtainable native oxides of ferromagnetic metals (e.g. NiO, CoO, Fe_2O_3) should be avoided. These oxides act as strong spin scattering centers, mixing spin-up and spin-down tunneling carriers. For this reason, early MTJs based on Ni-NiO-Co[102] has showed measurable TMR effects only at liquid Helium temperatures (4.2K). At room temperature, the strong paramagnetic centers of the NiO tunneling barrier effective mixes the spin polarization of the tunneling electrons, whereas at low temperature the spin scattering is less effective due to magnetic moment ordering.

Growing continuous ultra-thin (0.5-3nm) insulating oxides on a metal surface over large areas is highly challenging. The most straightforward route to grow these barriers is the direct evaporation of insulating oxides. However, this route generally leads to non-continuous barriers, with high concentration of pin-holes. Vapor-deposited oxides have low-surface diffusivity on metal surfaces, hindering the formation of smooth and continuous layers. The strategy found to be most effective is the deposition of a metal, followed by its oxidation. This methodology has proven to be highly successful for aluminum (Al). The surface diffusivity and wetting of Al on FM metal surfaces is excellent in comparison to its oxides. Since the first Al atomic layers deposited, a continuous film is formed, which can be later oxidized. In fact, even films as thin as 0.4nm (two Al monolayers) have been demonstrated to lead to high TMR values (∼10%) [103].

Another important aspect of producing high quality AlOx tunneling barriers is the method employed to oxidize the Al film. Several methods exist – such as natural air oxidation, in-situ oxidation with pure O_2 (with or without UV light), and plasma assisted oxidation (DC or RF). The most successful method for the oxidation of Al so far has been the latter, which is employed in this work. Plasma oxidation is a very efficient
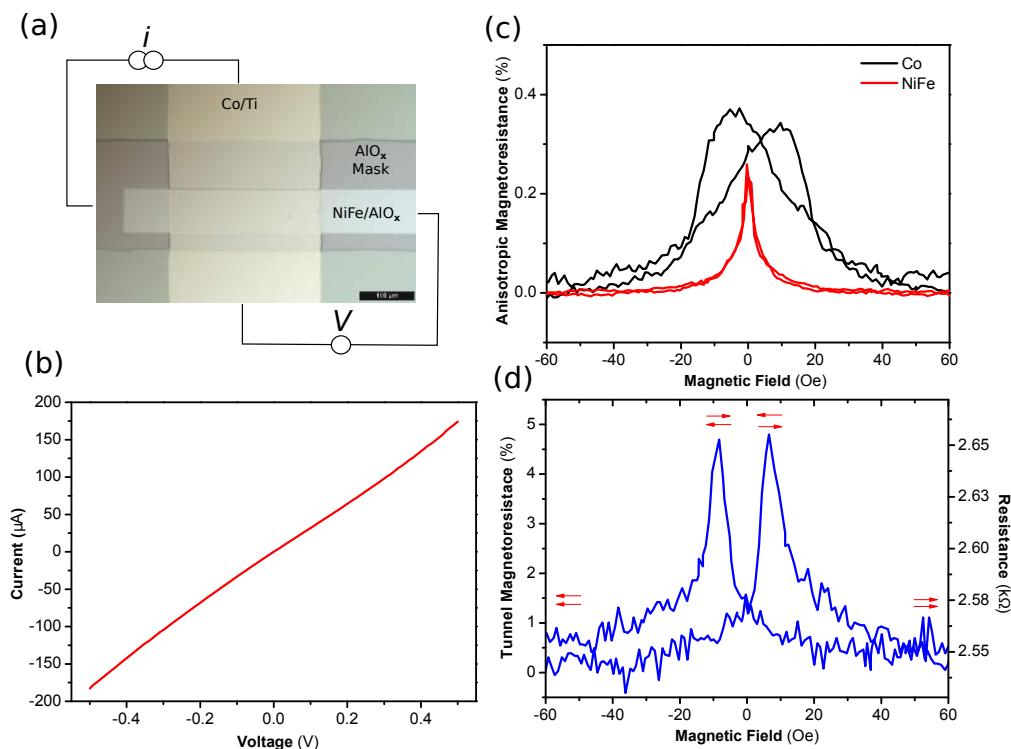
Figure 3.9: **NiFe/AlOx electrode test structure.** (a) An optical micrograph of the MTJ. Top and bottom FM electrode stacks form electrical contact in a junction defined by an dielectric layer, as indicated. (b) Non-linear tunneling-like current-voltage curve. (c) Anisotropic Magnetoresistance of the FM electrodes, showing the different coercive fields. (d) Tunneling Magnetoresistance of the NiFe/AlOx/Co MTJ. Measurement performed with a four-point probe layout at 295K and 8mV bias.

and convenient method since it allows deep O_2 penetration and stoichiometry control at room-temperature. For our lateral spin-valves the method is specially important, since the O_2 plasma additionally removes organic contamination prevenient from lithography and ambient exposure. It is therefore important to demonstrate that after the device processing, spin-polarized tunneling is conserved.

To verify the most critical features of the PEDOT:PSS nanoscale lateral devices, we have produced large-area MTJs that mimic the process history of the spin-polarized nanoelectrodes arrays presented in Chapter 4. One exemplary MTJ is shown in Figure 3.9(a), which consists of a NiFe(25nm)/AlOx bottom electrode, a thick insulating AlOx (40nm) mask defining the junction area, and the top Co (20nm) electrode with a layer of Ti (3nm) for protection against air oxidation (a TiO_x passivation layer is formed upon exposure to air). The thin-film stack of the bottom electrode is grown with identical procedure to the one used in our nanoscale lateral devices. This also entails exposing the spin injecting surfaces to air, a negative resist (ma-N2400 from

Micro Resist Technology), and solvents (n-methyl-2-pyrrolidone, acetone, isopropanol, and acidic water) in order to fabricate the dielectric mask and deposit the conducting polymer. For these devices, the ultra-thin Al is plasma oxidized twice – after removing from the evaporation chamber (to generate high quality barrier), and a short plasma cleaning step to remove residual hydrocarbons from the surface before top electrode evaporation.

Post-process oxygen plasma cleaning has been previously shown to be highly effective to recover TMR values on air/solvent-exposed MTJs.[92, 104] In the example of Figure 3.9, a further test is performed. The clean bottom NiFe/AlOx electrodes are shortly exposed to a PEDOT:PSS solution (at pH 4), and rinsed thoroughly with water and ultrasonic bath. This is followed by thermal annealing of the electrode for 30min (at 423K and 0.1mbar), before proceeding to the evaporation of the the top Co/Ti electrode. This step is initially used to remove water residues from the PEDOT:PSS (highly hygroscopic), but has also the crucial function of removing water molecules from the AlOx surface.

Current-voltage (IV) measurement on MTJs is the first routine test made in order to verify if the junction has a non-linear tunneling-like behavior, like the one shown in Figure 3.9(b). When tunnel barriers are produced from very thin Al films (<1nm) it is not uncommon to have several shorted junctions. Specially when the junction area is very large, as the one prepared for this example. It is important to note, however, that electrical shorts are not as critical for organic-based lateral devices. OSC small molecules or polymers are very bulky, and therefore do not diffuse through underlying low-quality tunnel barriers. In the following, it is also important to check the magnetization reversal with the application of an external magnetic field. The easiest and most direct measurement to probe the reversal is to evaluate the anisotropic magnetoresistance (AMR) of the materials. As seen in Figure 3.9(c), a clear modulation of resistance is observed for Co and NiFe with magnetic field. The NiFe strap possesses low coercive field H_C ($\sim$1-2Oe), whereas Co is a harder magnet, with coercivity $\sim$20-25Oe at room-temperature.

Figure 3.9(d) shows a representative tunnel magnetoresistance (TMR) curve obtained with the MTJ described above. Large TMR values of $\sim$5% are routinely obtained at room-temperature after lithography and exposure to PEDOT:PSS solution. This value may seem low in comparison to record TMR values, but a few features of this junction must be evaluated. Firstly, we do not obtain a fully antiparallel magnetization state of the junction. This can be seen from the magnetotransport measurement as a peak-shaped curve when electrodes are in antiparallel state. No resistance plateau is

achieved in the antiparallel state, as the one observed in fully optimized MTJs (Figure 2.8). This is an interesting feature since it clearly indicates that the TMR is much higher than what is measured. To obtain junctions at a full antiparallel state with materials with relatively close H_C, the FM electrodes are generally grown under special conditions. One important design rule to obtained well-spaced H_C is to have very thin FM films in order to reduce out-of-plane reversal and possible interlayer coupling. Another common approach is to use a seed layer (e.g. Ta, Si) for the bottom FM electrode growth to obtain textured crystallography and allow sharper magnetization reversal. Yet, another trick to obtain sharper reversal is to grow the FM electrode under magnetic field, promoting an preferentially magnetization axis. These optimizations have been intentionally not employed since in this thesis well spaced coercive fields are obtained by tuning the shape anisotropy, instead of crystallographic anisotropy of the nanoelectrodes.

3.5 Nanoscale Lateral Spin Valves Fabrication Details

In the following, details of the manufacture of the organic lateral spin valves are presented. These devices will be further explored in Chapter 4. The devices were prepared on square-shaped (10x10mm^2) Si substrates, that were cut with an automated diamond wire wafer dicer. All substrates were cleaned by sonication in acetone and isopropanol for several minutes, thoroughly rinsed in deionized water, and exposed to oxygen plasma for 20min (Diener PICO Plasma System, O$_2$ 10sccm, 1mbar, 100W). The devices were fabricated in two lithographic steps with a RAITH150-TWO electron beam lithography system. In the first step, a combination of LOR01B lift-off resist (ca. 85nm thick, baked out for 15min at 493K) with PMMA950K-A2 imaging resist (ca. 50nm thick, baked out for 10min at 453K) was used. Resist thickness was measured using a mechanical profilometer (Veeco Dektak 150). Electron-beam exposed areas were developed in two steps – first in MIBK:IPA (1:3) to remove exposed PMMA, followed by ma-D525 to remove the PMGI-based resist (immersion for 8s with mild agitation at 295K). A short O$_2$ plasma treatment (<3s) was routinely used to ensure a surface free of resist residues prior to metal deposition. Permalloy is electron-beam evaporated with high deposition rates to guarantee a smooth surface (CreaTec Fischer & Co. GmbH, ca. 1Ås^{-1}, base pressure <4x10^{-9}mbar, sample holder temperature 310K). Subsequently, aluminum is thermally evaporated from a Knudsen effusion cell (ca. 0.8Ås^{-1}, base pressure <2x10^{-8}mbar, thicknesses varying from 0.5nm to 2nm). To avoid contamination of the aluminum with magnetic impurities, the second evaporation step is performed 2h after permalloy evaporation. The deposition process is monitored

with a calibrated quartz crystal microbalance (QCM). Thin-film thickness calibration was performed frequently using X-Ray Reflectivity (XRR) in an X'Pert Panalytical system for all materials used. After metal evaporation the devices were transferred to a parallel-plate plasma sytem, after a brief exposure to air. Aluminum is exposed to O_2 plasma for $\sim$10s to oxidize the tunneling barrier ($11mW/cm^2$, $6.6x10^{-2}$mbar, 70sccm O_2, base pressure $<1x10^{-5}$mbar, Oxford PlasmaLab 80 Plus RIE System). Metal lift-off is carried out in hot (373K) N-Methyl-2-pyrrolidone (NMP), followed by thorough rinsing with fresh NMP and isopropanol. Short sonication was routinely used to assist the cleaning process.
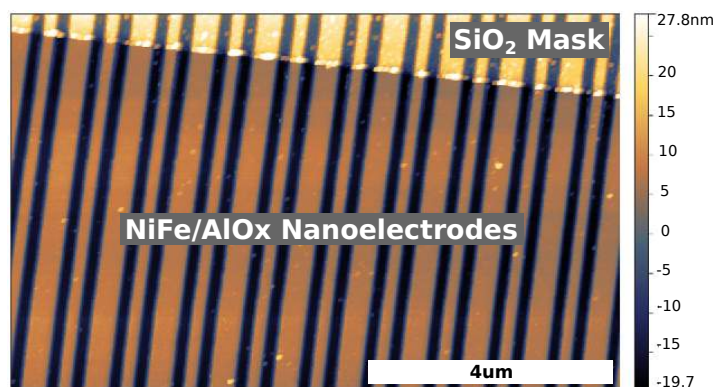

Figure 3.10: **Typical two-terminal organic lateral spin valve.** The atomic force microscopy image shows the topography of the interdigitated NiFe(25nm)/AlOx(2nm) nanoelectrode, and the insulating dielectric (SiO$_2$) that defines the area where spin-coated PEDOT:PSS makes contact with the electrodes.

For the devices with gaps below 200nm, a modified process was devised, wherein resist thicknesses of both PMMA and PMGI resists were reduced to 50nm and 30nm, respectively. This allowed for the fabrication of highly dense interdigitated nanoelectrode arrays of high quality and reproducibility. An integrated dielectric mask is produced in the second lithographic step. Negative-tone imaging resist ma-N2401 combined with LOR01B lift-off resist is exposed to electron beam only at the spin-valve junction and at the contact pads. The resist is developed using ma-D525 developer, thoroughly rinsed, followed by the deposition of SiO$_2$ by RF sputtering (4Wave Inc. System, base pressure 10^{-9}mbar, 40nm thick). Lift-off is performed in NMP, followed by thorough rinsing with fresh NMP and isopropanol. The AFM image of Figure 3.10 shows the device state after the lift-off and drying process. It is clear that residues left over from lithography process remains on the surface. Therefore, a short O_2 plasma treatment is performed to remove these residues (ca. 5s, 5W, $6.6x10^{-2}$mbar, 70sccm O_2) and guarantee a clean interface between the nanoelectrodes and the modified PEDOT:PSS.

3.6 Organic Semiconductor Processing

PEDOT:PSS thin-films

PEDOT:PSS dispersions are commercialized in a range of weight ratios and concentrations. In this thesis the Clevios PH 1000 is used, a state-of-the-art PEDOT:PSS grade, which shows the highest conductivities available commercially. This dispersion has an 1:2.5 PEDOT-to-PSS weight ratio, and can reach conductivities of 1000 Scm^{-1} after appropriate treatment. The excess PSS necessary to obtain high-doping unfortunately leads to dispersions with high acidity (pH $\sim$1.7), which complicates the integration of PEDOT:PSS material with several materials. Therefore, the acidity of PEDOT:PSS solution was carefully controlled with an organic base, allowing integration of this material with less stable materials, such as Ni, AlOx, etc. In the following, the method used to process and integrate PEDOT:PSS with lateral spin-valves is presented.

Three layers of freshly prepared PEDOT:PSS solution are spin-coated on top of the device (120s at 3000rpm, ca. 200nm total thickness), and a moist cotton swab was used to remove excess PEDOT:PSS and expose contact pads. PEDOT:PSS thickness was calibrated with a mechanical profilometer. Solvent was allowed to evaporate for 5min on a hotplate at 350K (in air). The chip is then transferred to a vacuum oven inside a glove-box ($<0.1ppm$ O_2 and $<0.1ppm$ H_2O), where a second baking step is performed to remove residual solvent (30min at 420K, 1mbar). The acidity of the PEDOT:PSS solution was controlled following the procedure reported in Moet *et al.*[105] by systematically adding an aqueous solution of of DMAE:H_2O (1:8).[1] Solution pH was measured with a calibrated Orion micro pH electrode (Thermo Scientific, Inc.). To enhance the conductivity of the spin-coated PEDOT:PSS films, 5%$_{vol}$ of DMSO was added to solution and mixed at room-temperature for 1h to homogenize the solution completely. We routinely prepared fresh solutions for each device batch, ultrasonicated and filtered it directly before the spin-coating process (0.45μmMilliPore Corp. syringe filters).

pBTTT Thin-Films

pBTTT thin-film can be prepared from solution processing techniques like spin-coating, ink-jet printing, or drop-casting. The material can be dissolved in warm organic solvents such as, 1,2-dichlorobenzene, tetralin, and so on. Solvent polarity improves solubility, and therefore 1,2-dichlorobenzene is generally the solvent of choice. With this solvent, it

---

[1]Diaonized Water was produced with a Millipore Gradient A10 (18.2 MΩcm, <5 ppb organic matter).

is important to dissolve the pBTTT at high temperatures (340-355K), whereas processing can be performed at temperatures as low as 333K. Films processed at this temperature after being fully dissolved result in continuous films with high-quality. Difficulties in obtaining continuous films arise when processing the films on highly hydrophobic surfaces. Combining non-interacting surfaces with hot (355K) pBTTT solutions give rise to dewetting at the spin-coating process (black regions in Fig. 1.4). However, if the film is processed at 333-338K, and the solution is left for a few seconds over the sample surface before spin-coating, obtaining continuous films is again possible.

3.7 Characterization Techniques

Scanning Electron Microscopy (SEM, FEI Quanta 250 FEG) and Atomic Force Microscopy (AFM, Agilent Technologies 5500) were routinely employed to verify device quality. Unless otherwise stated, AFM images were recorded in tapping mode with general purpose Si tips (Mikromasch NSC14/Al BS or Nanosensors PPP-NCHR). Room temperature electrical measurements were performed under vacuum in a magnetic-field-equipped variable-temperature probe-station (LakeShore Cryotronics, Inc.). Devices were transferred from the glove-box environment in a sealed container to avoid moisture up-take, and only opened in a stream of N_2 in the probe-station chamber. Devices were left in vacuum ($<3x10^{-4}$mbar) for 2h (up to 12h) before each measurement. Temperature-dependent electrical measurements were performed in a Physical Property Measurement System (PPMS, Quantum Design Inc.) equipped with liquid-He cryostat in the temperature range 2K-350K, and magnetic fields up to 20kOe. Static contact-angle measurements were performed with a G10 Krüss system.

The magnetic reversal of the spin-valve nanoelectrodes were routinely checked with optical wide-field polarization microscope optimized for Magneto-Optical Kerr Effect (MOKE) sensing. The microscope, provided by Evico Magnetics GmbH, is equipped with an electromagnet that allows the application of a magnetic field of up to 500mT along an arbitrary direction in the sample plane and with a CCD camera that is capable of taking magnetic-contrast images of the sample surface. The local hysteresis loop can be recorded by selecting an arbitrary region in the field of view, allowing quick testing on actual devices.

Devices measured in the PPMS system have been baked out for 2h at 400K ($\sim$10mbars) before measurements to evaporate moisture adsorbed in the transfer process. Current-Voltage (I-V), Current-Magnetic Field (I-H), and Resistance-Temperature (R-T) data were recorded with different semiconductor parameter analyzers controlled by Lab-

View programs (National Instruments Corp.). Most room-temperature I-H measurements were performed with Keithley 4200-SCS, whereas temperature-dependent and low-temperature measurements (<80K) were performed with a current source (Keithley 6220) and a nanovoltmeter (Keithley 2182A). In order to reduce resistance measurement uncertainty we routinely performed a sequential measurement method, subtracting the recorded voltage at zero and the required current.[106] The result was averaged over several measurements, normally around 16-64 times. This allowed to compensate for thermoelectric offset currents, reduce the effect of capacitive couplings, and reduce the noise level.

4 Charge and Spin Transport in PEDOT:PSS Nanoscale Lateral Devices

In this Chapter, the electrical transport of the highly conductive poly-(3,4-ethylene-dioxythiophene):poly(styrenesulfonic acid) (PEDOT:PSS) is investigated with ohmic and spin-polarized tunnel contacts at nanoscale lateral dimensions. Temperature-dependent charge transport measurements reveals that electrical conductivity scales non-linearly as a function of electrode spacing, which is attributed to the localization of carriers induced by the disorder introduced by the PSS polyelectrolyte. In addition, we demonstrate the integration of this conducting polymer in nanoscale lateral spin valve devices by increasing the pH of the PEDOT:PSS solution. We present charge and magnetotransport measurement results of $NiFe/AlO_x/PEDOT:PSS/AlO_x/NiFe$ lateral structures for various thicknesses of the alumina tunnel barriers. We discuss the absence of magnetoresistance of our spin valves within the framework of Valet-Fert theory, and estimate an upper limit for the spin lifetime of carriers in PEDOT:PSS to $\tau_{sf} \leq 50ns$.

4.1 Introduction

Organic spintronics is a branch of electronics concerned with exploiting both the charge and the spin of the electron in organic semiconductors (OSC). The prospect of using the carrier's spin in OSC has led to a number of device concepts, such as organic magnetic sensors[107], spin-valves[82], and spin-polarized organic light emitting diodes (OLED)[108]. OSCs are very attractive for spintronics applications for several reasons. Firstly, their very small spin-orbit interaction, caused by the low atomic number (Z) of the elements composing semiconducting molecules, leads to very long spin lifetimes for this class of materials.[109, 110] Secondly, ample flexibility in the design of functional molecules makes them perfectly tunable to each specific device design. A typical organic spintronics device consists of two ferromagnetic (FM) electrodes separated by an

organic semiconductor spacer. Substantial modulation of the device resistance is expected upon changing the relative alignment of the magnetization of the ferromagnetic electrodes. Indeed, very large magnetoresistance (MR>300% [111]) has been observed for devices with ultra-thin organic layers, wherein the transport mechanism is dominated by direct tunneling[79, 112], or by multi-step tunneling through localized states or defects[113–115]. These large MR values are strong evidence of the conservation of the spin information in the period it travels through the organic spacer.

Until now, organic spintronic devices are predominantly designed as vertical structures. Although widely used, this geometry is prone to artifacts caused by the top electrode metal penetration[77, 87, 116] radiation damage in the organic layer[117] or other fabrication issues. These problems cause controversy in the interpretation of the electronic transport data, and make peremptory the search for new device geometry. The logical step in the design of more reliable experimental conditions is the fabrication of lateral spin valves for organic semiconductors, in which the electrodes are laid-out coplanarly instead of being vertically stacked. This approach is particularly attractive since it offers ample control over device parameters (e.g. channel length, electrode width, interfacial roughness), thereby greatly increasing experimental flexibility and the range of materials that can be studied.[92] However, satisfying optimal design procedures for the fabrication of high quality lateral devices is not an easy undertaking[118] and, as a result, only a limited number of experiments have been reported following this approach.[89, 91, 92, 119, 120] Here we report on the fabrication and characterization of lateral spin valves for a doped organic semiconductor, namely poly(3,4-ethylenedioxythiophene) stabilized with poly(4-styrenesulphonic acid) (PEDOT:PSS). This composite can be dispersed in water due to the hydrophilicity of the PSS polyelectrolyte, and it can be processed into smooth thin films by spin coating. Benchmark conductivity values in excess of 1000 Scm^{-1} can be obtained due to the PSS doping combined with appropriate solvent treatments[121, 122]. The dopant produces a strong π-orbital overlap and consequent delocalization of the carrier wavefunction at the Fermi energy (ε_F), retaining ohmic transport characteristics over a wide temperature range at weak to moderate electric fields.

Previous attempts to obtain spin-polarized charge transport in lateral spin valve devices have largely focused on pristine organic semiconductors, which possess a narrow density of states at energy levels that are usually offset from the ferromagnetic electrode work function. In contrast, highly-doped organic semiconductors such as PEDOT:PSS have a high density of states accessible for transport with high work-function ferromagnetic electrodes. Consequently, devices can be operated at very low voltages without the application of any electrostatic gate. Moreover, the inherent bulk conductivity is

fundamentally important for the design of multi-terminal organic spintronic devices, which may potentially allow non-local measurements of spin currents.[120]

Here we present details on the lateral electrical transport characteristics of spin-coated PEDOT:PSS at scales that are relevant to spin transport in organic semiconductors (<500nm) with bottom nanoelectrodes made of Au, and $Ni_{80}Fe_{20}$ (NiFe, permalloy) coated with a thin alumina tunnel barrier (AlO_x). Measurements with Au electrodes showed a rapid increase in the conductivity of PEDOT:PSS upon reduction of the distance between the electrodes, which reveals the effect of insulating PSS barriers for lateral electrical transport. Magnetotransport data in the samples with ferromagnetic NiFe electrodes allow us to estimate an upper limit for the carriers' spin lifetime of PEDOT:PSS to $\tau_{sf} \leq 50ns$.

4.2 Device Design and Fabrication

The devices were designed in order to minimize any damage to the delicate PEDOT:PSS in the fabrication process. Accordingly, PEDOT:PSS integration with the NiFe/AlO$_x$ and Au nanoelectrodes has taken place only at the last fabrication step, avoiding in this way any interaction of the conducting polymer with organic solvents and/or high-energy radiation. In Figure 4.1(a) a photograph of a typical device is shown, in which one can see the Si/SiO$_2$ substrate (grey), and the contact pads (yellow) covered with a square-shaped dielectric maskof SiO$_2$ that defines the area in which the spin-coated PEDOT:PSS (green) makes electrical contact with the electrodes. In Figure 4.1(b) a scanning electron micrograph of one of the spin-valve device junctions (*type 1*) is shown. The device comprises two-terminal interdigitated nanoelectrodes (green) of 80nm (FM^1) and 280nm (FM^2) in width. The nanoelectrodes were obtained with well-defined geometry and channel lengths ranging from 690nm down to 80nm. An atomic force microscopy (AFM) cross-section profile of a typical structure is overlaid in the illustration of Figure 4.1(c) (light red), demonstrating the edge quality of the nanoelectrodes. The integrated dielectric mask (blue in Figure 4.1(b)) was patterned using a negative resist, creating an opening (window) that allowed electrical contact of the spin-coated PEDOT:PSS with the electrodes. The opening area was selected such that the total interface area between the electrodes and the PEDOT:PSS summed up to $\sim 150\mu m^2$ and $\sim 300\mu m^2$ for the electrodes with small and large widths, respectively. Relatively large junction areas were chosen due to the heterogeneity of the PEDOT:PSS blend. This guaranteed the comparability amongst different devices in the chip and to obtain larger current values.
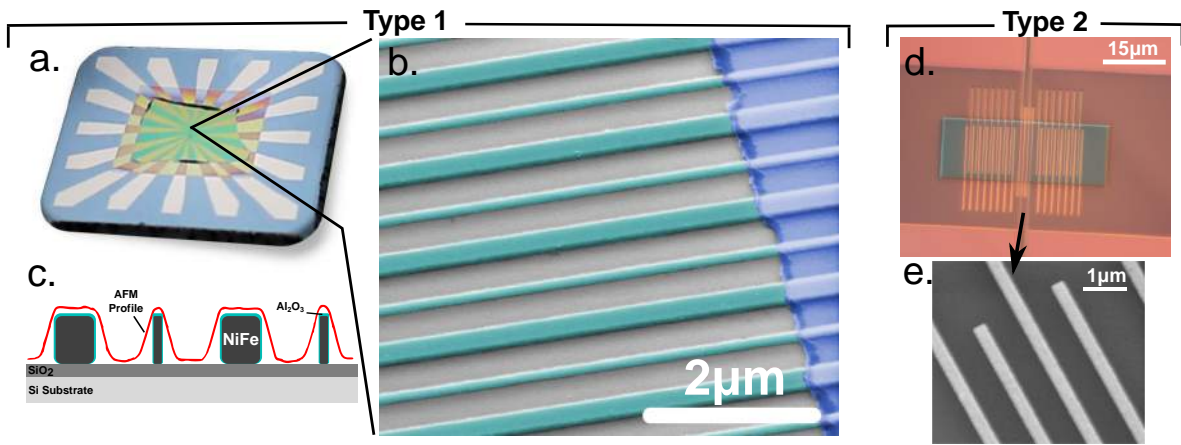
Figure 4.1: Lateral spin valves (*Type 1*) and four-point probe (*Type 2*) devices. (a) Exemplary digital photography of the fabricated devices – the electrodes, the integrated dielectric mask, and the PEDOT:PSS are clearly visible. (b) False-color scanning electron micrograph (SEM) of a typical two-terminal interdigitated spin valve. Each $NiFe/AlO_x$ nanoelectrode (light green) possesses different width for independent control of the terminal's magnetization. The integrated SiO_2 mask (light blue) defines the area where PEDOT:PSS makes contact with the ferromagnetic electrodes. (c) Schematic representation of the device's cross-section. The $NiFe(25nm)/AlO_x(0.5$-$2nm)$ are 80nm (FM^1) and 280nm (FM^2) wide. An AFM cross-sectional profile is overlaid (light red) in the schematics, demonstrating the edge quality of the nanoelectrodes. An optical microscopy image of a typical four point-probe devices (Type 2) with integrated SiO_2 mask is shown in (d). In (e), the corresponding SEM image shows junctions with Ti/Au electrodes separated by 700nm.

Four-point probe devices (*type 2,* Figure 4.1(d)) for conductivity measurements were fabricated in similar manner – namely, bottom electrodes (Ti 1nm/Au 25nm) with an opening defined by a patterned SiO_2 dielectric mask. The PEDOT:PSS was then deposited via spin-coating (200nm thick). In each chip, devices with various electrode separations (300nm, 700nm, and $5\mu m$) were laid out, in order to study the effect of channel length in PEDOT:PSS electrical transport. In Figure 4.1(e) an SEM micrograph of a device with 700nm electrode separation is shown (without dielectric mask). Further technical details of the manufacture of both device types are given in Chapter3 Section 3.5 and 3.6.

For the spin-valve devices (*type 1*), alumina tunnel barrier (light green in the illustration of Figure 4.1(c)) was grown on top of the NiFe electrodes with thicknesses ranging from 0.5nm to 2nm (nominal values) for a number of reasons. Firstly, fabrication of lateral spin valves with air-exposed ferromagnetic metal electrodes would lead to the formation of a variety of antiferromagnetic transition metal oxides at the
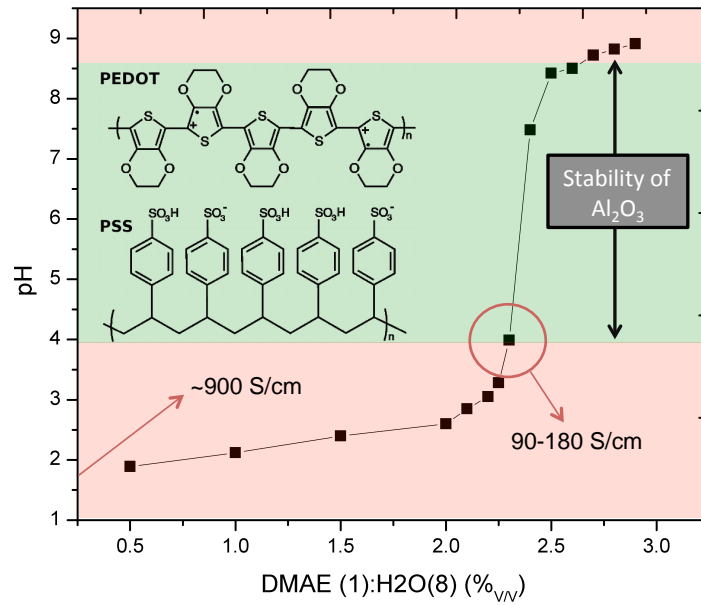
Figure 4.2: Titration of PEDOT:PSS PH1000 with aqueous dimethylaminoethanol. The pH range where the AlO$_x$ tunnel barrier is chemically stable is marked in light green. The chemical structures of PEDOT and PSS are depicted in the inset. A small decrease in conductivity was observed upon DMAE addition at pH4, as indicated in the graph. Conductivity measurements were performed after addition of DMSO (conductivity enhancer), in four-point probe geometry (Au electrodes).

surface, which randomize the spin state of the electrons. Secondly, even though we employ an organic spacer of relatively high conductivity, there is still a "conductivity mismatch"[60] between the NiFe electrode and PEDOT:PSS of the order of ~10^3. The passivating AlO$_x$ layer helps to recover the spin accumulation at the AlO$_x$/PEDOT:PSS interface. Thirdly, the alumina tunnel barrier provides sufficient chemical stability to the electrodes against the dissolving effect of the acidic PEDOT:PSS aqueous solutions (pH1.8 in its pristine state). For instance, dissolution of the NiFe electrodes has been observed upon immersion in warm (50°C) dilute poly(sulfonate styrene) aqueous solutions even for pH5 (not shown). In contrast, AlO$_x$ is chemically stable in aqueous solutions ranging from pH4 to pH8.5.[123]

For all devices the PEDOT:PSS solution has been increased to pH4 by systematically adding the organic base 2-(dimethylamino)ethanol (DMAE). As indicated in the PEDOT:PSS titration curve in Figure 4.2, the addition of 2.3%$_{v/v}$ of dilute aqueous solution of DMAE (1:8 dilution) reduces the acidity of the PEDOT:PSS to pH4. The measured conductivities of the modified PEDOT:PSS processed with DMSO (5%$_{v/v}$) have reduced slightly – from ~800Scm^{-1} in its pristine state to ~120Scm^{-1} after DMAE addition. Thin films of NiFe(25nm)/AlO$_x$(1nm) were immersed in hot solutions (60°C)
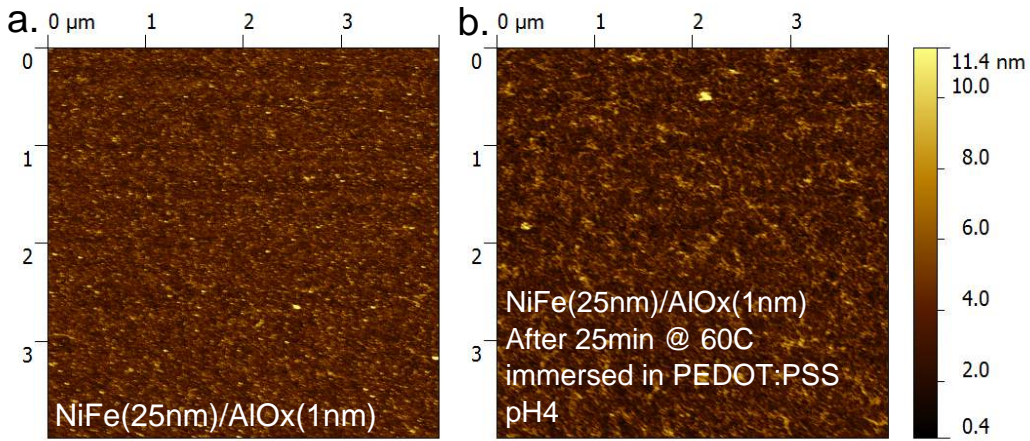
Figure 4.3: Stability of NiFe/AlO$_x$ thin films in hot PEDOT:PSS solutions at pH4. *a.* Atomic Force Microscopy image of NiFe(25nm)/AlO$_x$(1nm) thin film deposited of Si(n++)/SiO$_2$. The roughness for the pristine film was R_q~0.98nm. *b.* Atomic Force Microscopy image for the same film immersed in hot solutions (333K) of modified PEDOT:PSS (*p*H4) for 25min. The measured roughness of the treated film was R_q~0.96nm. The morphological changes after treatment may be attributed to adsorbed polymer molecules, since no thorough cleaning has been made after immersion in PEDOT:PSS. The surface roughness values obtained are much higher than the *device-grade* films/nanostructures roughness (R_q<0.5nm) due to the lower quality substrates used (*test-grade* silicon wafer with *rms* roughness R_q>0.6nm).

of modified PEDOT:PSS (*p*H4) for 25min in order to verify its chemical stability. No damage has been detected, as observed by optical microscopy and by AFM (Figure 4.3). Note that we consider in our work only devices with smooth NiFe/AlO$_x$ electrode surfaces, having root-mean-square roughnesses R_q<0.5nm.

4.3 Scaling effect of PEDOT:PSS conductivity

The conductivity of spin-coated PEDOT:PSS has been widely studied for various device geometries – lateral four-terminal,[124] and vertical two-terminal devices[125] –, and with different formulations – varying the *p*H,[126] solvent[127] or additives[128]. Temperature-dependent charge transport measurements of this disordered three-dimensional electronic system have demonstrated that transport occurs mainly through hopping of charge carriers. Scanning electron microscopy and scanning tunneling microscopy measurements have shown that the morphology of spin-coated PEDOT:PSS is composed of pancake-shaped PEDOT-rich clusters with sizes of the order of 50nm, surrounded
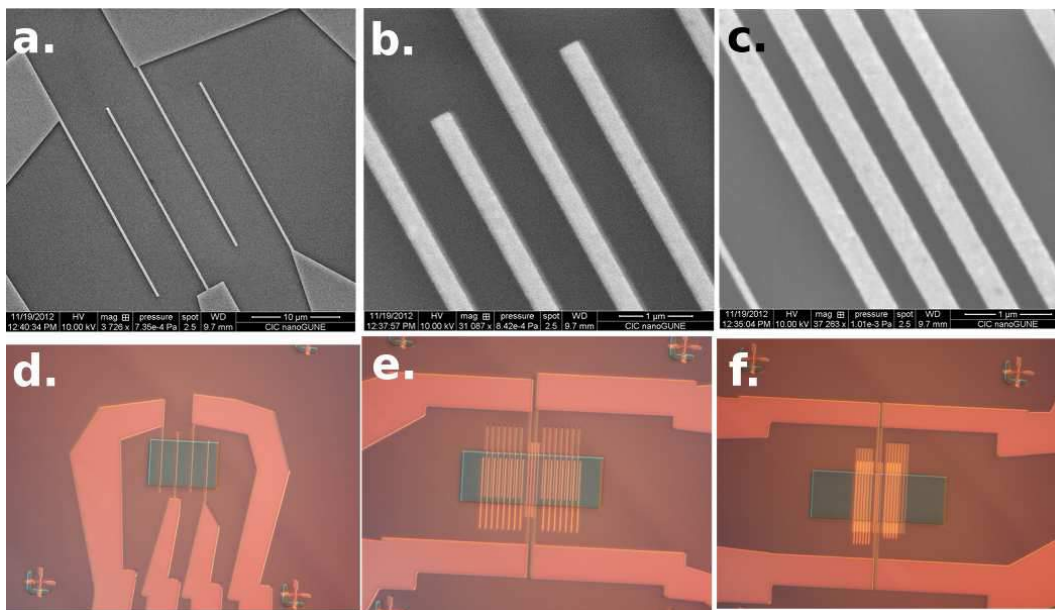
Figure 4.4: Four-point probes for lateral charge transport measurements of *Au/PEDOT:PSS/Au* type devices. a, b, c. Scanning electron micrographs of Au electrodes patterned by electron beam lithography for channel lengths of 5μm, 700nm, and 300nm, respectively. d, e, f. Optical Microscopy images (x1000) of devices with integrated SiO_2 mask. This insulating mask defines the area in which spin-coated PEDOT:PSS make contact with Au nanoelectrodes (images size $100x120\mu$m^2). For junctions (b, e) and (c, f) extra isolated Au nanostructures have been placed near the active electrodes. This was found to improve electrodes' edge quality in the lift-off process.

by PSS-rich lamellae.[129, 130] Recent AFM studies have shown that the PEDOT-rich regions have filamentary morphology for the PEDOT:PSS grade used here (Clevios PH1000).[131] Transmission electron microscopy (TEM) studies have shown that the filaments can extend over hundreds of nanometers.[132] Sub-micrometer vertical charge transport has been shown to differ dramatically from millimeter-sized lateral transport in spin-coated PEDOT:PSS.[133] The effect was assigned to the higher concentration of PSS insulating barriers in the carriers' path in the vertical direction. Of particular relevance to our study is the understanding of the sub-micrometer lateral charge transport of spin-coated PEDOT:PSS, which is still lacking. To address this question, four-point probe temperature-dependent charge transport measurements were performed on devices fabricated with Au nanoelectrodes separated by 300nm, 700nm, and $5\mu m$ (Figure 4.4).

Temperature-dependent, sub-micrometer lateral charge transport measurements of the modified PEDOT:PSS are shown in Figure 4.5. The results were interpreted in the framework of Mott's variable-range hopping (VRH) for disordered electronic systems.[134]

The conductivity was found to follow a stretched exponential temperature dependence over the temperature range 300K-10K, and is expressed as:

$$\sigma\left(T\right) \propto \exp\left[-\left(\frac{T_0}{T}\right)^x\right], \tag{4.1}$$

wherein T_0 is the material-dependent characteristic temperature, and $x=(1+D)^{-1}$ is the hopping exponent related to the dimensionality D of the system. The characteristic parameters of the system can be precisely determined by plotting the reduced activation energy $W(T)=-d(\ln\rho)/d(\ln T)$ against temperature T, where ρ is the material's resistivity (Figure 4.4(c)). The hopping exponents x can be determined from the slope of a linear fit in the log-log plot of W(T), whereas T_0 can be obtained with[135, 136]

$$T_0 = \left(-\frac{10^A}{x}\right)^{-\frac{1}{x}}, \tag{4.2}$$

where A is the intercept of the curve with the log(W(T)) axis. In the analysis we find T_0=1119K (L=5μm), 1231K (L=700nm), and 1260K (L=300nm) for the slopes (x$\approx$0.43) depicted in Figure 4.4(c). This demonstrates that our modified PEDOT:PSS treated with high-boiling point solvent is in the quasi one-dimensional Mott-VRH regime (D$\approx$1).
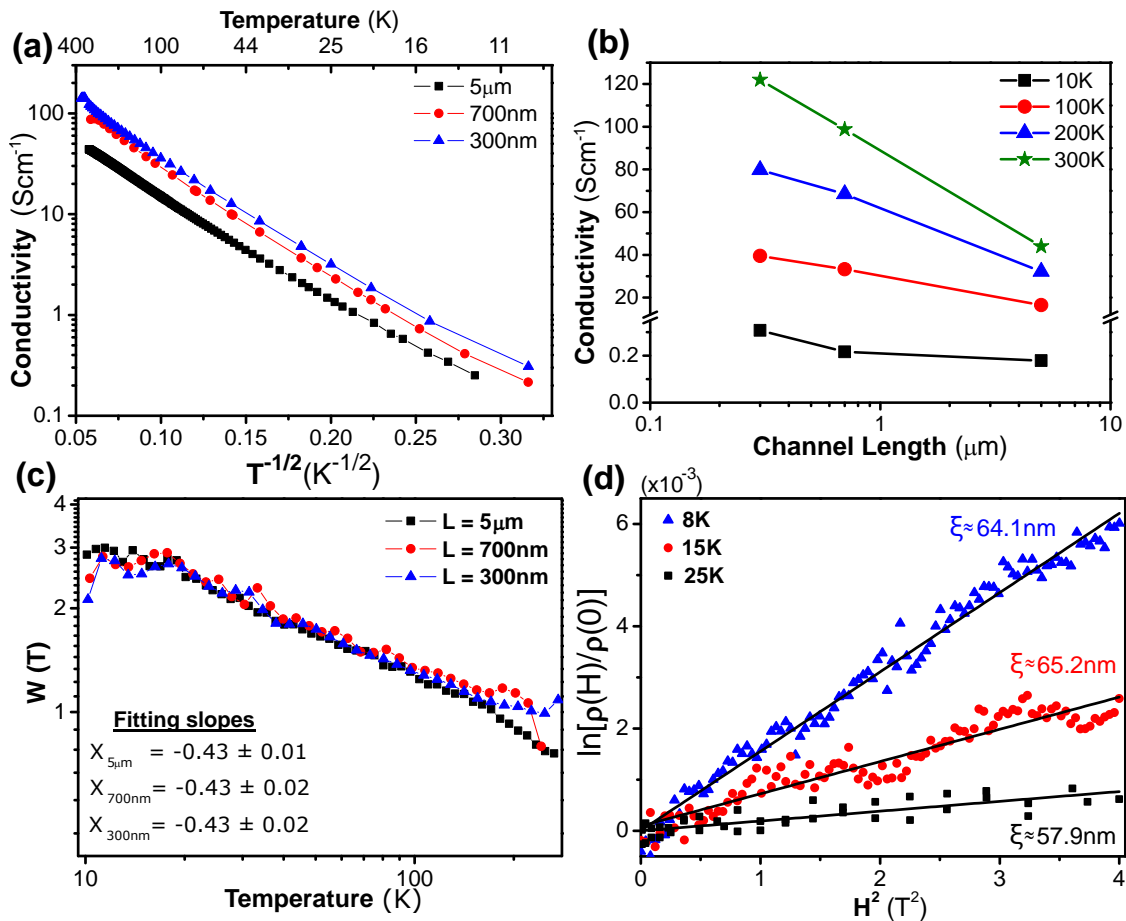
Figure 4.5: Temperature dependence of conductivity for Au/PEDOT:PSS/Au junctions. (a) Distinct increase in conductivity is observed upon reduction of the distance between electrodes for temperatures from 300K to 10K. Four-point probe conductivity measurements were performed for electrode spacings of 5μm (black squares), 700nm (red circles), and 300nm (blue triangles). (b) Conductivity variation with electrode spacing for different temperatures (10K in black, 100K in red, 200K in blue, and 300K in green). The scaling effect is more pronounced at elevated temperatures. (c) Reduced activation energy versus temperature in log-log scale for different L. The linear fitting slopes are depicted within as inset. Fittings were removed for clarity. (d) Magnetoresistance $\ln[\rho(H)/\rho(0)]$ versus H^2 for junction with L=5μm, for T=8, 15, 25K.

Within the framework of the one-dimensional VRH theory, the characteristic temperature T_0 is related to the density of states of the PEDOT:PSS at the Fermi level $N(\varepsilon_F)$, and to the localization length ξ of the electron's wavefunction via the equation $T_0 = 4/N(\varepsilon_F)\xi k_B$.[134, 137] The localization length ξ in one-dimensional hopping electronic systems can be estimated from the dependence of resistivity with weak magnetic

fields (H) with the expression

$$\ln\left[\frac{\rho(H,T)}{\rho(0,T)}\right] = t\left(\frac{\xi}{L_H}\right)^4\left(\frac{T_0}{T}\right)^{\frac{3}{2}}, \tag{4.3}$$

where t=1/288 is a numerical constant [138], and $L_H = \sqrt{c\hbar/eH}$ is the magnetic length. The VRH theory predicts a positive magneoresistance having quadratic response, as observed in our devices. In Figure 4.5(d) the magnetoresistance curves for the junction with L=5μm at different temperatures are shown. The localization length is evaluated with Eq. (4.3), and is estimated to be ξ=62±4nm, as indicated in Figure 4.4(d). Localization lengths for PEDOT:PSS as high as $\sim$44nm have been reported in the literature.[139] We argue that the higher values obtained here should be related to the superior conductivity of our PEDOT:PSS grade, even after DMAE modification. An increased ξ has been previously suggested by Xia *et al.*[131] for the same PEDOT:PSS grade used here. Our results confirm the claim, which has been attributed[131] to the higher molecular weight of the PEDOT:PSS grade used.

Having estimated ξ, we find a density of states $N^{1D}(\varepsilon_F)\approx$6.9x10^{6}eV^{-1}cm^{-1} for our modified PEDOT:PSS (pH 4). Note that this density of states is relevant only to the PEDOT chains participating in the transport. Assuming a rectangular density of states at the Fermi energy with a typical bandwidth of 0.5eV[140], we can obtain the 1D carrier concentration n. To convert to a meaningful three-dimensional n value, we compensate the 1D carrier concentration by the proportion of PEDOT to PSS chains in the solid (1:2.5 by weight), and obtain n$^{3D}\approx$1.4x10^{18}cm^{-3}. The obtained carrier concentration for our modified PEDOT:PSS (*p*H4) will be useful in the next section for the analysis of the magnetotransport measurements of spin-valve devices.

Although PEDOT:PSS retains similar temperature-dependent electrical response from bulk-like to the sub-micrometer regime, it is remarkable to find an increase in conductivity when the electrode spacing is reduced (see Figure 4.5(a,b)). Moreover, the conductivity increase is dependent on the temperature – the higher the temperature, the more the conductivity increases when electrode spacing is reduced, as highlighted in Figure 4.5(b). This scaling effect can be interpreted in terms of the localization of the carriers' wavefunction by the energetic and spatial disorder induced by the insulating PSS shells/lamellae, which surround the complex network of PEDOT:PSS conduction paths. In this context, the different rates at which the conductivity changes are an indication that the carrier's wavefunction can get localized when arriving at a PSS barrier. Or alternatively, it can tunnel through the insulating layer depending on the thermal energy available, the applied voltage bias, and the PSS shell thickness. Note that our

conductivity measurements were taken at low electric-field regime ($e\Delta V < k_B T$). In this limit, thermal effects are expected to become apparent in the material's electrical response. At room temperature, the PEDOT:PSS-rich areas are highly delocalized and impose little resistance to the carrier transport. Thermally-assisted tunneling through thin PSS layers is possible due to the available thermal energy, and consequently this is the strongest component of the measured resistance. Decreasing the system size reduces the amount of PSS barriers to transport, and as a result the measured conductivity increases. At low temperatures, the carriers percolate along the PEDOT:PSS-rich conduction paths with relatively high resistances, while tunneling through the PSS barrier is severely inhibited due to the lack of thermal energy. In this case, a weaker dependence of the conductivity with the system size is observed, given that the PSS no longer has such a strong influence in conductivity.

4.4 Tunnel-coupling of ferromagnetic electrodes to conducting polymers

Now we move our attention to the analysis of the NiFe/AlO$_x$/PEDOT:PSS/AlO$_x$/NiFe two-terminal spin valves. Ferromagnetic electrodes were engineered to have different coercive fields (Hc_{FM1} and Hc_{FM2}) by tailoring the width of the electrodes of each terminal. Magneto-optic Kerr effect (MOKE) microscopy has been used to verify the independent reversal of the NiFe/AlO$_x$ electrodes' magnetizations, with the application of an external in-plane magnetic field. As seen in Figure 4.6, two distinct coercive fields are observed, $Hc_{FM1} = 190$ Oe for the 80nm wide electrodes, and $Hc_{FM2} = 70$ Oe for the 280nm wide ones. The MOKE signal strength of the *FM²* electrodes is markedly stronger than the *FM¹* signal due to the higher surface area.

Current-voltage (*I-V*) measurements were conducted to examine the integrity of the device and its charge transport properties. It has been observed that the combination of solution-processed PEDOT:PSS at *p*H<4 with NiFe/AlO$_x$ nanoelectrodes was highly detrimental to the electrical stability of the junction (not shown). However, for the modified PEDOT:PSS at *p*H4, stable junctions were obtained, given that the noise level was generally only ~0.1% of the total current. Figure 4.7(a) shows the typical room-temperature *I-V* curves of the PEDOT:PSS spin-valves for different thicknesses of AlO$_x$ tunnel barrier and voltage bias up to 1V. The non-linear *I-V* response is symmetric and shows no hysteretic behavior, indicative of a good quality quantum-mechanical tunneling from the NiFe^{FM1} nanoelectrodes to the PEDOT:PSS through the AlO$_x$^{FM1}, and from the PEDOT:PSS to the NiFe^{FM2} through the AlO$_x$^{FM2}. Temperature-dependent
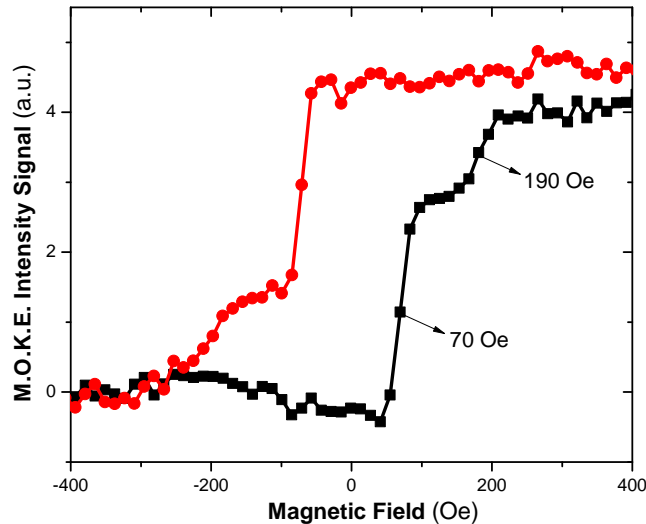
Figure 4.6: Magnetic hysteresis loops of the NiFe/AlO$_x$ nanoelectrodes measured by MOKE. Data was recorded in the actual spin-valve device at room temperature. Two distinct coercive fields are observed, Hc$_{FM1}$= 190 Oe for the 80nm wide electrodes, and Hc$_{FM2}$= 70 Oe for 280nm.

resistance measurements in the 300K-10K range were also carried out to confirm that the observed nonlinearity indeed originates from the tunneling barrier, rather than from space-charge limited transport in undoped PEDOT:PSS regions. As seen in Figure 4.7(b), the Resistance-Temperature (*R-T*) response of a representative device shows weak temperature dependence for several junctions within the chip, having different channel lengths: 200nm (black squares), 250nm (red circles), 380nm (blue triangles), and 480nm (inverted green triangles). The observed invariance of resistance as function of channel length, and the weak temperature-dependence is expected since the tunneling barrier dominates device resistance. Note that the PEDOT:PSS contribution to the series resistance was on the order of ∼400$m\Omega$ at room temperature, which is less than ∼0.001% of total junction resistance for the devices with the lowest impedances. From the combination of these results it becomes evident that the highly conductive PEDOT:PSS has been successfully integrated with the NiFe/AlO$_x$ spin-polarized tunneling electrodes.

One important requirement in the construction of spin valves for diffusive systems is the selection of appropriate interface resistance between FM electrodes and the non-magnetic spacer. Resistance-area products spanning over three orders of magnitude have been obtained by tuning the AlO$_x$ thickness – from 6x10$^{-7}\Omega m^2$ to 2x10$^{-4}\Omega m^2$ within the 17 devices measured. However, the detection of spin transport signal has remained elusive even for devices with the smallest electrode spacing (80nm), and at the lowest temperatures (down to 10K). This result is represented in Figure 4.8 (grey
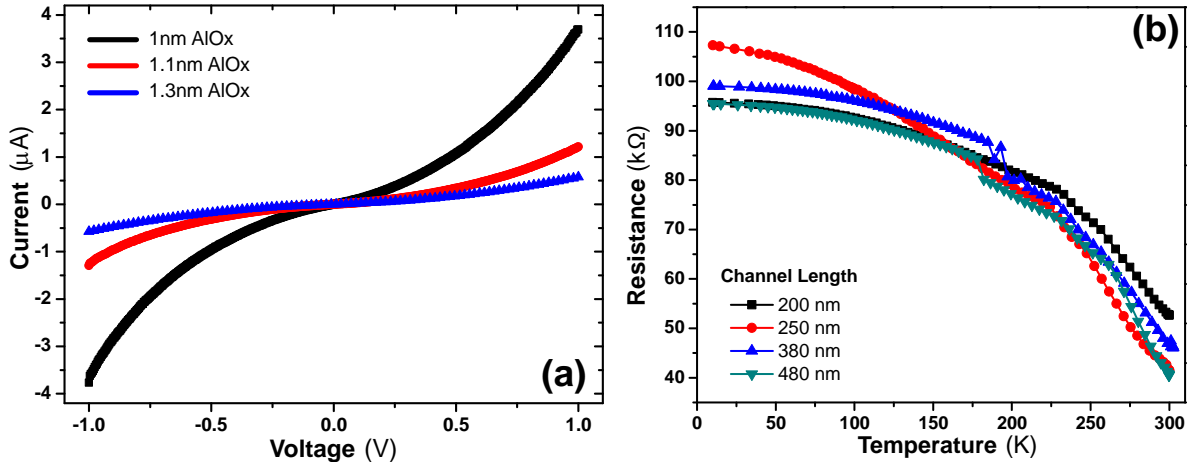
Figure 4.7: Electrical transport characteristics of the NiFe/AlO$_x$/PEDOT:PSS/AlO$_x$/NiFe lateral spin valves. (a) Current-voltage response of the spin-valves with different tunnel barrier thicknesses (indicated in the graph). (b) Resistance-temperature curve of an exemplary chip recorded from 300K to 10K. Spin-valve junctions with several channel length are plotted – 200nm (black squares), 250nm (red circles), 380nm (blue triangles), and 480nm (green inverted triangles). The measurement was performed applying a D.C. current of 1μA, and measuring the voltage of the two-terminal device.

symbols), wherein the normalized magnetoresistance is depicted as function of the RA products of the measured devices at room temperature. A typical magnetoresistance measurement sweep is shown in the inset of Figure 4.8 – the data were recorded at 10K, and the applied bias was 100mV for a PEDOT:PSS spin valve with 80nm channel length.

In view of our experimental results for the NiFe/AlO$_x$/PEDOT:PSS/AlO$_x$/NiFe structures combined with the material parameters acquired with the Au/PEDOT:PSS/Au lateral junctions (e.g. density of states and resistivity of PEDOT:PSS), we can now proceed to examine the absence of spin signal in our PEDOT:PSS spin valves with the theory developed by Fert & Jaffres for spin transport in diffusive systems.[59, 62] The magnetoresistive response of the NiFe/AlO$_x$/PEDOT:PSS/AlO$_x$/NiFe structures can be expressed as,[62]

$$\Delta R = \frac{2(\beta r_F + \gamma r_b)^2}{(r_b + r_F)\cosh\left(\frac{t_N}{l_{sf}^N}\right) + \frac{r_N}{2}\left[1 + \left(\frac{r_b}{r_N}\right)^2\right]\sinh\left(\frac{t_N}{l_{sf}^N}\right)} \tag{4.4}$$

where r$_b$ is the interface resistance value (RA product), r$_N$ is the spin resistance product for the non-magnetic spacer, $\rho_N l_{sf}^N$, and r$_F$ is the spin resistance product for the ferro-
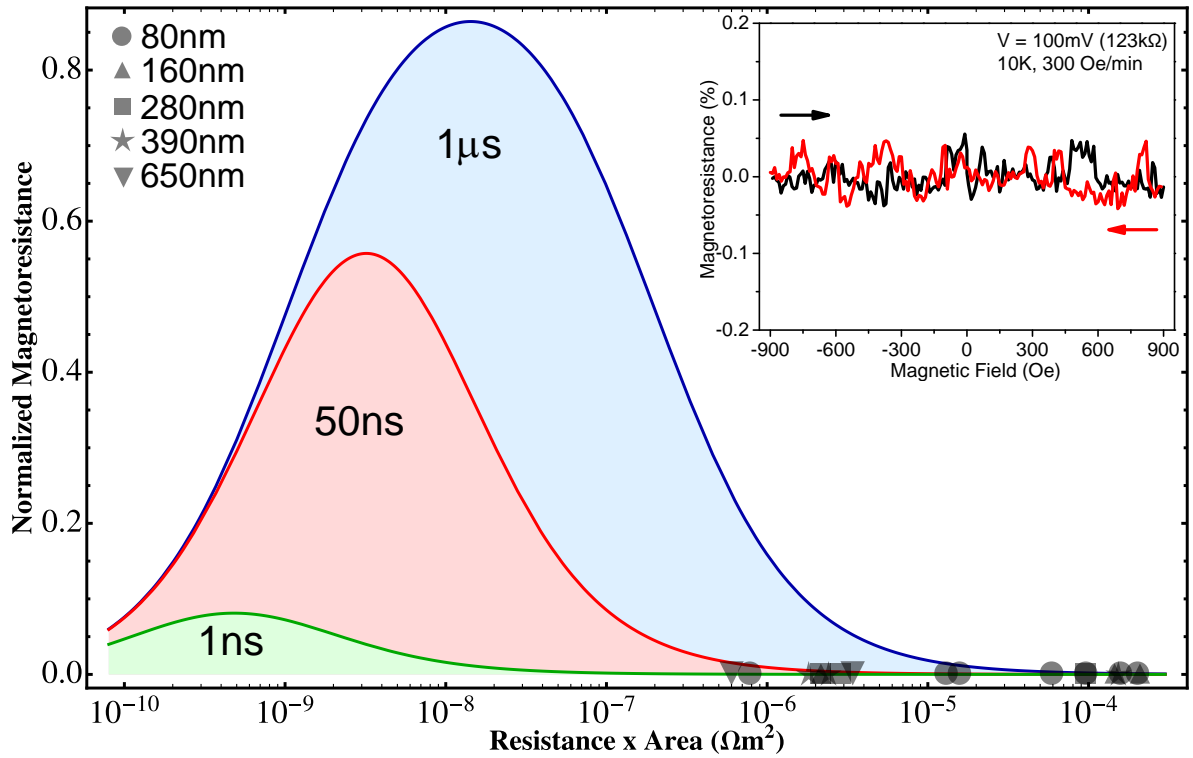
Figure 4.8: Magnetotransport characteristics of NiFe/AlO$_x$/PEDOT:PSS/AlO$_x$/NiFe spin valve devices. The experimental data points are shown as black symbols for different channel lengths. The calculated normalized MR for the smallest channel length (80nm) is represented as function of the RA product and spin lifetime in PEDOT:PSS (τ_{sf}). In the inset a typical experimental MR measurement result is depicted for a device with channel length 80nm, bias voltage 100mV, temperature 10K, and external magnetic field from -900Oe to +900Oe.

magnetic material, $\rho_F l_{sf}^F$. This equation holds for PEDOT:PSS thickness approximately equals the FM electrode width, which is the case for our lateral spin valves. The value of l_{sf}^N is unknown, while $l_{sf}^F = 5.5nm$ for NiFe ferromagnetic material.[141] We have conservatively set the interfacial spin-asymmetry coefficient γ, which is related to the spin-dependent interface resistance (AlO$_x$ tunneling barriers), to $\gamma = 0.3$.[70, 142, 143] This can yield a maximal magnetoresistance value of $\Delta R^{\mathrm{max}}/R_P = \gamma/\left(1 - \gamma^2\right) = 9.8\%$. The device resistance in the parallel configuration of the electrodes' magnetization R_P was computed using Eq.2.21. The degrading effect of interconnects/contact pads resistances (750Ω) was included in the calculation of R_P, and the bulk spin-asymmetry coefficient β of the NiFe ferromagnetic electrodes was set to $\beta = 0.7$.[144] The value of r$_N$ is calculated using,[62]

$$r_N = \frac{\hbar\pi}{(3\pi^2)^{\frac{1}{6}}e^2}\sqrt{\frac{\tau_{sf}}{2\tau}}n^{-2/3} \tag{4.5}$$

in which PEDOT:PSS is taken as a degenerately doped semiconductor. Material parameters for the modified PEDOT:PSS ($pH4$), such as carrier concentration $n \approx 1.4 \times 10^{18} cm^{-3}$ and resistivity $\rho_N \cong 9m\Omega cm$, were input from the study of the local charge transport with the Au/PEDOT:PSS/Au lateral junctions.

It is important to note that although the theory was initially developed for metals/semiconductors, it may be extended to our highly-doped organic semiconductor, given that it retains metallic electrical characteristics in most of the temperature and voltage range evaluated. This is shown in Figure 4.8 for the smallest channel length (80nm), taking the unknown spin lifetime $\tau_{sf} = 1ns$(green), 50ns (red), and $1\mu s$(blue). The calculations revealed that measurable magnetoresistance values could only be detected for a narrow range of interface resistances in our PEDOT:PSS spin valve. Moreover, we observe that the high interface resistances obtained with AlO_x barriers (grey symbols) might actually prejudice the chances of having a measurable spin signal. It is noticeable, however, that if the spin lifetime were $\tau_{sf} \geq 50ns$ (blue and red regions), we should have been able to detect MR in some of our devices. This allows us to estimate an upper limit to the spin lifetime in PEDOT:PSS to $\tau_{sf} \leq 50ns$, which has been calculated by conservatively setting the minimal measurable MR signal to 0.1%, see also inset of Figure 4.8.

This result suggests the use of alternative tunnel barriers that are sufficiently transparent for electron tunneling and chemically stable to the acidic PEDOT:PSS solutions. For instance, the well-established MgO tunnel barriers would qualify from the electrical standpoint (RA products on the order of $10^{-11}\Omega m^2$ to $10^{-8}\Omega m^2$),[145, 146] but success may still be hindered due to its low chemical stability in acidic aqueous solutions.

Perhaps the main outcome of our interpretations, irrespective of the absence of spin signal in the experiment, is the possibility of estimating the upper limit for the spin lifetime of carrier diffusion in PEDOT:PSS ($\tau_{sf} \leq 50ns$). This result suggests that early electron paramagnetic spin resonance observations of spin lifetimes in organic conductors (e.g. polyaniline with $\tau_{sf} \geq 1\mu s$)[147] may not be directly applied to spin transport studies. Nonetheless, further studies can be carried out on alternative spin-tunnelling electrodes with high spin polarization, in order to verify whether spin transport in PEDOT:PSS can be achieved at lower values of interface resistance.

4.5 Conclusions

We have presented charge transport studies of spin-coated PEDOT:PSS with ohmic and spin-polarized tunnel contacts at nanoscale lateral dimensions. The approach used allowed us to fabricate well-defined lateral devices, while preventing any damage to the organic film and interfacial metal diffusion from top electrodes. We have experimentally demonstrated the non-linear enhancement of the conductivity of PEDOT:PSS upon the reduction of the electrode separations at sub-micrometer scales. This previously unreported scaling effect is a characteristic feature of hopping charge transport in highly disordered systems, which, in our particular case, is revealed when the device's lateral dimensions approach the spatial extent of the carriers' wavefunction localization induced by disorder.

Due to the highly delocalized nature of this doped organic semiconductor and consequent superior diffusivity of carriers, we have fabricated two-terminal lateral spin-valve devices to address its spin transport properties. To that end, we have demonstrated the feasibility of integrating the traditional $NiFe/AlO_x$ spin-polarized tunnel electrodes with PEDOT:PSS when the polymer solution is increased to pH=4. This procedure is not limited to the $NiFe/AlO_x/PEDOT:PSS$ system, but may be extended to other conducting polymers and FM metal electrodes. We do not observe any measurable MR signal in our $NiFe/AlO_x/PEDOT:PSS/AlO_x/NiFe$ lateral spin valve structures, which we attribute to the high RA products obtained with the AlO_x tunnelling barriers (10^{-7} to $10^{-4}\Omega m^2$). However, the agreement with theoretical predictions suggests the use of a rather lower interfacial resistance between PEDOT:PSS and NiFe to transform the spin information into significant MR electrical signals. Moreover, we have found an upper limit for the spin lifetime $\tau_{sf} \leq 50ns$, which is an invaluable material input for further investigations.

5 Mixed Self-Assembled Monolayer Gate Dielectrics For Low-Voltage Solution-Processed Polymer Field Effect Transistors

In this Chapter, ultrathin hybrid gate dielectrics based on aluminum oxide (AlOx) and a mixed-type phosphonic-acid self-assembled monolayers (SAM) are studied with a high performance liquid-crystalline semiconducting polymer, viz. poly(2,5-bis(3-alkylthiophen-2-yl)thieno[3,2-b]thiophene (pBTTT). We demonstrate that by tailoring the assembly of carboxylate terminated SAMs one can obtain high surface energy, while recovering the leakage current levels obtained with high quality methyl terminated monolayers. We also study the impact of the underlying patterned gates on the morphology of pBTTT, and find that terrace-like microstructure can be formed on simple thermally evaporated aluminum gates. A strong improvement of the field-effect transistor characteristics is observed when the concentration of carboxylate groups is reduced.

5.1 Mixed phosphonic-acid SAM for lithographically patterned OFETs

Solution-processable semiconducting polymers have attracted substantial interest in recent years due to their potential for low-cost, large-area device fabrication. Performance has constantly been improved, with field-effect mobilities reaching benchmark values of ≥ 1 cm^{2}V^{-1}s^{-1}.[32, 148–150] High-performance materials are generally comprised of a rigid π-conjugated polymer backbone functionalized with regularly spaced alkyl side-chains. This molecular design promotes intra/interchain π-π stacking, while allowing the formed crystallites to align parallel to substrates with appropriate surface chemistry. An example for this class of material is the liquid crystalline semiconductor
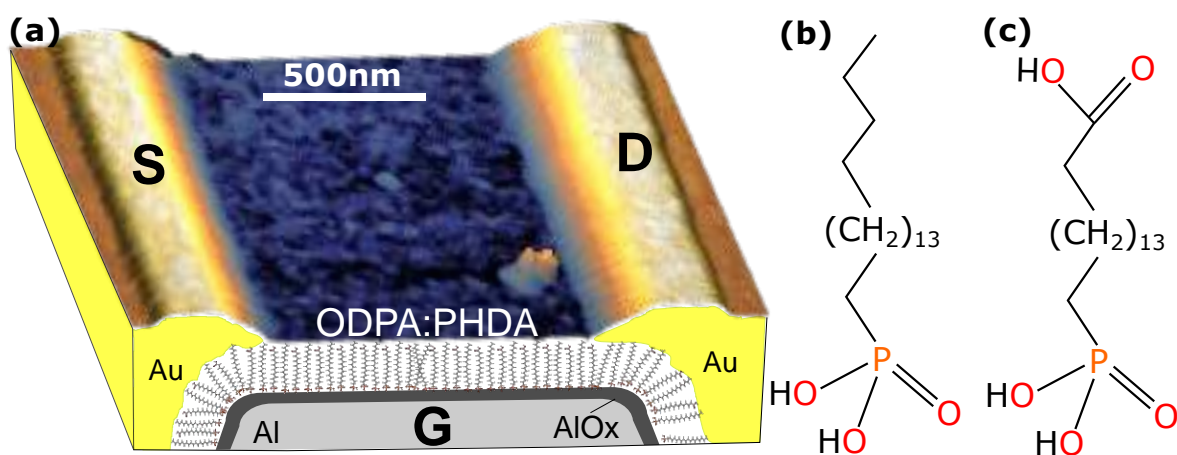
Figure 5.1: (a) Schematic representation of the organic transistors with patterned hybrid gate electrodes, prior to spin-coating of pBTTT. A three-dimensional atomic force microscopy image is embedded in the scheme for a device with Al/AlOx functionalized with PHDA:ODPA(1:1). The molecular chemical structures are represented in (a) for ODPA, and (b) for PHDA.

polymer poly(2,5-bis(3-alkylthiophen-2-yl)thieno[3,2-b]thiophene (pBTTT) introduced in Section 1.2.1. It shows long-range two-dimensional order,[32] as well as very high field-effect mobilities (0.1–$1 \ cm^2V^{-1}s^{-1}$).[151, 152] One key step towards the realization of circuitry based on semiconducting polymers is the development of organic field-effect transistors (OFET) operating at low supply voltages, and consequent low power consumption. A very attractive route has been proposed by Klauk *et al.*[153], wherein they use a hybrid gate dielectric comprised of a thin AlOx and an aliphatic phosphonic-acid (PA) self-assembled monolayer (SAM) to provide high capacitive coupling and low leakage currents. However, due to the very low surface energy obtained with this functionalization, conventional polymer processing methods becomes challenging (e.g. spin-coating).[154] To solve this issue, Ball et al.[155] have proposed the use of carboxylate terminated PA-SAMs (16-phosphonohexadecanoic acid, PHDA, Fig. 5.1) to increase the surface energy and thus to allow solution processing. However, this has in turn increased the leakage current through Al/AlOx gate dielectrics.

In this Chapter we show that by functionalizing patterned aluminum gate electrodes with a mixed-type self-assembled monolayer combination – PHDA and octadecylphosphonic acid (ODPA) –, one can simultaneously have increased surface energy while recovering the insulating performance obtained with highly hydrophobic ODPA-based gate dielectrics. The power of this mixed-SAM approach is demonstrated by fabricating solution-processed OFETs with patterned hybrid gate electrodes by standard lithographic methods. The transistors were tested with pBTTT, whose morphology and electronic properties critically depend on interface chemistry[156] and roughness[157].

Therefore, pBTTT is an ideal candidate to test the quality of the hybrid gate dielectrics.

We present the electronic transport properties of transistors with Al/AlOx gate electrodes functionalized with three different SAM types: (1) PHDA-only, (2) mixed PHDA:OPDA, and (3) mixed PHDA:OPDA with ODPA-only channel. Devices prepared with mixed SAMs show steeper subthreshold swing and over two orders of magnitude lower leakage currents, as compared to the PHDA-only case, whereas full hole mobility is obtained only for the devices with an ODPA-channel. We also studied the impact of the underlying SAMs on the semiconductor morphology by atomic force microscopy (AFM). For ODPA-only monolayers, we observed well-ordered pBTTT terrace-like domains, after annealing above the mesophase transition temperature. This is an interesting result since terraces can only form on very smooth surfaces, while thermally evaporated aluminum (Al) films are generally very rough.

5.2 Device Fabrication

Figure 5.1(a) and Figure 5.2 show an exemplary atomic force microscopy (AFM) and an optical image of the transistors studied here, respectively. The devices were fabricated with a two-step electron-beam lithography process to define the gate (G), source (S), drain (D), and guard electrodes. Degenerately As-doped silicon wafers with 150nm thermally grown SiO_2 insulator were used as substrates. The gate electrodes were patterned in the first lithographic step using an PMGI/PMMA double-layer resist combination, and with high deposition rates of Aluminum ($\sim$100Å/s). Further details on the lithographic and deposition steps have been given in Chapter 3, Sections 3.2 and 3.3, respectively. The resulting Al patterns (20$\pm$3nm thick) were subjected to an oxygen plasma treatment (Parallel Plate Oxford Plasma System 80Plus, 220mW, 20min, 20sccm, 5mbar, 13.56MHz) to produce aluminum oxide (AlOx) of defined thickness, to enhance its quality[158], and create a high concentration of hydroxyl groups at the surface upon exposure to air.[1] The samples are then immersed in 1mM solutions of ODPA, PHDA, or a mixture of both in 2-propanol. Substrates are taken from solution after 1h, rinsed with 2-propanol, and baked at 65°C for 10min in a hot-plate. Low power ultrasonication with 2-propanol removed physisorbed molecules, before the assembly was continued in fresh ODPA solution (healing phase). The surface energy resulting from the assembly of PHDA:ODPA (1:1, for 1h) healed with ODPA has been sufficient to allow spin-coating of PMMA (dissolved in Anisole) absent of the usual dewetting

---

[1]Samples for leakage current measurement and contact angle measurement (Figure 5.3) were treated with a low-energy Diener Pico System, 100W, 20min, 20sccm, 2mbar
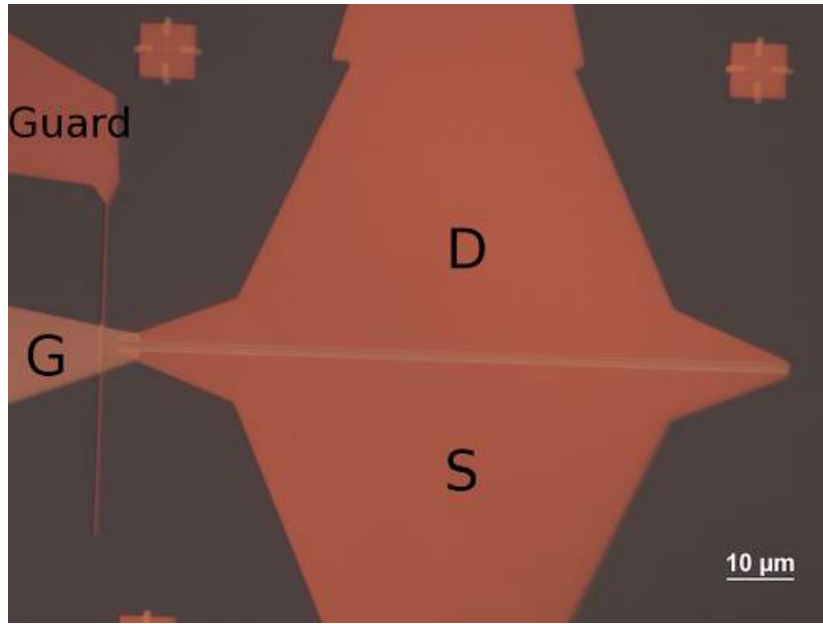
Figure 5.2: **Optical microscopy image of a typical transistor.** Source (Au), drain (Au), guard (Au), and gate (Al/AlOx/PA-SAM) electrodes are clearly visible in the image. Channel length (L) is 1μm, whereas the width (W) is 100μm. pBTTT thin films are spin-coated onto these structures in order to complete the fabrication process.

problems.

Source, drain and guard electrodes are patterned in a second lithography step with a double-layer PMMA resist combination (as of Figure 3.2). We deposited 0.3nm of titanium (Ti) as adhesion layer by electron-beam evaporation[159, 160], followed by the thermal evaporation of 35nm of gold (Au). The lift-off was performed in warm acetone, and rinsed with warm 2-propanol. This carefully optimized process results in hybrid gate dielectrics with routine root-mean-square roughness $Rq \cong 0.3$nm, as indicated in Fig. 5.1(a). The devices were transferred into a N_2-filled glove-box ($<0.1ppm$ O_2 and $<0.1ppm$ H_2O), and thin pBTTT films were cast via spin-coating from warm 1,2-dichlorobenzene (DCB, $0.5\%_{w/w}$). The resulting pBTTT films have thicknesses of ca. 25nm, as measured by stylus profilometry. All transistors had a fixed channel width (W) of 100μm, and the channel length (L) varied from 40μm down to 0.5μm. A guard electrode was positioned next to the source and drain contacts in order to eliminate fringe currents in the unpatterned semiconducting layer, thus preventing overestimation of mobility and reducing the gate current (I_{gs}). This was done in order to simulate the operation of the transistor as if the pBTTT layer was patterned[161] on top of the gate dielectric. All measurements were performed in vacuum ($<2 \times 10^{-4}$mbar) after a short exposure to ambient air (<30s).

5.3 Influence of self-assembled monolayer dielectrics on pBTTT morphology

To evaluate the characteristics of the phosphonic-acid SAM (PA-SAM) type and process method we performed static contact angle (SCA, 1μL H_2O, 60% air humidity) measurements and two-terminal current-voltage (I-V) measurements. Current densities were analysed with Al/AlOx/PA-SAM/Au stacks with varied junction areas $(1.2$–$2.5{\times}10^{-4}cm^2)$. In Figure 5.3(a) the SCA is plotted for a range of ODPA:PHDA molar fractions, with total concentration kept at 1mM. The black curve displays the SCA of samples immersed in PA-SAM solution overnight, which indicates that the surface energy is enhanced when the PHDA fraction is increased. SCA values obtained for PHDA-only surfaces are in agreement with values obtained previously in the literature[155]. Curiously, we found that by re-immersing fully assembled and stabilized monolayers into a solution of pure ODPA, SCA values significantly increased for PHDA-containing monolayers (red data points). We attribute the loose bonding to surface coordination with the carboxylate terminus, in agreement with recent studies[162], which show that molecules with phosphonic acid groups can replace carboxylate-bound molecules on AlOx surfaces.
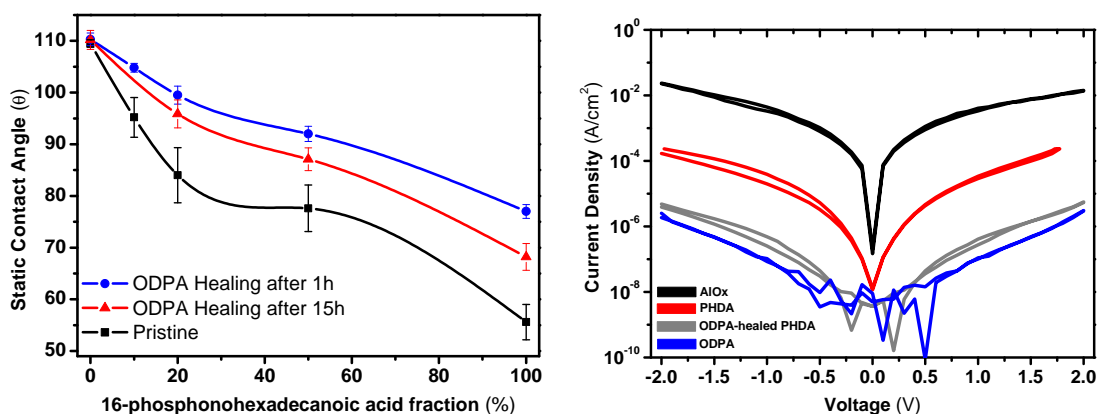
Figure 5.3: The healing effect of ODPA on mixed-type SAMs. (*top*) The water static contact angles (SCA) for various fractions of PHDA:ODPA. *Black squared* symbols represents the SCA for a one-step assembly. The *red triangle* symbols for fully assembled substrates (>15h) healed with ODPA. *Blue circles* symbols for substrates with incomplete assembly ($\sim$1h) healed with ODPA. (*bottom*) Current densities for Al/AlOx/PA-SAM/Au junctions and an Al/AlOx/Au reference junction (*black curve*).

The outstanding robustness achieved with phosphonic acid-bound SAMs with Al gates[163] can be partially attributed to the bonding strength of the phosphonate groups to AlOx

surfaces. In turn, monolayers containing weakly (carboxylate-) bound PHDA molecules are expected to have poorer insulating performance than the purely phosphonate-bound ones. In Figure 5.3(b) we show the current densities recorded for a reference AlOx junction (black), PHDA-only (red), PHDA:ODPA(1:1) healed with ODPA (grey), and a junction based on pure ODPA (blue). The increase in current density for PHDA monolayers in comparison to ODPA monolayers is of the same order of magnitude ($\sim 10^2$) of values reported in the literature[155]. By contrast, for the mixed SAM we observe a remarkable enhancement in insulation, which is imparted by the ODPA healing step. Leakage currents reduces by nearly two orders of magnitude, approaching the quality obtained with ODPA-only monolayers. More importantly, lithographic patterned electrodes can be defined since the surface energy is sufficiently high for resist spin-coating. However, we noticed that for healed mixed-type SAMs with molar fractions lower than (1:1) PMMA dewetting would occur upon spin-coating. Therefore, for all lithographically patterned transistors of mixed-type SAM we used exclusively PHDA:ODPA at (1:1) proportion.

5.3.1 pBTTT thin films on patterned Al/AlOx/PA-SAM gate electrodes

Morphological studies of pBTTT thin-film have been extensively reported in the literature for various types of substrate surfaces.[164, 165] However, to our knowledge, no study has been reported on pBTTT morphology formation on patterned gate dielectrics based on Al/AlOx/PA-SAM. The formation pBTTT molecular terraces has been shown to be disrupted on rough surfaces ($Rq < 0.5$nm[157]) and/or for surfaces with high surface energy. Although low surface energy is easily attainable with appropriate surface functionalization, obtaining Al surfaces roughness with $Rq < 0.5$nm generally poses challenges. However, we found that by controlling evaporation rates of Al to around 80–120 Ås^{-1}, $Rq < 0.35$nm can be routinely obtained (see Section 3.3 for details). At these surface roughness levels, pBTTT films on ODPA-terminated gate dielectric show clear terrace-like domains upon annealing above the mesophase transition temperature ($\sim 145°$C, Ref. [166]). Atomic Force Microscopy (AFM) images taken in the transistor channels functionalized with ODPA post-lithographically are shown in Fig. 5.4(a,b,c). Terraced domains of pBTTT (step height 2.1nm) can be easily distinguished for lower roughness channels ($Rq < 0.31$nm, Fig. 5.4(a,b)), while for rougher Al/AlOx/ODPA gates ($Rq \sim 0.65$nm, Fig. 5.4(c)) the terraced domains are no longer observed. This is in agreement with a similar study made with SiO_2/OTS based dielectrics[157].
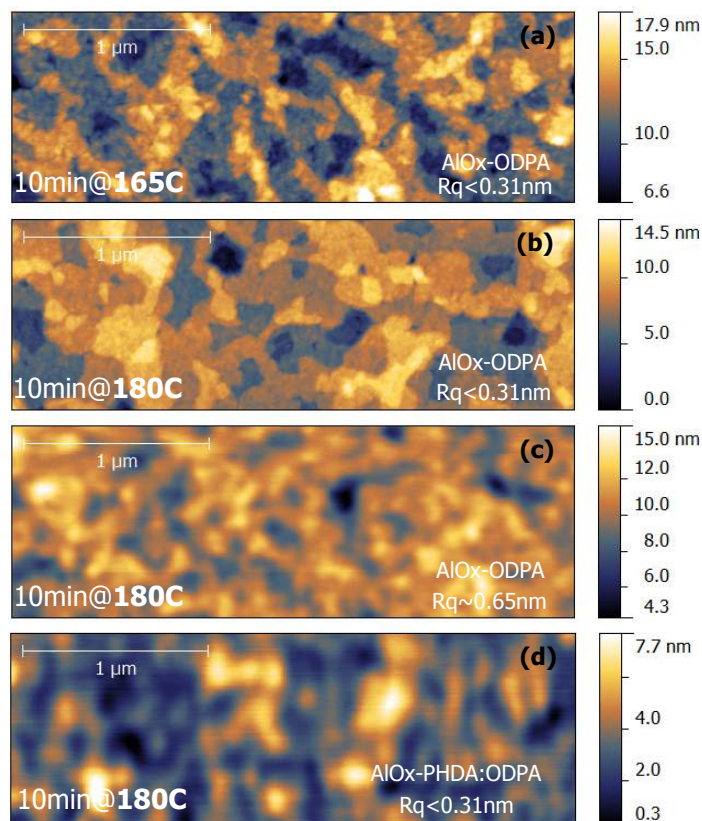
Figure 5.4: AFM images of annealed pBTTT on Al/AlOx gates functionalized with ODPA or PHDA:ODPA (1:1, healed with ODPA). The impact of the annealing temperature on smooth ODPA-only channels ($Rq<0.31$nm) is evaluated for (a) $T = 165°$C, and (b) $T = 180°$C. In (c), an image of a rougher ODPA-only channel ($Rq\sim0.65$nm) annealed at $T = 180°$C. In (d), an image of pBTTT on smooth channel ($Rq < 0.31$nm) with mixed-type SAM annealed at $T = 180°$C.

Devices annealed at 180°C displayed noticeably better defined terraces as compared to devices annealed at 165°C. Annealing at 165°C for a longer period (30min) did not improve the definition of the terraces, as seen in Figure 5.5. An AFM image of pBTTT coated on ODPA-healed PHDA:OPDA(1:1) surface is shown in Fig. 5.4(d). Molecular terracing has not been observed, even though the device channel possessed low surface roughness. This finding emphasizes the importance of the chemical nature of the dielectric surface. It has been previously reported that sharp and small pBTTT terraces can form on clean SiO_2 surface upon annealing[156]. Surface energies observed for UV cleaned SiO_2 is usually significantly higher ($\Theta_{SCA}<10°$) than what we obtain with ODPA-healed PHDA:OPDA(1:1) ($\Theta_{SCA} = 92 - 94°$). However, the presence of sparse $-COOH$ functional groups connected to a relatively flexible alkyl chain (C15) has proven effective in hindering reorganization of pBTTT crystallites upon annealing.
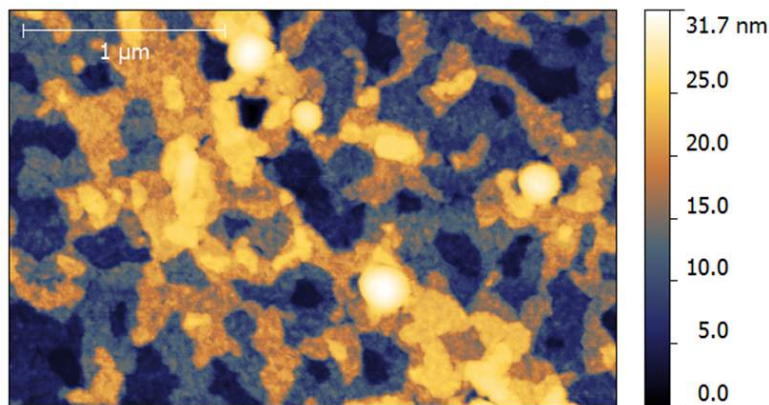
Figure 5.5: Effect of extended annealing time on pBTTT thin-film on a Al(20nm)/AlOx(4nm)/ODPA gate electrode. This image represents the annealed (10min at 165°C) sample of Figure 5.4(a) further annealed at the same temperature for 20min. The surface roughness over the pBTTT terraces decreases only slightly with the extra annealing time.

It thus seems clear that the morphological characteristics of pBTTT on mixed PA-SAMs cannot be explained only in terms of surface energy. We therefore propose that the side chains (C16) of pBTTT intercalate with the underlying mixed-type PA-SAM in the annealing process. Interdigitation of alkyl side chains of polythiophene-based based semiconductors (e.g. poly(3-hexylthiophene-2,5-diyl)) with the alkyl chains of monolayers is known to occur.[167] In this scenario, carboxylate end groups can readily interact with the polymer backbone. In contrast, less reactive and rigid SiO_2 surface cannot interact easily with the pBTTT backbone, given that its C16 side chains protect the semiconducting core.

5.3.2 pBTTT thin films on ultrasmooth atomic layer deposited AlOx functionalized with mixed PA-SAM

In order to confirm the effect of the PA-SAM on the pBTTT morphology described in the previous section, we have prepared samples for several PHDA:ODPA fractions (as of Fig. 5.3(*left*)) on ultra-smooth atomic layer deposited (ALD) AlOx substrates. This allows the exclusion of the disturbance of roughness on the morphology, and further verify the effect of sparse -COOH endgroups. For these samples, *ODPA healing step* was performed in order to remove loosely bound PHDA molecules that could compromise pBTTT crystallization.

Figure 5.6 displays the AFM images for five different PHDA concentrations. Sample processing and characterization was done in parallel with the samples used for SCA
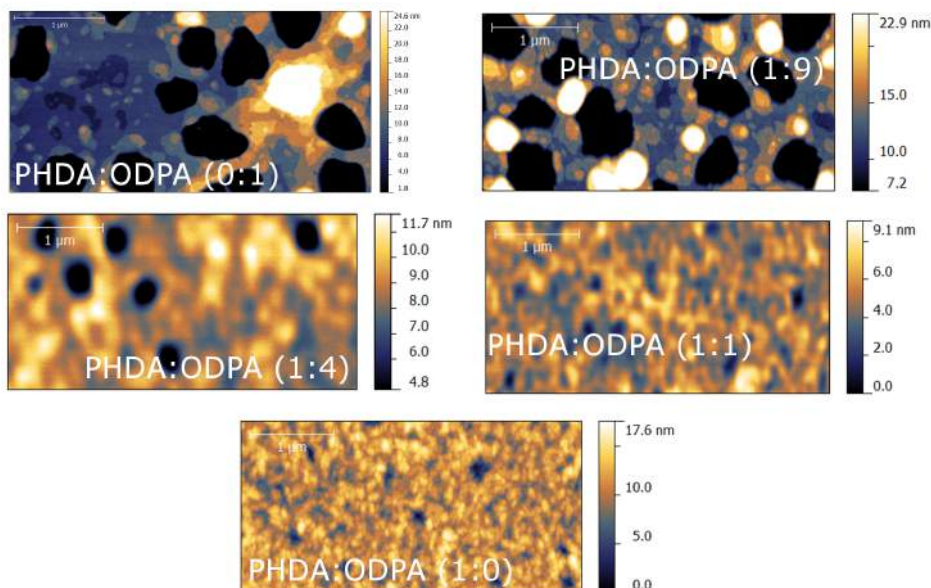
Figure 5.6: AFM images of spin-coated and annealed (180°C, 10min) pBTTT thin-films on ultrasmooth ODPA-healed PA-SAM/ALD-AlOx (Rq<0.17–0.22nm). As indicated, the SAM's PHDA:ODPA molar fraction was varied from (0:1, pure ODPA) to (1:0, pure PHDA). Molecular terracing is observed for the sample with the lowest fraction of PHDA (1:9), and pure ODPA (0:1).

and J-V analysis of Fig. 5.3(a). The r.m.s. surface roughness of the samples after PA-SAM assembly was around 0.17-0.2nm, as measured by AFM (not shown), ruling out therefore roughness disturbances. As it is observed, dewetting is reduced as PHDA concentration is increased and, concurrently, molecular terracing is disrupted. All images were carefully taken with the same AFM tip. The tip condition was checked before and after each image with the well crystallized PHDA:ODPA(0:1) as reference sample.

We observe pBTTT reorganization/crystallization only for PA-SAM prepared with initial PHDA molar concentration <10%. The real concentration after the ODPA healing step was not quantified. It is interesting to observe that even for samples with water contact angle 100°(ODPA-healed PHDA:ODPA 1:4), the pBTTT does not crystallize with thermal annealing but still show some degree of dewetting. This indicates that dewetting occur mostly in the spin-coating process, and is not directly induced by the thermal annealing. The images also independently confirm the dramatic sensitivity of the pBTTT crystallization to sparse -COOH endgroups.

5.4 Low-Voltage pBTTT field-effect transistors based on mixed-type PA-SAM

Figure 5.7 displays the transfer and output characteristics of pBTTT low-voltage transistors with three types of gate dielectrics. Two devices (Fig. 5.7(a,b)) were fabricated with mixed- SAM PHDA:ODPA(1:1) healed with ODPA. The third device (Fig. 5.7(c)) was fabricated with the gate dielectric functionalized with pure PHDA (1:0). One of the mixed-SAM devices was further processed, and had its channel monolayer replaced by pure ODPA (0:1) (Fig. 5.7(a)). The leakage currents, on-off current ratios I_{DS}^{ON}/I_{DS}^{OFF}, and subthreshold swing are significantly improved for devices prepared with the mixed-type SAM, as compared to PHDA-only devices. Leakage currents decreased by a factor of $\sim$10 (evaluated at $V_{DS} = -2.5$ V and $V_G = -3$V), whereas I_{DS}^{OFF} decreased by two orders for the mixed-type SAM. The off-current increase for PHDA-based OFETs is in contrast to the results reported in Novak *et al.*;[168] however, these data have been obtained with the comparatively small molecule α-β-dihexylquaterthiophene (DH4T), and importantly, without thermal annealing. Hence side chain interdigitation with the underlying PA-SAM cannot be expected.

We partially attribute the observed off-current increase to doping of the first pBTTT layer by the PHDA endgroups. Leakage current and I_{DS}^{OFF} of OFETs with patterned bottom-gate with overlapping bottom-contact geometry (BGBC) are highly sensitive to the thickness and quality of the gate dielectric. Particularly, the I_{DS}^{OFF} of transistors with very thin hybrid dielectrics can also include spurious contributions from S/D current leaking through the gate electrode. We argue that the off-current degradation observed for the PHDA-only pBTTT transistors has a two-fold origin – the doping effect of the carboxylate-terminated SAM, and the increased contribution from spurious gate currents. In contrast, ODPA-healed PHDA:ODPA(1:1) SAM has a much smaller density of carboxylate groups, and provides excellent insulation from S/D and gate electrodes. The mixed-SAM approach can thus reduce I_{DS}^{OFF}, and consequently increase the I_{DS}^{ON}/I_{DS}^{OFF} ratio of lithographically defined pBTTT OFETs.

The subthreshold swing S_{s-th} becomes sharper with decreasing PHDA content – $S_{s-th} = 213$mV/dec (for PHDA-only 1:0), $S_{s-th} = 106$mV/dec (for mixed ODPA-healed PHDA:ODPA(1:1)), and $S_{s-th} = 119$mV/dec (for ODPA-only 0:1 channels). This is followed by a variation of the subthreshhold voltage – $V_{th} = -1.5$V (for PHDA-only 1:0), $V_{th} = -1.4$V (for mixed ODPA-healed PHDA:ODPA(1:1)), and $V_{th} = -1$V (for ODPA-only 0:1 channels). As shown in Figure 5.8, the capacitance per unit area (C_i) values were found to vary for the different types of SAM used: 0.78µF/cm^2 for ODPA-only, 0.8µF/cm^2 for ODPA-healed
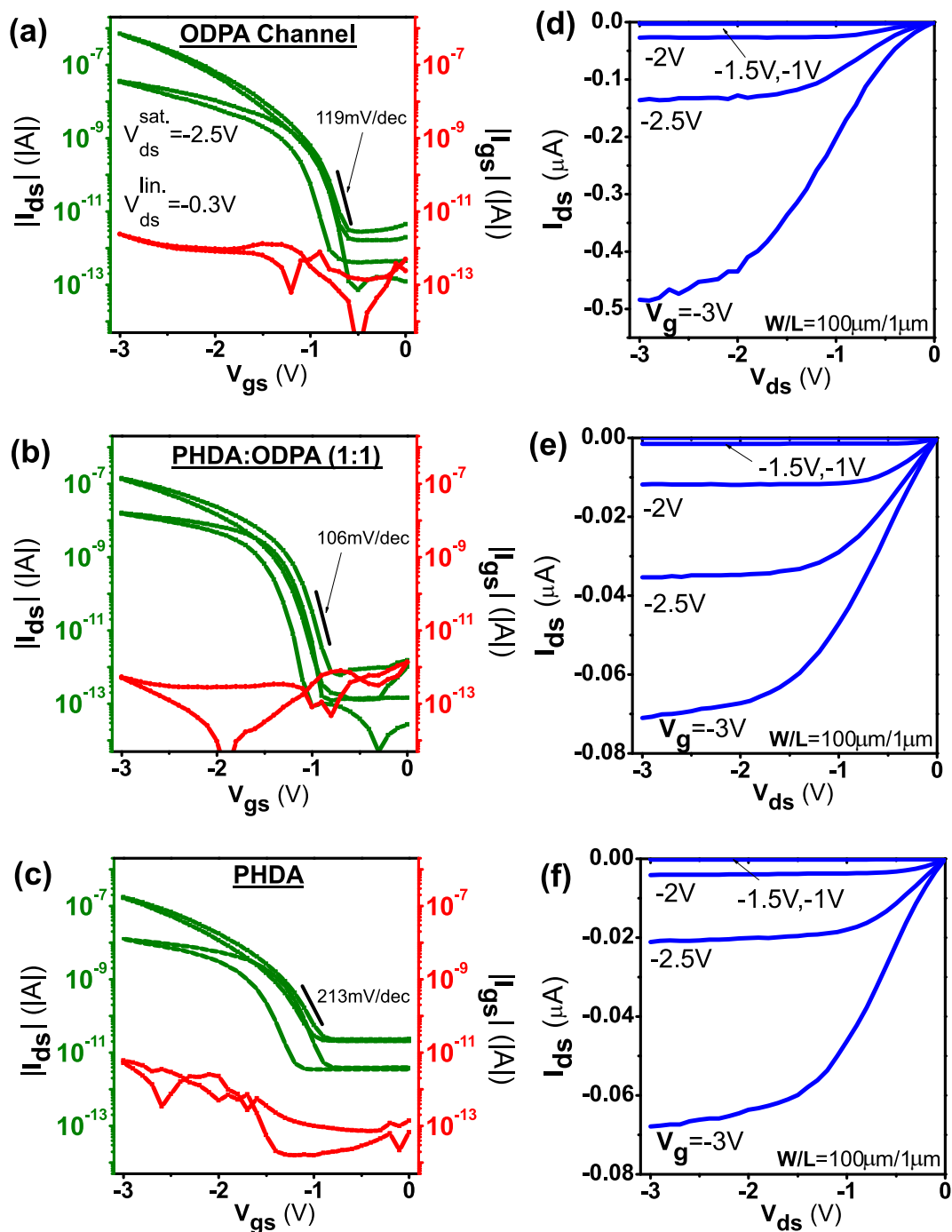
Figure 5.7: Electrical properties of lithographically patterned pBTTT transistors. The transfer and output characteristics are depicted for transistors with $W/L = 100\mu m/1\,\mu m$, measured at room temperature and high vacuum. In (a,d) a transistor patterned with PHDA:OPDA(1:1, healed with ODPA) with ODPA-only channel. In (b,e), the transfer and output curves for a PHDA:OPDA(1:1, healed with ODPA) channel. In (c,f), transfer and output curves for a transistor fabricated with PHDA-only monolayer.
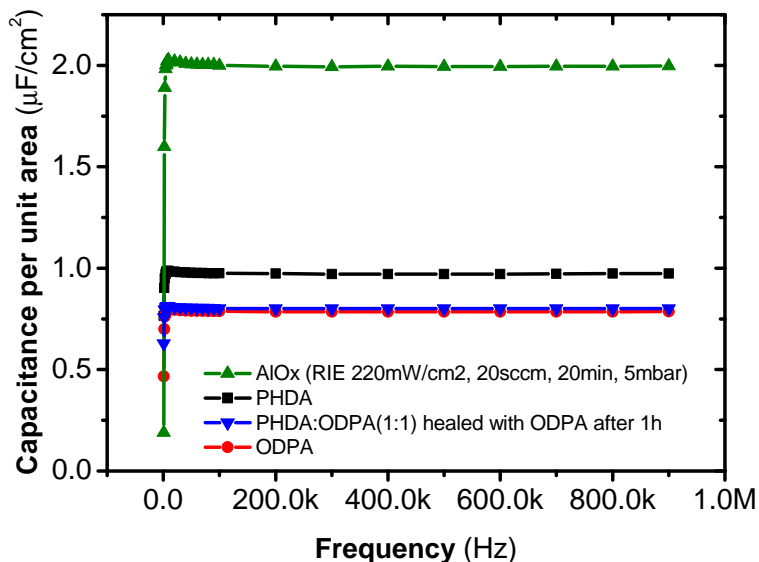
Figure 5.8: **Capacitances of AlOx and the PA-SAM/AlOx dielectrics.** The measurements were recorded with a Keithley 4200-SCS parameter analyser, for a range of junction areas (1.2–$2.5{\times}10^{-4}$cm^2), and Au top electrodes deposited through shadow mask. The AlOx had a thickness of ${\sim}4$nm (measured by X-Ray Reflectivity), resulting in a calculated relative permitivity of $\varepsilon_r \approx 9$. The increased areal capacitance of the PHDA-only layer can be attributed to a higher defect density of the SAM. The measurement was done with bias 3V($\sim$30mV) up to 1 MHz.

PHDA:ODPA(1:1), and 0.99µF/cm^2 for PHDA-only (1:0) transistors. Field-effect mobilities were calculated with their respective capacitance values in the saturation regime ($V_{DS} = -2.5$V), with Eq.2.11 (Chapter 2). Devices with ODPA-only (0:1) channel had the best performances, with hole mobilities approaching ~ 0.1cm^{2}V^{-1}s^{-1} for long-channel transistors. On the other hand, PHDA-containing devices exhibit lower field-effect mobilities, irrespective of the carboxylate concentration in the interface. It is interesting to observe that although the reduction of the PHDA fraction improves the overall performance (e.g. on-off current ratios and subthreshold swing), the field-effect mobilities do not improve significantly. We attribute this to the strong disorder in the pBTTT morphology induced by PHDA, as observed by AFM (Figure 5.4). Therefore, the formation of long-range order pathways for charge carrier transport is hindered since pBTTT crystallites are pinned at the interface.

For PHDA-containing devices, the channel resistance (R_{Ch}) dominates the device response, whereas for devices with ODPA-only channel the contact resistance (R_C) is prevalent. This is seen in Figure 5.7 as a strong reduction of carrier mobility with channel scaling for ODPA-only channel, whereas for PHDA-containing long-channels ($\geq$2.5µm) the mobility is nearly constant. Noticeably, for PHDA-containing devices
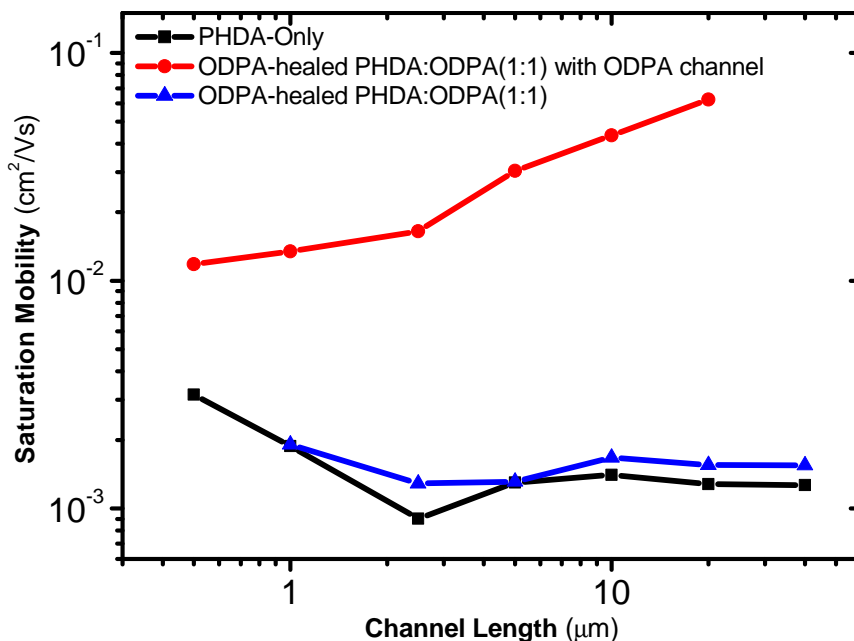
Figure 5.9: Extrinsic charge carrier mobility calculated in the saturation regime (μ_{sat}, V_{ds}=−2.5V) after annealing at 165°C. Mobility values are shown for devices of Fig. 5.7 with fixed channel width ($W = 100$ μm) and varying the channel length from 40μm to 0.5μm.

the mobilities tended to increase with the reduction of channel length (≤ 2.5μm). A similar effect has been previously reported by Hamadani *et al.*[151] and was attributed to a Poole-Frenkel-like ($\mu \propto \exp\left[\sqrt{\overrightarrow{E}}\right]$) behavior of pBTTT, in which the field-effect mobility depends on the lateral electric strength induced by S/D electrodes. This can be observed in annealed pBTTT transistors with low contact resistance, by using platinum S/D electrodes.[169] In contrast, in our PHDA-containing devices $R_{Ch} \geq R_C$ and, as a result, channel effects are much more apparent, even with transistors with relatively high R_C (Au/pBTTT). Thus, the mobility increase can be interpreted within the framework of the Poole-Frenkel formalism as field-induced lowering of the energy barrier for carrier hopping in disordered, trap-limited pBTTT.

5.5 Conclusions

In summary, we have shown a simple two-step assembly process for mixed phosphonic acid (PA) monolayers to obtain high surface energy, while preserving good insulating properties. Our results strongly suggests that the anchoring of PHDA molecules on AlOx surfaces is not given exclusively via de PA terminal groups, which explain its inferior insulating performance. We combined our method with standard lithography, and

fabricated low operation voltage OFETs based on the high performance semicrystalline semiconducting polymer pBTTT. Additionally, we provide a comprehensive study of the morphology of pBTTT on patterned molecular gate electrodes. In particular, we demonstrate that by careful control of the AlOx surface roughness and PA-SAM surface modification, molecular terracing can be observed on pBTTT. The OFET performance was evaluated for three types of channel surface chemistries. The overall performance improves for mixed SAMs, whereas full mobilities were observed for ODPA-only devices. The proposed method may prove valuable also for the growth of semiconducting oxides via atomic layer deposition, and indeed for all other chemical methods that rely on the presence of functional groups on gate electrode surfaces.

6 pBTTT nanotransistors with patterned molecular gate dielectrics

In this Chapter, nanoscale organic field effect transistors based on a poly(2,5-bis(3-alkylthiophen-2-yl)thieno[3,2-b]thiophene (pBTTT) are demonstrated with patterned metal gate electrodes and ultrathin gate dielectrics based on self-assembled monolayers. Owing to the high capacitance of this hybrid dielectric, we were able to operate pBTTT transistors at very low input voltages (<3V), together with very low leakage currents (<5pA) and high on/off ratios ($\sim 10^3$). Additionally, we demonstrate that by optimizing the atomic force microscopy imaging process of pBTTT films, one can reveal the morphology of the nanoscale crystallites. We find a twofold increase of the pBTTT crystallite diameter compared to previous literature values.

6.1 Introduction

Semicrystalline semiconducting polymers are subject of intense research in recent years. As already introduced in Chapter 5, one important example of this class of materials is poly(2,5-bis(3-alkylthiophen-2-yl)thieno[3,2-b]thiophene (pBTTT). This organic semiconductor has demonstrated excellent performance, achieving benchmark mobilities in excess of $\sim 1 \mathrm{cm^2 V^{-1} s^{-1}}$ [151]. The high hole mobility observed is explained in terms of the large degree of crystallinity of pBTTT, and the preferential orientation of the polymer backbone parallel to gate dielectrics with low surface energy.[32] Atomic force microscopy (AFM) studies of pBTTT showed that upon annealing and careful control of surface chemistry and roughness, micrometer-sized terraced domains can be formed.[156] Later, it has been shown that these large terraces are not composed of single crystalline lamella, but consist of smaller subunits on the order of $\sim 10 \mathrm{nm}$. In light of that, the charge transport in pBTTT was understood to result from multiple length scales – fast charge displacement within the small crystallites, and slower for larger lengths. Indeed, by inputing this structural information in Mobility Edge calculations, Wang et al.[170] estimate charge carrier mobilities as high as $\sim 20 \mathrm{cm^2 V^{-1} s^{-1}}$

within these nm-sized, high-quality crystallites. Therefore, the charge transport in extended pBTTT films can be thought to be limited by energetic and morphological disorder at the boundaries between adjacent crystallites[171], which largely limit the observed carrier mobility.

In this chapter we demonstrate that by a simple optimization of atomic force microscopy imaging process, one can directly observe the pBTTT crystallites. In contrast to previous transmission electron microscopy (TEM) study[170], we obtain a larger average grain diameter ($\sim$23nm). We argue that this discrepancy originates from the potential underestimation of grain size obtained by TEM, since a transmission image is comprised of a superposition of grain boundaries of several pBTTT lamellas. This finding is interesting since device fabrication at this length scale can be easily achieved via standard electron beam lithography. In fact, one can envision sub-30nm junctions in which a few pBTTT crystallites are positioned in the transistors channel, and potentially exploit its full carrier mobility. However, highly scaled channel lengths in OFETs results in several short-channel effects[172] that drastically degrades device performance. Among them, one important requirement for channel length scaling in OFETs is the concomitant reduction of the gate dielectric thickness. Here we present pBTTT organic field effect transistors OFETs at sub-100nm length scales with patterned, ultra-thin molecular-based gate dielectrics ($\sim$5nm). This reduced thickness enhances the capacitive coupling between the gate and the organic semiconductor, thus improving I_{ds} modulation and allowing operation at much lower voltages. In our devices, we employ side guarding electrodes to probe exclusively the pBTTT response at the nanoscale gaps. We present devices with channel lengths comparable to the pBTTT crystallite dimensions (20-30nm). At this scale, highly mobile charge carriers can flow along the π-stacking and the π-conjugated backbone directions, without being relayed through amorphous grain boundary regions. Nanotransistors based on pBTTT have been previously reported in the literature for unpatterned back-gates with thick SiO_2 dielectrics[173]. However, in this report no attempt has been made to hinder fringe currents – therefore, masking the true electrical response of pBTTT crystallites.[174]

6.2 Sample Preparation

Two transistors types were developed for this study – one with thick SiO_2 dielectric functionalized with octadecyltrichlorosilane (OTS), and the other with AlOx functionalized with mixed-type phosphonic acid self-assembled monolayers (PA-SAM). For the transistors based on SiO_2, the underlying doped Si was used as global gate, whereas

for transistors with patterned gate electrodes the Si/SiO$_2$ served only as substrate. Both transistors were fabricated using bottom-gate, bottom-contact geometry (BGBC). Source (S), drain (D), guard, and Al gate electrodes ($\sim$20nm thick) were defined with the PMGI/PMMA double layer resist and electron beam lithography, as described in Section 3.2. Aluminum electrodes were deposited via thermal evaporation with high evaporation rates ($\sim$20nm.s^{-1}) in order to reduce surface roughness, as described in Chapter 3, Section 3.3. At these rates, we obtained smooth surfaces with root-mean-square roughness Rq$\approx$0.6nm. Surface roughness measurements were performed by AFM over areas of 2x2μm^2.

The gate dielectrics of the pattern electrodes consisted of AlOx functionalized with mixed-type phosphonic acid self assembled monolayers, as introduced in Chapter 5. Aluminum structures were treated in a low-energy O$_2$ plasma system to increase the AlOx thickness and enhance the density of hydroxyl groups. The substrates were then immersed for 1h into a 2-propanol solution of octadecylphosphonic acid mixed with 16-phosphonohexadecanoic acid (PHDA:ODPA (1:1), 1mM). Samples were removed from solution, rinsed, dried in a stream of N$_2$, and shortly baked at 65°C. Afterwards, the substrates were re-immersed into an ODPA solution for 15h to heal the SAMs defects. The assembly is terminated, and a highly insulating SAM is formed with sufficient surface energy for subsequent solution processing.[1] S/D and guard electrodes consisted of electron-beam deposited titanium (Ti, 0.3nm thick), and thermally-evaporated gold (Au, 35nm thick) multilayer. The finished devices were treated in oxygen plasma to remove the PHDA:ODPA SAM, and pure ODPA monolayer was assembled to obtain low surface energy at the transistors channel. Devices were then transferred to a N$_2$ glove-box ($<$0.1ppm O_2 and $<$0.1ppm H_2O), and pBTTT was spin-coated from a 1,2-dichlorobenzene solution (0.25%$_{wt.}$ at 65°C). Excess solvent was removed at 120°C for 5min, followed by thermal annealing at 180°C to induce crystallization of pBTTT.

6.3 pBTTT nanotransistors with SiO$_2$-OTS dielectrics

In Figure 6.1 we evaluate interaction of the pBTTT thin-films deposited on SiO$_2$-OTS gate dielectric with the Ti/Au nanoelectrodes. The atomic force microscopy image (Figure 6.1(a)) depicts the device junction (W=100, L=65nm), and the guard electrodes. Note that the morphological characterization was only performed after the device was fully characterized, since air exposure can degrade and disturb the electrical measurements. The well-known pBTTT molecular terraces are observed for this an-

---

[1]For further details on this mixed SAM assembly please refer to Ref. [175] or Section 5.2.
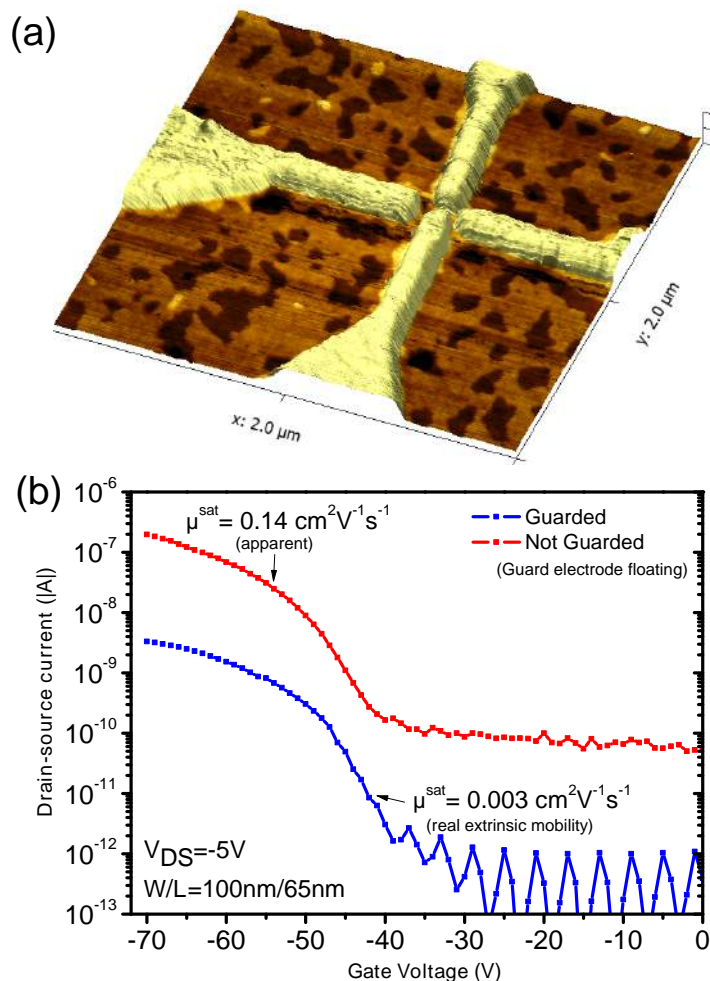
Figure 6.1: (a) Three-dimensional atomic force microscopy (AFM) topography image of pBTTT nanotransistor with Si back-gate, and SiO_2-OTS gate dielectrics. (b) Transfer curves for the transistor with (blue) and without (red) guard electrode bias.

nealed device, with no observable morphological disruption induced by the electrodes. This result is in contrast to the observations of Noh *et al.*[176], wherein they report the degradation of pBTTT domain order caused by bare Au electrodes upon annealing at 170°C. For our experiments we used a pBTTT with long alkyl side chains (C16) annealed at 180°C. We believe that the higher temperature employed in our annealing process may facilitate the reorganization of pBTTT. Another interesting observation made with these nanojunctions was that all devices with smaller channel lengths (L=20nm or 25nm) showed negligible S/D currents, nor field-effect modulation. We speculate that due to the strong tendency to form molecular terraces, pBTTT crystallites may be expelled from confined channel areas during annealing. This indicates existence of a minimal channel length for which spin-coated pBTTT OFETs can be fabricated, which is evidenced by the fact that working devices were only obtained for

channel lengths L≥30nm.

The Guard Electrode Effect

The transfer characteristics of the device are represented in Figure 6.1(b). Non-guarded transistors (red) showed large off-currents (∼100pA), on-off current ratio of ∼10^3, and high saturation mobilities (0.14cm^{2}V^{-1}s^{-1}). The calculated mobility is comparable to values reported previously in the literature for long-channel pBTTT transistors.[161] However, when the same junction is measured using the guard electrodes the I$_{DS}$ is drastically reduced due to fringe current suppression (blue curve, Figure 6.1). As a result, the extrinsic field-effect mobility is reduced to μ =0.003cm^{2}V^{-1}s^{-1}. This result is more realistic since highly scaled OFETs suffers from short-channel effects that strongly degrades device performance.[172]

6.3.1 pBTTT nanocrystallites size distribution

The morphology of high-performance semicrystalline semiconducting polymers is thought to be composed of aggregates of highly ordered π-stacked lamellas, co-existing with disordered amorphous regions[177]. High degree of delocalization is expected within its crystallites, whereas long-range carrier transport is achieved with π-conjugated polymer chains interconnecting ordered regions through the amorphous ones. Therefore, the efficiency to which charge carriers are bridged from/to regions of high delocalization can limit semiconductors performance. Indeed, it has been recently found that polymers with high rigidity backbone can efficiently induce the formation of a network of pathways for charge transport, even with an apparent low crystallinity.[150] For pBTTT, this morphology has been previously observed by TEM, wherein the crystallite average diameter was estimated to be ≈10nm.[170]

Here we employ a very sharp silicon AFM tip (apex radius better than 2nm, Nanosensors SSS-NCH) to directly observe pBTTT aggregates on annealed thin films, as seen in Figure 6.2(a). The AFM imaging process was performed in tapping-mode with slightly high set-point, in order to improve grain boundaries details. The resulting image was segmented with standard watershed algorithm[2], and the distribution of equivalent diameters is plotted in Figure 6.2(b). In contrast to the previous TEM study, we obtained a larger average diameter of D$_{eq}$≈23nm. For this comparison we use a polymer of similar molecular weight (chain extended length of 65-68nm), and a similar thermal annealing

---

[2]The analysis was performed using GWYDDION, an open-source software for scanning probe microscopy data analysis.[178]
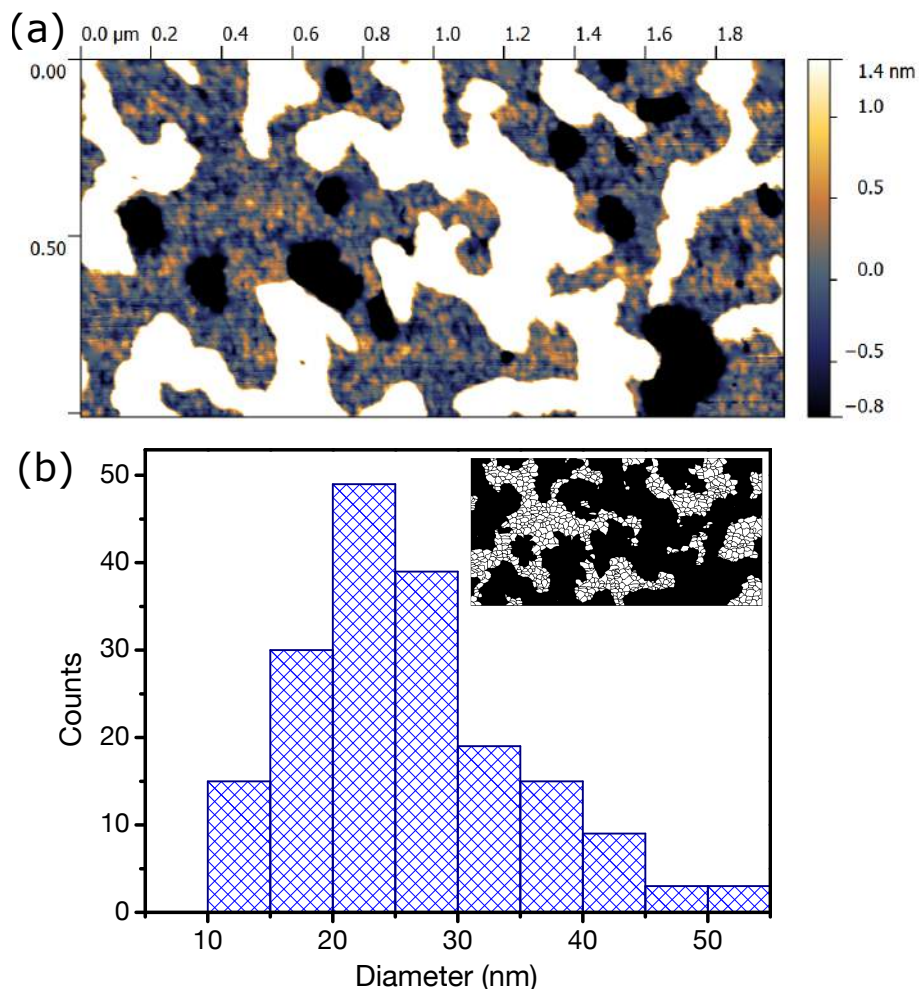
Figure 6.2: pBTTT morphological analysis. (a) Atomic force microscopy topography image of pBTTT on SiO_2-OTS, annealed at 185°C. Color scale is adjusted to one terrace level to facilitate observation of the crystallites. (b) The same image was segmented with watershed algorithm – the resulting binary image of grain boundaries is shown in the inset. The histogram displays the distribution of pBTTT grain diameters.

procedure as used in Ref.[170]. We believe that using TEM to evaluate the pBTTT crystallite inherently underestimates the measured sizes. TEM image is a result of the superposition of a few levels of pBTTT terraces, which is composed of several crystallites. Since the distribution of crystallite boundary is stochastic, no boundary vertical alignment from neighboring terraces is expected, complicating size distribution estimation. In our AFM analysis only the grains at the surface are evaluated, resulting therefore in a accurate distribution of grain sizes of the pBTTT thin film. It is interesting to note that we have only been able to detect these grains with the sharp AFM tip, whereas conventional AFM tips did not reveal any grain boundary (several images can be seen in Sections 5.3.1 and 5.3.2 for comparison).

6.4 pBTTT FET with patterned gate electrodes

Devices with global back-gating and thick SiO_2 dielectrics operate at high supply voltages and cannot be scaled into large-area organic circuits. Patterned metal gate electrodes allows addressing individual transistor junctions at very low voltages, with potential for applications in the manufacture of integrated organic circuitry. An exemplary transistor based on patterned Al gate electrodes is shown in Figure 6.3(a). The contact geometry was similar to the devices fabricated with global silicon back-gate. Any fringe current emanating from source electrode is effectively blocked by the guard electrodes. Therefore, the measured electrical response is truly from the pBTTT crystallites confined to $WxL=120x30nm^2$ channel area. Transfer and output characteristics of the transistor are shown in Figure 6.3(b,c). Owing to the large areal capacitance of the molecular gate dielectric $(0.75\mu Fcm^2)$, the transistor is operated at relatively small voltages ($V_{DS} \leq$-2.5V, $V_G \leq$-3V). The on-off current ratio ($\sim 7x10^2$) has decreased slightly as compared to devices with thick SiO_2 dielectric. The degradation in current modulation is caused by an increase of drain off-current for devices with AlOx/PA-SAMs dielectrics. The off-current increase can be also attributed to the increased electric field strength in these junctions, since channel length is reduced by two times (L=30nm). On the other hand, the AlOx dielectric for these devices were produced with low-energy O_2 plasma, which is known to form lower quality oxides.[179] Therefore, current leakage from source to drain electrode through the AlOx/PA-SAM may also negatively impact the off-state currents. Non-linearities at low drain-source voltages are observed in the output curves. This indicates that device response is strongly influenced by contact resistance at the Au/pBTTT interface. Indeed, when contact resistance is estimated using transmission line method with long-channel devices (not shown), we obtain R_C=10-20kΩcm. However, these values are unrealistic since it would result in device series resistances that are significantly higher than what is measured in device shown in Figure 6.3. We argue that this discrepancy may be caused by the energy barrier lowering at the Au/pBTTT interface induced by source-drain electric fields. Unfortunately, the uncertainty in contact resistance estimation precludes any attempt of reliably extracting the intrinsic carrier mobility of pBTTT crystallites.

We obtain an extrinsic field effect mobility of μ =0.0045cm^{2}V^{-1}s^{-1} in the saturation regime, which is of comparable magnitude with devices produced with silicon back-gate. Despite the low mobilities extracted on the nanoscale transistors, one can speculate that the intrinsic pBTTT mobility may be substantially higher since channel resistance is only a very small fraction of total device resistance. Improvements in performance should be achieved by employing top contact electrodes.[180, 181] However, fabrication
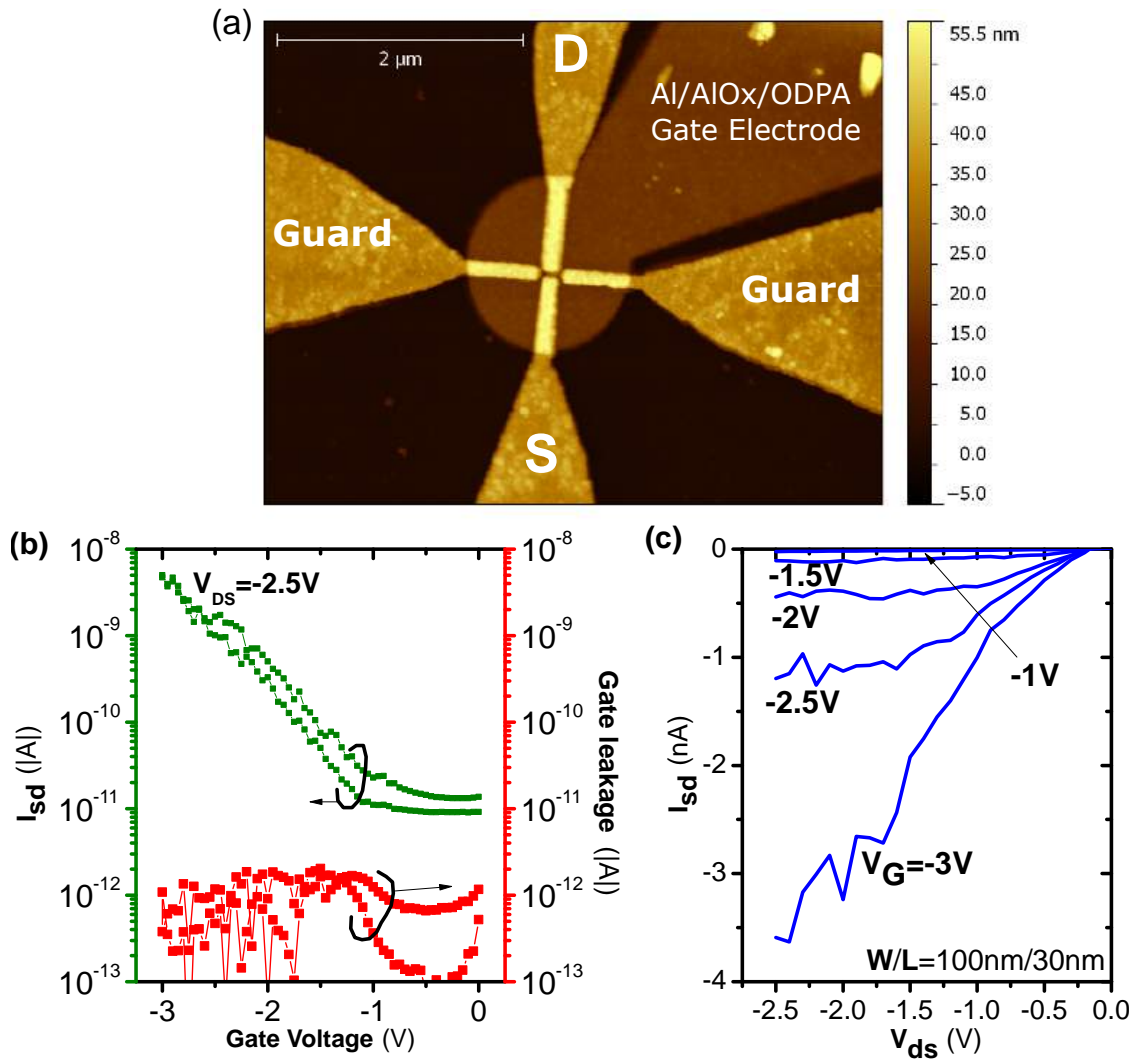
Figure 6.3: (a) Atomic Force Microscopy (AFM) image of the pBTTT nanotransistors with hybrid gate dielectrics. Source (S), drain (D), and guard electrodes meet at the Al/AlOx/ODPA gate electrode to form a 45nm junction. Transfer (b), and output (c) characteristics of the pBTTT low-voltage ($V_{DS} \leq$-2.5V, $V_G \leq$-3V) nanoscale transistor with L≈30nm and W≈120nm.

of polymer-based transistors with sub-50nm channel length using top-contact configuration is very challenging due to incompatibility with solvents used in lithography. Nevertheless, the use of bottom electrodes with devices operating at low voltages may find interest in other research areas, such as organic spintronics[110]. Spin injection in organic semiconductors is known to take place only at low voltage biases (<1V), in devices with intentionally high contact resistances (tunneling barriers). Due to the high capacitive coupling obtained with AlOx/PA-SAM dielectrics, this operation condition can be easily achievable.

6.5 Conclusions

In summary, we show the manufacturing process of pBTTT field effect transistors operating at low voltages with a patterned molecular-based gate electrodes and channel lengths scaled to the dimensions of a single crystallite of pBTTT. Moreover, we demonstrate that by a simple optimization of the AFM imaging process, one can directly observe the pBTTT aggregate and evaluate its distribution. We found that the grain average diameter is two times larger than previously reported values (D≈23nm). By employing side guard electrodes and scaled channel length, we obtain the charge transport characteristics of pBTTT at these very confined areas. In spite of the aggressively scaled channel and high contact resistances, we obtain a high field effect modulation (10^3) and extrinsic field effect mobilities of $\mu = 0.0045 \text{cm}^2 \text{V}^{-1} \text{s}^{-1}$.

7 Summary and Outlook

Polythiophene-based organic electronic devices with nanoscale lateral dimensions have been fabricated and analyzed. Two classes of devices were investigated, namely organic spin-valves and field-effect transistors, with highly-conducting and liquid crystalline organic semiconductors (OSCs), respectively. These hybrid organic-inorganic devices draw substantial attention because of the opportunity of combining properties of each material class, and additionally exploiting new functionalities arising from their combination. To that end, the materials and devices studied here were explored with a wide scope.

In the first part of the thesis, important questions of organic spintronics have been addressed. In particular, the possibility of detecting spin-polarized charge transport OSCs in well-defined lateral spin-valves has been investigated. This elusive observation constitutes an open question of paramount importance, since it would allow unambiguous proof of long-range spin transport in OSCs. Several steps toward that goal were shown. Firstly, the use of highly conducting, namely PEDOT:PSS, instead of pristine semiconducting organic material for lateral spin-valve integration has been proposed and demonstrated. Organic conductors offer the unique advantage of high bulk conductivity, due to charge carriers generated through chemical doping. Since high-quality spin-polarized electrodes can only be obtained in a *bottom contact* device configuration, the availability of bulk charge carriers offers the opportunity of generating spin currents from the electrode's top surface that can be well controlled. Laterally patterned devices with bottom contacts prevent any source of damage to the organic film, such as strong radiation or interaction with incompatible solvents. Moreover, it completely eliminates the problematic issue of interfacial metal diffusion from top electrodes of vertically stacked spin-valves.

Charge transport studies of PEDOT:PSS films with ohmic and spin-polarized tunnel contacts at nanoscale lateral dimensions were shown. Measurements with ohmic nanoelectrodes demonstrated that the conductivity of PEDOT:PSS enhances non-linearly with the reduction of the electrode separations at sub-micrometer scales. This previously unreported scaling effect is a characteristic feature of hopping charge transport

in highly disordered systems, which, in this particular case, was revealed when the device's lateral dimensions approached the spatial extent of the carriers' wavefunction localization (induced by disorder).

The integration of traditional NiFe/AlO$_x$ spin-polarized tunnel electrodes with PE-DOT:PSS was demonstrated by controlling the polymer solution acidity to a level within the tolerances of the metal oxide tunnel barrier (pH=4). Temperature-dependent electrical measurements of the resulting NiFe/AlO$_x$/PEDOT:PSS/AlO$_x$/NiFe lateral structures allowed to confirm the integrity of the tunnel barrier. This procedure is not limited to the NiFe/AlO$_x$/PEDOT:PSS system, but may be extended to other conducting polymers and FM metal electrodes. Following this approach, spin transport properties of PEDOT:PSS were analysed. No measurable MR signal in our NiFe/AlO$_x$/-PEDOT:PSS/AlO$_x$/NiFe lateral spin valve structures were observed, which was correlated with the high resistance-area products obtained with the AlO$_x$ tunneling barriers (10^{-7} to $10^{-4}\Omega m^2$). The agreement with theoretical predictions suggested the use of a rather lower interfacial resistance between PEDOT:PSS and NiFe to transform spin information into significant MR electrical signals. In the following, device modelling was used to describe the behaviour of the PEDOT:PSS spin-valves. By applying the experimental data obtained with the devices, an upper limit for the spin lifetime ($\tau_{sf} < 50ns$) was established, which is an invaluable material input for future investigations.

Future studies may be focused on the search of alternative materials to engineer the FM/OSC interface, delivering low tunneling energy barrier, high spin-asymmetry coefficient, and sufficient chemical inertness to allow the integration with conducting polymers. The need of tailored interface resistances in organic spintronic devices was further corroborated by a recent study, wherein spin-polarized current was injected in PEDOT:PSS by a spin-pumping technique, which circumvents the impedance mismatch problem.[182] Alternatively, novel device processing methods could be devised, wherein the organic conductor is integrated with FM electrodes in a dry state, such as thin-film transfer techniques.[183] Using this technique, other materials or formulations of organic conductors could be used – for instance, polyaniline doped with organic acids that show quasi drude-like transport behaviour,[184] or PEDOT:PSS with hot acid treatment, which shows conductivities as high as 2500 Scm^{-1}[122]. A recent study suggested the use of PEDOT:PSS in highly conductive state for spintronics, since its conduction mechanism takes place almost exclusively via spinless *bipolarons*.[185] However, it is not yet clear if a bipolaronic system would tend to quench the spin accumulation by recombination of spins, or if the absence of spin-1/2 *polarons* would be advantageous due to a reduction of paramagnetic scattering centers. To answer these questions, future studies should combine spin-sensitive spectroscopic techniques, such

as electron paramagnetic resonance, with electrical transport measurements. These efforts would also allow a better understanding of spin-spin and spin-lattice relaxation mechanisms with its relation to spin lifetime and long range transport in OSC.

In the second part of this thesis, pBTTT OFETs with patterned gate electrodes operating at voltages as low as 3V were studied. Low voltage operation was allowed by ultrathin gate dielectrics based on aluminum oxide (AlOx) and phosphonic-acid-based self-assembled monolayers (PA-SAMs). Firstly, the assembly of carboxylate terminated monolayers on AlOx surfaces was addressed. These monolayers have been known to provide weak insulation properties when compared to high-quality methyl-terminated monolayers. A simple two-step assembly process for mixed monolayers, containing both methyl and carboxylate termination, was presented. This modified process allowed to obtain two orders of magnitude improvement of the leakage current through the thin hybrid dielectric. In fact, this approach allowed to obtain leakage current levels previously observed only with high quality methyl terminated PA-SAMs, in parallel with tunable surface energy due to the mixed nature of the SAM. The observations strongly suggested that the anchoring of carboxylate-terminated molecules on AlOx surfaces is not given exclusively via the PA terminal groups, which explains their inferior insulating performance. Furthermore, a comprehensive study of the morphology of pBTTT on the mixed SAMs with various fractions of carboxylate-termination was shown. In particular, it has been demonstrated that, by carefully controlling the aluminum electrode surface roughness and the PHDA content of the monolayers, molecular terracing can be observed on pBTTT. The OFET electrical performance was evaluated for three types of channel surface chemistries. Very high performance improvement has been observed for mixed SAMs, compared with SAMs based on carboxylate-terminated molecules, whereas full mobilities were observed only for devices with pure methyl-terminated dielectrics.

The success obtained with mixed SAMs for OFETs motivated further investigation. Taking advantage of the solution processability imparted by these monolayers, nanoscale field-effect transistors with channel lengths scaled to the dimensions of a single crystallite of pBTTT were studied. In order to confirm the size distribution of pBTTT crystallites, a careful atomic force microscopy analysis was conducted. This allowed direct observation of the pBTTT crystallite size distribution. We found that the average diameter of the crystallites (D≈23nm) was two times larger than previously reported. OFETs were fabricated with channel lengths on this length scale. In addition to source and drain electrodes, guard electrodes to hinder fringe currents were laid out, which allowed to study the electrical response of the device with only a few pBTTT crystallites. In spite of the aggressively scaled channel lengths and high contact resistances

(due to bottom-contact configuration), high field-effect modulations ($\sim 10^3$) and extrinsic field effect mobilities of $0.0045 \text{cm}^2\text{V}^{-1}\text{s}^{-1}$ were obtained. These results constitute the first report of a pBTTT nanotransistor operating at voltages <3V, concurrently with extremely low leakage-currents.

The development of functional elements for electronic devices, such as ultra-thin dielectrics presented here, is very important. These may allow operation of organic electronic devices at very low power consumption and low production costs, which are ultimately the bottleneck of many emerging technologies. The proposed hybrid gate dielectrics may also prove valuable for other classes of semiconductors. The presence of functional groups at the gate electrode surface unequivocally allows the growth of semiconducting oxides via low-temperature atomic layer deposition, e.g. zinc oxide. [186]. In fact, the method can be extended to any other chemical methods that rely on the presence of functional groups on the SAMs. For example, phosphonic-acid SAMs grown on LSMO has been already demonstrated as spin-polarized tunnel barriers[187], and electrochemically deposited ferromagnetic metals has been shown to result in good quality organic spin-valves[188]. One could envision utilizing simpler methods to exploit the presence of functional groups at the SAM surface. For instance, electroless deposition of elemental ferromagnetic metals could be used in conjunction with the mixed monolayers[189, 190], allowing the fabrication of organic-based TMR junctions almost entirely from solution methods.

Acknowledgements

Several people have made contributions that led to the completion of this PhD thesis. First and foremost, I would like to thank my PhD supervisors Alexander M. Bittner & Luis E. Hueso for the opportunity to perform this project in CIC nanoGUNE, the interest in embarking in a highly multidisciplinary and challenging work, and the continuous support and guidance over the last years.

I am also most thankful for the help and fruitful discussions within our group: José M. Alonso, Abid A. Khan, Wiwat Nuansing, Marcin Ł. Górzny, Sven Degenhard, Charllote Stenner, Amaia Rebollo, Monika Goikoetxea, Aitziber Eleta – Thank You!

Several people must be acknowledge for the engagement in collaboration in scientific or in a technical level: Marco Gobbi, Amilcar Bedoya-Pinto, Xiangnan Sun, José M. Porro, Fan Yang, Roger Llopis, Federico Golmar, Nicolò Macaferri, Libe Arzubiaga, Felix Casanova, Emmanouil Masourakis, Estitxu Villamor, Mato Knez, Paolo Vavassori, Keith Gregorczyk, Sergei Ponomarenko, Josetxo Pomposo, Miren Isasa, Celso P. Fernandes. Also a big thanks to Gorka Pazos and Ralph Gay for keep everything running smoothly in the clean-room.

A PhD thesis span over several years, and I am very grateful for the friendship/love/support of many people in San-Sebastián. They made a great job in keeping my work/life balance from diverging, for which I am most thankful. Jon Romero, David Escobar, Matthew Cowburn, Katerine Yiannibas, Itziar Mendigutxia, Iñigo Perez, Raul Zazpe, Paulo Sarriugarte, Lorenzo Fallarino, Jon Ander, Xabier Osorio, Amaia Alaya, Gabriella Portella, Alberto Lopez – Thank You! A few names mentioned above should be in this list as well, but I won't mention twice.

Também agradeço aos meus páis e irmãos – Marcos de Oliveira, Fabrízio Glória, Lorraine Glória, Vanja M. Glória –, que me deram contínuo suporte/amor/carinho desde a primeira vez que sai da pátria amada. Muita saudade de vocês e do Brasil. And to conclude, a special thanks to my beloved wife, Anastasia de Oliveira, a gift given by this city, who had a lot of endurance and patience with this line of work that consumes all the time of the world.

List of Publications

Publications covered in this thesis

Chapter 4

Charge and Spin Transport in PEDOT:PSS Nanoscale Lateral Devices
TVAG de Oliveira, M Gobbi, JM Porro, LE Hueso, AM Bittner
Nanotechnology **24**, 475201 (2013)

Chapter 5

Mixed Self-Assembled Monolayer Gate Dielectrics for Low-Voltage Solution-Processed Polymer Field-Effect Transistors
TVAG de Oliveira, AE Lopez, LE Hueso, AM Bittner
submitted (2014)

Chapter 6

Sub-100nm pBTTT Nanotransistors with Self-assembled Monolayer based Gate Dielectrics
TVAG de Oliveira, F Golmar, AC Moreira, CP Fernandes, LE Hueso, AM Bittner
in preparation (2014)

Other publications

Electrospinning of Tetraphenylporphyrin Compounds into Wires
W Nuansing, E Georgilis, **TVAG de Oliveira**, G Charalambidis, A Eleta, AG Coutsolelos, A Mitraki, AM Bittner
Part. Part. Syst. Charact. **31**, 88−93 (2014)

Phase-Sensitive Magneto-Optical Kerr Effect in Plasmonic nanoferromagnets for Label-Free Refractive Index and Molecular Sensing Applications
N Maccaferri, K Gregorczyk, **TVAG De Oliveira**, M Kataja, S van Dijken, Z Pirzadeh, A Dmitriev, M Knez, P Vavassori
in preparation (2014)

Bibliography

[1] K. E. Drexler, *Engines of Creation: The Coming Era of Nanotechnology* (Anchor Press/Doubleday, Garden City, N.Y, 1986).

[2] R. Saini, S. Saini, and S. Sharma, Journal of cutaneous and aesthetic surgery **3**, 32 (2010).

[3] W. Arden, M. Brillouët, P. Cogez, M. Graef, B. Huizing, and R. Mahnkopf, Version **2**, 31 (2010).

[4] R. Friend, R. Gymer, A. Holmes, J. Burroughes, R. Marks, C. Taliani, D. Bradley, D. Santos, J. Bredas, M. Logdlund, Others, D. Dos Santos, and M. Lögdlun, Nature **397**, 121 (1999).

[5] A. Tsumura, H. Koezuka, and T. Ando, Applied Physics Letters **49**, 1210 (1986).

[6] G. Horowitz, Advanced Materials **10**, 365 (1998).

[7] M. Halik, H. Klauk, U. Zschieschang, G. Schmid, C. Dehm, M. Schütz, S. Maisch, F. Effenberger, M. Brunnbauer, and F. Stellacci, Nature **431**, 963 (2004).

[8] K. Buschow, *Concise encyclopedia of magnetic and superconducting materials* (Elsevier Science, 2005).

[9] B. Behin-Aein, D. Datta, S. Salahuddin, and S. Datta, Nature nanotechnology **5**, 266 (2010).

[10] M. Baibich, J. Broto, A. Fert, F. Van Dau, F. Petroff, P. Etienne, G. Creuzet, A. Friederich, and J. Chazelas, Physical Review Letters **61**, 2472 (1988).

[11] C. Chappert, A. Fert, and F. N. Van Dau, Nature materials **6**, 813 (2007).

[12] G. Prinz, Journal of Magnetism and Magnetic Materials **200**, 57 (1999).

[13] S. A. Wolf, D. D. Awschalom, R. A. Buhrman, J. M. Daughton, S. von Molnár, M. L. Roukes, A. Y. Chtchelkanova, and D. M. Treger, Science (New York, N.Y.) **294**, 1488 (2001).

[14] S. Datta and B. Das, Applied Physics Letters **56**, 665 (1990).

[15] V. F. Motsnyi, J. De Boeck, J. Das, W. Van Roy, G. Borghs, E. Goovaerts, and V. I. Safarov, Applied Physics Letters **81**, 265 (2002).

[16] J. Stephens, J. Berezovsky, J. P. McGuire, L. J. Sham, A. C. Gossard, and D. D. Awschalom, Physical Review Letters **93** (2004), 10.1103/PhysRevLett.93.097602.

[17] X. Lou, C. Adelmann, M. Furis, S. Crooker, C. Palmstrø m, and P. Crowell, Physical Review Letters **96** (2006), 10.1103/PhysRevLett.96.176603.

[18] I. Appelbaum, B. Huang, and D. J. Monsma, Nature **447**, 295 (2007).

[19] B. T. Jonker, G. Kioseoglou, A. T. Hanbicki, C. H. Li, and P. E. Thompson, Nature Physics **3**, 542 (2007).

[20] V. A. Dediu, L. E. Hueso, I. Bergenti, and C. Taliani, Nature Materials **8**, 707 (2009).

[21] T. D. Nguyen, G. Hukic-Markosian, F. Wang, L. Wojcik, X.-G. Li, E. Ehrenfreund, and Z. V. Vardeny, Nature materials **9**, 345 (2010).

[22] Z. Bao and J. J. Locklin, *Advanced Materials*, Vol. 10 (CRC Press, 2007) p. 640.

[23] J. Shim, K. Raman, Y. Park, T. Santos, G. Miao, B. Satpati, and J. Moodera, Physical Review Letters **100** (2008), 10.1103/PhysRevLett.100.226603.

[24] C. W. Scherr, The Journal of Chemical Physics **21**, 1582 (1953).

[25] H. Shirakawa, E. J. Louis, A. G. MacDiarmid, C. K. Chiang, and A. J. Heeger, Journal of the Chemical Society, Chemical Communications , 578 (1977).

[26] A. Heeger, Reviews of Modern Physics **73**, 681 (2001).

[27] A. MacDiarmid, Reviews of Modern Physics **73**, 701 (2001).

[28] A. G. MacDiarmid and A. J. Heeger, Synthetic Metals **1**, 101 (1980).

[29] T. Yamamoto, K. Sanechika, and A. Yamamoto, Journal of Polymer Science: Polymer Letters Edition **18**, 9 (1980).

[30] K.-Y. Jen, G. G. Miller, and R. L. Elsenbaumer, Journal of the Chemical Society, Chemical Communications **5**, 1346 (1986).

[31] T.-A. Chen, X. Wu, and R. D. Rieke, Journal of the American Chemical Society **117**, 233 (1995).

[32] I. McCulloch, M. Heeney, C. Bailey, K. Genevicius, I. Macdonald, M. Shkunov, D. Sparrowe, S. Tierney, R. Wagner, W. Zhang, M. L. Chabinyc, R. J. Kline, M. D. McGehee, and M. F. Toney, Nature Materials **5**, 328 (2006).

[33] S. Rasmussen and M. Pomerantz, in *Handbook of Conducting Polymers*, edited by T. A. Skotheim and J. Reynolds (CRC Press, 2007) 3rd ed., Chap. 12, pp. 12–01.

[34] F. Jonas and L. Schrader, Synthetic Metals **41**, 831 (1991).

[35] G. Heywang and F. Jonas, Advanced Materials **4**, 116 (1992).

[36] P. Blanchard, A. Cravino, and E. Levillain, in *Handbook of Thiophene-Based Materials: Applications in Organic Electronics and Photonics*, edited by I. F. Perepichka and D. F. Perepichka (John Wiley & Sons, Ltd, Chichester, UK, 2009) Chap. 9.

[37] M. Ratner, Nature nanotechnology **8**, 378 (2013).

[38] V. Coropceanu, J. Cornil, D. a. da Silva Filho, Y. Olivier, R. Silbey, and J.-L. Brédas, Chemical reviews **107**, 926 (2007).

[39] O. D. Jurchescu, J. Baas, and T. T. M. Palstra, Applied Physics Letters **84**, 3061 (2004).

[40] P. W. Anderson, Physical Review **109**, 1492 (1958).

[41] A. Miller and E. Abrahams, Physical Review **120**, 745 (1960).

[42] N. Mott, Journal of Non-Crystalline Solids **1**, 1 (1968).

[43] N. F. Mott, Philosophical Magazine **19**, 835 (1969).

[44] N. F. Mott and E. A. Davis, *Electronic processes in non-crystalline materials* (Oxford University Press, 1971).

[45] V. Ambegaokar, B. Halperin, and J. Langer, Physical Review B **4**, 2612 (1971).

[46] S. M. Sze and K. N. Kwok, *Physics of Semiconductor Devices* (John Wiley & Sons, 2006) p. 832.

[47] N. F. Mott, Proceedings of the Royal Society of London. Series A, Mathematical and Physical Sciences **153**, 699 (1936).

[48] C. Zener and R. R. Heikes, Rev. Mod. Phys. **25**, 191 (1953).

[49] C. Chappert, A. Fert, and F. N. V. Dau, Nat. Mater. **6**, 813 (2007).

[50] F. J. Jedema, *Electrical Spin Injection in metallic Mesoscopic Spin Valves*, Phd thesis, Rijksuniversiteit Groningen (2002).

[51] A. F. Andreev, Sov. Phys. JETP **19**, 1228 (1964).

[52] R. Meservey, P. Tedrow, and P. Fulde, Physical Review Letters **25**, 1270 (1970).

[53] P. Tedrow and R. Meservey, Physical Review B **7**, 318 (1973).

[54] A. Anguelouch, A. Gupta, G. Xiao, D. W. Abraham, Y. Ji, S. Ingvarsson, and C. L. Chien, Phys. Rev. B **64**, 180408 (2001).

[55] R. J. Soulen, J. M. Byers, M. S. Osofsky, B. Nadgorny, T. Ambrose, S. F. Cheng, P. R. Broussard, C. T. Tanaka, J. Nowak, J. S. Moodera, A. Barry, and J. M. D. Coey, Science **282**, 85 (1998).

[56] A. Fert, Journal of Magnetism and Magnetic Materials **200**, 338 (1999).

[57] F. J. Jedema, A. Filip, and B. J. van Wees, Nature **410**, 345 (2001).

[58] B. I. R. A. Z. Y. D. V. Hueso L.E., Advanced Materials **19**, 2639 (2007).

[59] T. Valet and A. Fert, Physical Review B **48**, 7099 (1993).

[60] G. Schmidt, D. Ferrand, L. Molenkamp, A. Filip, and B. van Wees, Physical Review B **62**, R4790 (2000).

[61] E. Rashba, Physical Review B **62**, R16267 (2000).

[62] A. Fert and H. Jaffrès, Physical Review B **64**, 1 (2001).

[63] I. H. Campbell, P. S. Davids, D. L. Smith, N. N. Barashkov, and J. P. Ferraris, Applied Physics Letters **72**, 1863 (1998).

[64] H. Zhu, M. Ramsteiner, H. Kostial, M. Wassermeier, H.-P. Schönherr, and K. Ploog, Physical Review Letters **87** (2001), 10.1103/PhysRevLett.87.016601.

[65] G. Schmidt, Journal of Physics D: Applied Physics **38**, R107 (2005).

[66] M. Johnson and R. H. Silsbee, Physical Review Letters **55**, 1790 (1985).

[67] M. Julliere, Physics Letters A (1975).

[68] J. S. Moodera, L. R. Kinder, T. M. Wong, and R. Meservey, Physical Review Letters **74**, 3273 (1995).

[69] T. Miyazaki and N. Tezuka, Journal of Magnetism and Magnetic Materials **139**, 94 (1995).

[70] J. Moodera, J. Nowak, and R. van de Veerdonk, Physical Review Letters **80**, 2941 (1998).

[71] D. Wang and C. Nordman, . . . IEEE Transactions on **40**, 2269 (2004).

[72] H. X. Wei, Q. H. Qin, M. Ma, R. Sharif, and X. F. Han, Journal of Applied Physics **101**, 09B501 (2007).

[73] M. Cinchetti, K. Heimer, J.-P. Wüstenberg, O. Andreyev, M. Bauer, S. Lach, C. Ziegler, Y. Gao, and M. Aeschlimann, Nature materials **8**, 115 (2009).

[74] A. J. Drew, J. Hoppler, L. Schulz, F. L. Pratt, P. Desai, P. Shakya, T. Kreouzis, W. P. Gillin, A. Suter, N. A. Morley, V. K. Malik, A. Dubroka, K. W. Kim, H. Bouyanfif, F. Bourqui, C. Bernhard, R. Scheuermann, G. J. Nieuwenhuys, T. Prokscha, and E. Morenzoni, Nature materials **8**, 109 (2009).

[75] R. Fiederling, M. Keim, G. Reuscher, W. Ossau, G. Schmidt, A. Waag, and L. Molenkamp, Nature **402**, 787 (1999).

[76] V. Dediu, L. E. Hueso, I. Bergenti, A. Riminucci, F. Borgatti, P. Graziosi, C. Newby, F. Casoli, M. De Jong, C. Taliani, and Y. Zhan, Physical Review B **78**, 115203 (2008).

[77] D. Sun, L. Yin, C. Sun, H. Guo, Z. Gai, X.-G. Zhang, T. Z. Ward, Z. Cheng, and J. Shen, Physical Review Letters **104**, 236602 (2010).

[78] Y.-L. Chan, Y.-J. Hung, C.-H. Wang, Y.-C. Lin, C.-Y. Chiu, Y.-L. Lai, H.-T. Chang, C.-H. Lee, Y. J. Hsu, and D. H. Wei, Physical Review Letters **104** (2010), 10.1103/PhysRevLett.104.177204.

[79] R. Lin, F. Wang, J. Rybicki, and M. Wohlgenannt, Physical Review B **81** (2010), 10.1103/PhysRevB.81.195214.

[80] F. Wang, Z. Xiong, D. Wu, J. Shi, and Z. Vardeny, Synthetic Metals **155**, 172 (2005).

[81] W. Xu, G. J. Szulczewski, P. LeClair, I. Navarrete, R. Schad, G. Miao, H. Guo, and A. Gupta, Applied Physics Letters **90**, 072506 (2007).

[82] Z. H. Xiong, D. Wu, Z. V. Vardeny, and J. Shi, Nature **427**, 821 (2004).

[83] S. Pramanik, C.-G. Stefanita, S. Patibandla, S. Bandyopadhyay, K. Garre, N. Harth, and M. Cahay, Nature nanotechnology **2**, 216 (2007).

[84] N. A. Morley, A. Rao, D. Dhandapani, M. R. J. Gibbs, M. Grell, and T. Richardson, Journal of Applied Physics **103**, 07F306 (2008).

[85] Y. Liu, S. Watson, T. Lee, J. Gorham, H. Katz, J. Borchers, H. Fairbrother, and D. Reich, Physical Review B **79** (2009), 10.1103/PhysRevB.79.075312.

[86] J.-W. Yoo, H. Jang, V. Prigodin, C. Kao, C. Eom, and a.J. Epstein, Synthetic Metals **160**, 216 (2010).

[87] H. Vinzelberg, J. Schumann, D. Elefant, R. B. Gangineni, J. Thomas, and B. BuÌĹchner, Journal of Applied Physics **103**, 093720 (2008).

[88] M. Jagadeesh, S. Tiffany, and R. Karthik, in *Organic Spintronics* (CRC Press, 2010) pp. 1–29.

[89] M. M. M. F. C. T. C. B. S. Dediu V., Solid State Communications **122**, 181 (2002).

[90] E. H. Huisman, *Towards Spin Injection in Pentacene Thin Films*, Master thesis, Rijksuniversiteit Groningen (2005).

[91] M. Michelfeit, G. Schmidt, J. Geurts, and L. W. Molenkamp, physica status solidi (a) **205**, 656 (2008).

[92] W. Naber, M. Craciun, J. Lemmens, A. Arkenbout, T. Palstra, A. Morpurgo, and W. van der Wiel, Organic Electronics **11**, 743 (2010).

[93] C. Vieu, F. Carcenac, A. Pépin, Y. Chen, M. Mejias, A. Lebib, L. Manin-Ferlazzo, L. Couraud, and H. Launois, Applied Surface Science **164**, 111 (2000).

[94] A. N. Broers, J. M. E. Harper, and W. W. Molzen, Applied Physics Letters **33**, 392 (1978).

[95] W. Chen and H. Ahmed, Applied Physics Letters **62**, 1499 (1993).

[96] G. Bernstein, K. Sarveswaran, and M. Lieberman, in *2003 Third IEEE Conference on Nanotechnology, 2003. IEEE-NANO 2003.*, Vol. 2 (IEEE, 2003) pp. 602–605.

[97] Y. CHEN, Microelectronic Engineering **73-74**, 278 (2004).

[98] B. Cord, C. Dames, K. K. Berggren, and J. Aumentado, Journal of Vacuum Science & Technology B: Microelectronics and Nanometer Structures **24**, 3139 (2006).

[99] M. Manheller, S. Trellenkamp, R. Waser, and S. Karthäuser, Nanotechnology **23**, 125302 (2012).

[100] M. W. Knight, L. Liu, Y. Wang, L. Brown, S. Mukherjee, N. S. King, H. O. Everitt, P. Nordlander, and N. J. Halas, Nano letters **12**, 6000 (2012).

[101] S. Valenzuela, D. Monsma, C. Marcus, V. Narayanamurti, and M. Tinkham, Physical Review Letters **94**, 196601 (2005).

[102] S. Maekawa and U. Gafvert, Magnetics, IEEE Transactions on **M**, 0 (1982).

[103] J. S. Moodera, E. F. Gallagher, K. Robinson, and J. Nowak, Applied Physics Letters **70**, 3050 (1997).

[104] M. Grobosch, C. Schmidt, W. Naber, W. van der Wiel, and M. Knupfer, Synthetic Metals **160**, 238 (2010).

[105] D. J. D. Moet, P. de Bruyn, and P. W. M. Blom, Applied Physics Letters **96**, 153504 (2010).

[106] F. Casanova, A. Sharoni, M. Erekhinsky, and I. Schuller, Physical Review B **79**, 1 (2009).

[107] W. J. Baker, K. Ambal, D. P. Waters, R. Baarda, H. Morishita, K. van Schooten, D. R. McCamey, J. M. Lupton, and C. Boehme, Nature Communications **3**, 898 (2012).

[108] T. D. Nguyen, E. Ehrenfreund, and Z. V. Vardeny, Science (New York, N.Y.) **337**, 204 (2012).

[109] W. J. M. Naber, S. Faez, and W. G. Van Der Wiel, Journal of Physics D: Applied Physics **40**, R205 (2007).

[110] V. A. Dediu, L. E. Hueso, I. Bergenti, and C. Taliani, Nature materials **8**, 707 (2009).

[111] C. Barraud, P. Seneor, R. Mattana, S. Fusil, K. Bouzehouane, C. Deranlot, P. Graziosi, L. Hueso, I. Bergenti, V. Dediu, F. Petroff, and A. Fert, Nature Physics **6**, 615 (2010).

[112] T. Santos, J. Lee, P. Migdal, I. Lekshmi, B. Satpati, and J. Moodera, Physical Review Letters **98**, 3 (2007).

[113] J. Schoonus, P. Lumens, W. Wagemans, J. Kohlhepp, P. Bobbert, H. Swagten, and B. Koopmans, Physical Review Letters **103**, 1 (2009).

[114] M. Gobbi, F. Golmar, R. Llopis, F. Casanova, and L. E. Hueso, Advanced Materials **23**, 1609 (2011).

[115] T. L. A. Tran, T. Q. Le, J. G. M. Sanderink, W. G. van der Wiel, and M. P. de Jong, Advanced Functional Materials **22**, 1180 (2012).

[116] C.-Y. Liu, H. AlQahtani, M. Grell, D. Allwood, M. Gibbs, and N. Morley, Synthetic Metals **173**, 51 (2013).

[117] J. Rybicki, R. Lin, F. Wang, M. Wohlgenannt, C. He, T. Sanders, and Y. Suzuki, Physical Review Letters **109**, 1 (2012).

[118] J. S. Moodera, T. S. Santos, and K. V. Raman, in *Organic Spintronics*, edited by Z. V. Vardeny (CRC Press, 2010) pp. 1–29.

[119] T. Ikegami, I. Kawayama, M. Tonouchi, S. Nakao, Y. Yamashita, and H. Tada, Applied Physics Letters **92**, 153304 (2008).

[120] Y. Kawasugi, M. Ara, H. Ushirokita, T. Kamiya, and H. Tada, Organic Electronics **14**, 1 (2013).

[121] Y. H. Kim, C. Sachse, M. L. Machala, C. May, L. Müller-Meskamp, and K. Leo, Advanced Functional Materials **21**, 1076 (2011).

[122] Y. Xia, K. Sun, and J. Ouyang, Advanced Materials (Deerfield Beach, Fla.) **24**, 2436 (2012).

[123] K. Wefers and C. Misra, *Oxides and Hydroxides of Aluminum*, Tech. Rep. (ALCOA Laboratories, 1987).

[124] J. Kim, J. Jung, D. Lee, and J. Joo, Synthetic Metals **126**, 311 (2002).

[125] A. J. Kronemeijer, E. Huisman, I. Katsouras, P. van Hal, T. Geuns, P. Blom, S. van der Molen, and D. de Leeuw, Physical Review Letters **105**, 1 (2010).

[126] A. N. Aleshin, S. R. Williams, and A. J. Heeger, Synthetic Metals **94**, 173 (1998).

[127] J. Ouyang, Q. Xu, C.-W. Chu, Y. Yang, G. Li, and J. Shinar, Polymer **45**, 8443 (2004).

[128] M. Vosgueritchian, D. J. Lipomi, and Z. Bao, Advanced Functional Materials **22**, 421 (2012).

[129] A. M. Nardes, M. Kemerink, R. A. J. Janssen, J. A. M. Bastiaansen, N. M. M. Kiggen, B. M. W. Langeveld, A. J. J. M. van Breemen, and M. M. de Kok, Advanced Materials **19**, 1196 (2007).

[130] U. Lang, E. Müller, N. Naujoks, and J. Dual, Advanced Functional Materials **19**, 1215 (2009).

[131] Y. Xia and J. Ouyang, ACS Applied Materials & Interfaces **4**, 4131 (2012).

[132] K. van de Ruit, R. I. Cohen, D. Bollen, T. van Mol, R. Yerushalmi-Rozen, R. A. J. Janssen, and M. Kemerink, Advanced Functional Materials , 1 (2013).

[133] A. M. Nardes, M. Kemerink, and R. Janssen, Physical Review B **76**, 085208 (2007).

[134] N. Mott, Reviews of Modern Physics **50**, 203 (1978).

[135] A. Zabrodskii and K. Zinov'eva, Zh. Eksp. Teor. Fiz **742**, 425 (1984).

[136] A. Bedoya-Pinto, J. Malindretos, M. Roever, D. D. Mai, and A. Rizzi, Physical Review B **80**, 195208 (2009).

[137] B. Shklovskii and A. Efros, *Moscow Izdatel Nauka* (Springer-Verlag, 1979) p. 388.

[138] W. Schoepe, Zeitschrift für Physik B Condensed Matter **455463** (1988).

[139] A. M. Nardes, R. a. J. Janssen, and M. Kemerink, Advanced Functional Materials **18**, 865 (2008).

[140] A. Nardes, *Technische Universiteit Eindhoven*, Phd thesis, Technische Universiteit Eindhoven (2007).

[141] P. Holody, W. Chiang, R. Loloee, J. Bass, W. Pratt, and P. Schroeder, Physical Review B **58**, 12230 (1998).

[142] R. Meservey and P. Tedrow, Physics Reports **238**, 173 (1994).

[143] J. S. Moodera, J. Nassar, and G. Mathon, Annual Review of Materials Science **29**, 381 (1999).

[144] J. Bass and W. Pratt, Journal of magnetism and magnetic materials **200**, 274 (1999).

[145] S. Parkin, C. Kaiser, and A. Panchula, Nature Materials **3**, 2 (2004).

[146] Y. Fukuma, L. Wang, H. Idzuchi, S. Takahashi, S. Maekawa, and Y. Otani, Nature Materials **10**, 527 (2011).

[147] V. I. Krinichnyi, S. D. Chemerisov, and Y. S. Lebedev, Physical Review B **55**, 16233 (1997).

[148] J. Li, Y. Zhao, H. S. Tan, Y. Guo, C.-A. Di, G. Yu, Y. Liu, M. Lin, S. H. Lim, Y. Zhou, H. Su, and B. S. Ong, Scientific Reports **2**, 754 (2012).

[149] W. Zhang, J. Smith, S. E. Watkins, R. Gysel, M. McGehee, A. Salleo, J. Kirkpatrick, S. Ashraf, T. Anthopoulos, M. Heeney, and I. McCulloch, Journal of the American Chemical Society **132**, 11437 (2010).

[150] X. Zhang, H. Bronstein, A. J. Kronemeijer, J. Smith, Y. Kim, R. J. Kline, L. J. Richter, T. D. Anthopoulos, H. Sirringhaus, K. Song, M. Heeney, W. Zhang, I. McCulloch, and D. M. Delongchamp, Nature Communications **4**, 2238 (2013).

[151] B. H. Hamadani, D. J. Gundlach, I. McCulloch, and M. Heeney, Applied Physics Letters **91**, 243512 (2007).

[152] Y. M. Park, J. Daniel, M. Heeney, and A. Salleo, Advanced materials (Deerfield Beach, Fla.) **23**, 971 (2011).

[153] H. Klauk, U. Zschieschang, J. Pflaum, and M. Halik, Nature **445**, 745 (2007).

[154] P. H. WoÌĹbkenberg, J. Ball, F. B. Kooistra, J. C. Hummelen, D. M. de Leeuw, D. D. C. Bradley, and T. D. Anthopoulos, Applied Physics Letters **93**, 013303 (2008).

[155] J. M. Ball, P. H. WoÌĹbkenberg, F. ColleÌĄaux, M. Heeney, J. E. Anthony, I. McCulloch, D. D. C. Bradley, and T. D. Anthopoulos, Applied Physics Letters **95**, 103310 (2009).

[156] R. J. Kline, D. M. DeLongchamp, D. a. Fischer, E. K. Lin, M. Heeney, I. McCulloch, and M. F. Toney, Applied Physics Letters **90**, 062117 (2007).

[157] Y. Jung, R. J. Kline, D. a. Fischer, E. K. Lin, M. Heeney, I. McCulloch, and D. M. DeLongchamp, Advanced Functional Materials **18**, 742 (2008).

[158] A. E. T. Kuiper, M. F. Gillies, V. Kottler, G. W. âĂŹt Hooft, J. G. M. van Berkum, C. van der Marel, Y. Tamminga, and J. H. M. Snijders, Journal of Applied Physics **89**, 1965 (2001).

[159] R. T. Weitz, U. Zschieschang, F. Effenberger, H. Klauk, M. Burghard, and K. Kern, Nano letters **7**, 22 (2007).

[160] R. T. Weitz, U. Zschieschang, A. Forment-Aliaga, D. Kälblein, M. Burghard, K. Kern, and H. Klauk, Nano letters **9**, 1335 (2009).

[161] J.-F. Chang and H. Sirringhaus, Advanced Materials **21**, 2530 (2009).

[162] T. Bauer, T. Schmaltz, T. Lenz, M. Halik, B. Meyer, and T. Clark, ACS Applied Materials & Interfaces **5**, 6073 (2013).

[163] K. Kuribara, H. Wang, N. Uchiyama, K. Fukuda, T. Yokota, U. Zschieschang, C. Jaye, D. Fischer, H. Klauk, T. Yamamoto, K. Takimiya, M. Ikeda, H. Kuwabara, T. Sekitani, Y.-L. Loo, and T. Someya, Nature Communications **3**, 723 (2012).

[164] M. L. Chabinyc, R. Lujan, F. Endicott, M. F. Toney, I. McCulloch, and M. Heeney, Applied Physics Letters **90**, 233508 (2007).

[165] F. M. Li, P. Dhagat, H. M. Haverinen, I. McCulloch, M. Heeney, G. E. Jabbour, and A. Nathan, Applied Physics Letters **93**, 073305 (2008).

[166] S. Bain, *Kelvin Force Microscopy of Polymer and Small Molecule Thin-Film Transistors*, Phd thesis, University of Southampton (2011).

[167] D. H. Kim, Y. D. Park, Y. Jang, H. Yang, Y. H. Kim, J. I. Han, D. G. Moon, S. Park, T. Chang, C. Chang, M. Joo, C. Y. Ryu, and K. Cho, Advanced Functional Materials **15**, 77 (2005).

[168] M. Novak, T. Schmaltz, H. Faber, and M. Halik, Applied Physics Letters **98**, 093302 (2011).

[169] B. H. Hamadani, C. A. Richter, D. J. Gundlach, R. J. Kline, and I. Mcculloch, Journal of Applied Physics **102**, 044503 (2007).

[170] C. Wang, L. H. Jimison, L. Goris, I. McCulloch, M. Heeney, A. Ziegler, and A. Salleo, Advanced materials (Deerfield Beach, Fla.) **22**, 697 (2010).

[171] T. Hallam, M. Lee, N. Zhao, I. Nandhakumar, M. Kemerink, M. Heeney, I. McCulloch, and H. Sirringhaus, Physical Review Letters **103**, 256803 (2009).

[172] J. N. Haddock, X. Zhang, S. Zheng, Q. Zhang, S. R. Marder, and B. Kippelen, Organic Electronics **7**, 45 (2006).

[173] T. Hirose, T. Nagase, T. Kobayashi, R. Ueda, A. Otomo, and H. Naito, Applied Physics Letters **97**, 083301 (2010).

[174] F. Golmar, P. Stoliar, M. Gobbi, F. Casanova, and L. E. Hueso, Applied Physics Letters **102**, 103301 (2013).

[175] T. V. A. G. de Oliveira, A. E. Lopez, L. E. Hueso, and A. M. Bittner, (submitted) (2013).

[176] Y.-Y. Noh, X. Cheng, M. Tello, M.-J. Lee, and H. Sirringhaus, Semiconductor Science and Technology **26**, 034003 (2011).

[177] R. Noriega, J. Rivnay, K. Vandewal, F. P. V. Koch, N. Stingelin, P. Smith, M. F. Toney, and A. Salleo, Nature materials **12**, 1 (2013).

[178] D. Nečas and P. Klapetek, Central European Journal of Physics **10**, 181 (2011).

[179] A. Jedaa, M. Burkhardt, U. Zschieschang, H. Klauk, D. Habich, G. Schmid, and M. Halik, Organic Electronics **10**, 1442 (2009).

[180] F. Ante, D. Kälblein, U. Zschieschang, T. W. Canzler, A. Werner, K. Takimiya, M. Ikeda, T. Sekitani, T. Someya, and H. Klauk, Small (Weinheim an der Bergstrasse, Germany) **7**, 1186 (2011).

[181] F. Ante, *Contact Effects in Organic Transistors*, Phd thesis, École polytechnique fédérale de Lausanne (2011).

[182] K. Ando, S. Watanabe, S. Mooser, E. Saitoh, and H. Sirringhaus, Nature materials **12**, 1 (2013).

[183] L. Chen, P. Degenaar, and D. D. C. Bradley, Advanced Materials **20**, 1679 (2008).

[184] K. Lee, S. Cho, S. H. Park, a. J. Heeger, C.-w. Lee, and S.-h. Lee, Nature **441**, 65 (2006).

[185] O. Bubnova, Z. U. Khan, H. Wang, S. Braun, D. R. Evans, M. Fabretto, P. Hojati-Talemi, D. Dagnelund, J.-B. Arlin, Y. H. Geerts, S. Desbief, D. W. Breiby, J. W. Andreasen, R. Lazzaroni, W. M. Chen, I. Zozoulenko, M. Fahlman, P. J. Murphy, M. Berggren, and X. Crispin, Nature materials , 3 (2013).

[186] N. Huby, S. Ferrari, E. Guziewicz, M. Godlewski, and V. Osinniy, Applied Physics Letters **92**, 023502 (2008).

[187] S. Tatay, C. Barraud, M. Galbiati, P. Seneor, R. Mattana, K. Bouzehouane, C. Deranlot, E. Jacquet, A. Forment-Aliaga, P. Jegou, A. Fert, and F. Petroff, ACS nano **6**, 8753 (2012).

[188] S. Pramanik, C.-G. Stefanita, S. Patibandla, S. Bandyopadhyay, K. Garre, N. Harth, and M. Cahay, Nature nanotechnology **2**, 216 (2007).

[189] X. C. Wu, a. M. Bittner, and K. Kern, Langmuir **18**, 4984 (2002).

[190] M. Knez, A. M. Bittner, F. Boes, C. Wege, H. Jeske, E. Maiβ, and K. Kern, Nano Letters **3**, 1079 (2003).